_____

RAINCAST WP2000

WP2100 REPORT	Page 2
WP2200 REPORT	Page 42

RAINCAST

WP2100 REPORT

Review of the observation techniques

E. Cattani[1], V. Levizzani[1], G. Panegrossi[1], M. Montopoli[1], A. Battaglia[2]

1. CNR-ISAC, Italy
2. University of Leicester, Leicester UK

1 INTRODUCTION

Satellite sensors represent a unique source of observations essential for the global monitoring of precipitation, complementing the surface observations that are too sparse and primarily restricted to populated land regions (Kidd et al., 2017), and (in the case of weather radars) nearby coastal waters. At present about 40 years of satellite observations are available for the quantitative estimation of precipitation thanks to an increasing availability of precipitation-capable sensors based on different observation principles/techniques. The present scenario includes conical and cross-track scanning multichannel passive microwave (PMW) instruments on board low Earth orbiting (LEO) satellites, geostationary (GEO) visible/infrared (VIS/IR) imagers, and cloud and precipitation radars. The increasing number of precipitation-devoted satellite sensors and the improvement of the related technologies allowed for providing precipitation products at temporal and spatial scales close to diverse user requirements. Nevertheless, further improvements are expected in terms of precipitation estimate accuracy, spatial and temporal resolution, and spatial coverage of the observations, as expressed by the different user's communities [Report WP1000]. This means that besides the continuation of the operational missions to ensure the uninterrupted data flow necessary for hydro-meteorological applications and the exploitation of the long-term data sets for climate monitoring, new observation techniques need to be explored for their near future launch, including multi-frequency radars and constellations of small satellites. The innovation of the satellite observing systems is in fact strictly connected with the need to fill the existing gaps in precipitation remote sensing, chiefly the quantification of solid/liquid precipitation at high latitudes and of low-intensity rainfall. The last few decades of research on satellite precipitation have clearly identified solid and low-intensity precipitation as current gaps in existing global products. Even the advent of the Global Precipitation Measurement (GPM) mission has not completely filled these gaps due to several limitations in the radar observing capabilities. Note that improvements in solid precipitation retrievals from space could well contribute to a better quantification of the snowfall contribution to the water cycle by partially overcoming current limitations of ground-based measurement techniques (Rasmussen et al., 2012). The introduction of the orographic effects on precipitation formation (e.g., Shige et al., 2013; Yamamoto et al., 2017), the correct identification and weighing of warm rain (especially in the Tropics; e.g., Sohn et al., 2013; Song and Sohn, 2015) as well as an adequate sensing of the cloud horizontal and vertical structure appear necessary to ensure a successful precipitation retrieval both for cloud physics reasons (Stephens and Kummerow, 2007) and for mere geometric effects (e.g., Guilloteau et al. 2018). Finally, the new missions need necessarily to contribute shedding new light not only on the amount and intensity of precipitation, but also on its frequency and distribution, especially for managing weather-related risks (e.g., Marra et al. 2019; Mazzoglio et al., 2019), clearly spotting extremes out of ordinary events (e.g., Zorzetto et al., 2016) and identifying climate change effects on the water cycle (e.g., Trenberth et al., 2003; Trenberth and Zhang, 2018). For these reasons, the new precipitation-oriented missions should aim at a truly global coverage while at the same time fully exploiting the capabilities of PMW and multi-frequency radars.

In this context the aim of this report is to provide a review of the present observing system for satellite remote sensing of precipitation with a focus on the recent advances for the solid and light precipitation (Section 2). A survey of the new mission concepts based on constellation of small satellites and the new sensors planned for the near future are presented in Sections 3 and 4, respectively. Finally, Section 5 addresses critical gaps in the observational techniques with reference to the still open issues in precipitation remote sensing, and provides recommendations from the user community.

2 REVIEW OF THE STATE-OF-THE-ART OBSERVING SYSTEM FOR SATELLITE REMOTE SENSING OF PRECIPITATION

Several well documented review articles are available in the literature providing a complete description of algorithms, retrieval techniques and products. Note that, however, such reviews become rapidly outdated by rapidly evolving technology and science developments. Among such review articles, we will cite: Kidd et al. (2010), Kidd and Huffman (2011), Kidd and Levizzani (2011), Michaelides et al. (2009), Stephens and Kummerow (2007), Sun et al. (2018), Tapiador et al. (2012, 2017). The International Precipitation Working Group (IPWG, http://ipwg.isac.cnr.it) maintains a list of available satellite precipitation products and fosters collaboration on new development and dissemination of results to end-users (Levizzani et al., 2018). A most comprehensive book on satellite precipitation measurement including state-of-the-art techniques and science, validation and applications is currently in press (Levizzani et al., 2019).

2.1 VIS/IR sensors – GEO satellites

Thermal IR (TIR) observations from GEO sensors are widely exploited for the precipitation remote sensing because of their high time sampling and spatial resolution, which are consistent with precipitation temporal variability and suitable for daily precipitation accumulation. GEO sensors provide information on cloud top characteristics (temperature, optical thickness, thermodynamic phase, and effective radius), which are useful to identify precipitating clouds. The TIR-derived cloud top temperature in particular is used in the precipitation retrieval, considering colder cloud tops as indicators of precipitating clouds with a high vertical development. This is the idea at the base of the TIR precipitation estimate, a quite indirect retrieval methodology relying only on cloud top properties, which needs the support of precipitation estimates from MW or rain gauge networks to establish the connections between the TIR observation and precipitation intensity through statistical relationships or dynamical calibrations (Report WP1000). TIR-based retrievals are more oriented to convective precipitation estimate with clear difficulties in warm/orographic precipitation retrieval due to the cloud top temperature thresholds that are often too low for identifying orographic precipitation bearing clouds (e.g., Dinku et al., 2008). Other limitations are the degradation of the spatial resolution at high latitudes that makes GEO observations inapplicable for those areas and the complete inability to distinguish between liquid and solid precipitation. The history of the development of these techniques can be found for example in Kidd and Levizzani (2011). In recent times advances can be registered mainly concerning the introduction of cloud classification methods (e.g., Behrangi et al., 2010), the use of lightning data to improve heavy convective rainfall detection (e.g., Xu et al., 2014), the application of deep neural networks (Tao et al., 2018), and the improvement of the homogeneity of the products (e.g., Adler et al., 2018) and of the undercatch biases of the climatology (Funk et al., 2015).

2.1.1 Current status of GEO relevant instruments

Out of the 156 operational meteorological satellites presently in orbit, about 17 are operational from a geostationary orbit (World Meteorological Organization – Observing Systems Capability Analysis and Review Tool, WMO – OSCAR, https://www.wmo-sat.info/oscar/spacecapabilities). Each GEO

sensor monitors about one third of the Earth surface according to its own sub-satellite point (full disk). Nevertheless, due to the spatial resolution deterioration while approaching the border of the full disk with the consequent limited usability of the data in that area, five operational GEO satellites are required to ensure a complete West-East and North-South (~70°N – 70° S) coverage (Kidd and Huffman, 2011). Currently the primary platforms contributing to the GEO constellation are operated by the European Organization for the Exploitation of the Meteorological Satellites (EUMETSAT) with the Meteosat satellite series, the National Oceanic and Atmospheric Administration (NOAA) with the Geostationary Operational Environmental Satellite (GOES) satellites, the China Meteorological Administration (CMA) through the Feng-Yun-2 and 4A (FY-2, FY-4A) platform series, the Japan Meteorological Agency (JMA) with the Himawari-8 and 9 (in stand-by), and finally the Korea Meteorological Administration (KMA) with the Communication, Ocean, and Meteorological Satellite (COMS) and the GEO-KOMPSAT-2A (GK-2A, in commissioning phase) platforms. During the last decades these agencies promoted a continuous improvement of the VIS/IR sensors on board the GEO satellites, giving rise to a transition towards sensors equipped with a higher number of spectral channels, better spatial resolutions, and reduced acquisition time. Table 1 and 2 summarize the characteristics of the GEO sensors of the last generation.

Table 1: Summary of the presently operational geostationary sensors and their lifetime schedule (WMO-OSCAR, https://www.wmo-sat.info/oscar/gapanalyses). Information about the lifetime of the Meteosat satellite series come from the EUMETSAT's OSSI (https://www.eumetsat.int/ossi/webpages/about.html).

Sensor	Satellite	SSP	2019	2020	2021	2022	2023	2024	2025	2026	2027	2028	2029	2030	2031
ABI	GOES-16	75.2° W													
ABI	GOES-17	137.2° W													
AGRI	FY-4A	105° E													
AHI	Himawari-8	140.7° E													
AHI	Himawari-9	140.7° E													
AMI	GK-2A	128.2° E													
SEVIRI	Meteosat-11	0°						Availability lifetime until 2024 – from EUMETSAT							
SEVIRI	Meteosat-10 RSS	9.5°E						Availability lifetime until 2024 – from EUMETSAT							
SEVIRI	Meteosat-8 IODC	41.5°E			Fuel lifetime is until 2020 – from EUMETSAT										

The common characteristics are:
1. Spectral channel equipment: at least two channels in VIS and the TIR window at ~ 11 μm; one or more channel(s) in the NIR, the SWIR and the MWIR window at ~ 3.7 μm, and two or more channels in the TIR water vapor 6.3 μm band. This enables observing a wide range of geophysical variables, including cloud classification and properties (top temperature, optical thickness, thermodynamic phase and effective radius), atmospheric motion wind by cloud and water vapor tracking, and precipitation intensity.
2. Spatial resolution: ranging from 2(3) km at the sub-satellite point (SSP) for the NIR/SWIR/MWIR channels to 1 km or even better for the VIS channels.
3. Acquisition time: from 15-10 min for the full disk, up to 2.5 – 7.5 min or less for the acquisition of limited areas in the rapid scanning service (RSS) mode.

Table 2: GEO satellite sensor fact sheets.

Advanced Baseline Imager (ABI)

Platforms: NOAA - GOES 16 and 17, operational since Dec 2017 and Feb 2019 at 75.2° and 137.2° W, respectively.

Channels (resolution): 470 nm (1 km), 640 nm (0.5 km), 860 nm (1 km), 1380 nm (2 km), 1610 (1 km), 2260 nm (2 km), 3.90, 6.15, 7.00, 7.40, 8.50, 9.70, 10.3, 11.2, 12.3 13.3 μm (2 km).

Scanning technique: Mechanical, 3-axis stabilized satellite, E-W continuous, S-N stepping.

Coverage/cycle: Full disk every 15 min, CONUS in 5 min, 1000 x 1000 km2 in 30 s.

Advanced Geostationary Radiation Imager (AGRI)

Platforms: CMA - Feng-Yun-4A (105° E), Feng-Yun-4B planned in ≥ 2019.

Channels-resolution: 0.47 (1km), 0.65 (0.5-1 km), 0.825 (1 km), 1.375 (2 km), 1.61 (2 km), 2.25 (2-4 km), 3.75, 6.25, 7.1, 8.5, 10.7, 12.0, 13.5 μm (2 km).

Scanning technique: Mechanical, 3-axis stabilized satellite, E-W continuous, S-N stepping.

Coverage/cycle: Full disk acquisition in 15 min, RSS of the north disk in 2.5-5-7.5 min according to the observation mode.

Advanced Himawari Imager (AHI)

Platforms: JMA – Himawary-8 and 9 (140.7° E).

Channels-resolution: 0.455, 0.510 (1 km), 0.645 (0.5 km), 0.860 (1 km), 1.61, 2.26, 3.85, 6.25, 6.95, 7.35, 8.60, 9.63, 10.45, 11.20, 12.35, 13.30 μm (2 km).

Scanning technique: Mechanical, 3-axis stabilized satellite, E-W continuous, S-N stepping.

Coverage/cycle: Full disk acquisition in 10 min, RSS of the limited areas in shorter time intervals.

Advanced Meteorological Imager (AMI)

Platforms: KMA – GEO-KOMPOSAT-2A (128.2° E), the satellite is presently in the commissioning phase. The operational GEO service is carried out by the COMS satellite – MI sensor, a five VIS/MWIR/TIR channels sensor predecessor of the new AMI.

Channels-resolution: 0.470, 0.509 (1 km), 0.639 (0.5 km), 0.863 (1 km), 1.37, 1.61, 3.83, 6.21, 6.94, 7.33, 8.59, 9.62, 10.35, 11.23, 12.36, 13.29 μm (2 km).

Scanning technique: Mechanical, 3-axis stabilized satellite, E-W continuous, S-N stepping.

Coverage/cycle: Full disk acquisition in less than 10 min, RSS of limited areas in shorter time intervals.

Spinning Enhanced Visible and Infra-Red Imager (SEVIRI)

Platforms: EUMETSAT - Meteosat-11 (0° service), Meteosat-10 at 9.5°E (RSS), Meteosat-9 (standby), Meteosat-8 (operational at 41.5°E for IODC).

Channels-resolution: broad bandwidth VIS (0.6-0.9) μm - 1.6 km IFOV, 1 km sampling, 0.635, 0.81, 1.64, 3.92, 6.25, 7.35, 8.70, 9.66, 10.8, 12.0, 13.4 μm - 4.8 km IFOV, 3 km sampling.

Scanning technique: Mechanical, spinning satellite, E-W continuous, S-N stepping.

Coverage/cycle: Full disk every 15 min. RSS of limited areas in 5 min.

2.2   Passive and active MW sensors

Passive MW sensors, presently only on board of LEO satellites, provide a more direct mean to estimate precipitation than GEO VIS/IR sensors. The reason is that PMW frequencies are more directly responsive to the cloud internal processes and thus to precipitation formation mechanisms than the VIS/IR channels, because at these frequencies the precipitating hydrometeors are the main source of the attenuation (Michaelides et al., 2009). The emitted radiation from raindrops that makes

rain areas somewhat "warmer" that the surrounding "colder" ocean background and the reduction of the upwelling radiation due to scattering mainly related to ice particles are the two principal concepts at the base of the precipitation retrieval at these frequencies over ocean and land, respectively. The relatively low and the well predictable water surface emissivity makes the PMW retrieval methods more effective over ocean than over land. Surface emissivities are high and spatially quite variable so that the land surface contribution to the observable radiance is difficult to be separated from that of rain thus significantly affecting the rainfall retrieval accuracy. In recent years considerable research efforts were devoted to the creation of global surface emissivity maps in support of the PMW retrieval methods (e.g., Prigent et al., 2006), but the problem is still not completely solved. In this respect, higher frequency channels (> 89 GHz) can contribute to mitigate the effects of the poor knowledge of emissivity and scattering properties. Neural networks and large databases of surface types have been proposed for PMW retrieval algorithms such as for the Passive microwave Neural network Precipitation Retrieval (PNPR) both for cross-track (Sanò et al., 2016) and conical sensors (Sanò et al. 2018).

The more traditional Bayesian approaches have in turn been extended to more or less all the PMW radiometers on board the entire constellation of satellites that compose the GPM such as in the case of the Cloud Dynamics and Radiation Database (CDRD) algorithm (Casella et al., 2017). Kummerow et al. (2015) have also proposed a fully parametric approach to transform the Goddard Profiling algorithm (GPROF) for an operational use in the GPM era: the idea is to use a Bayesian inversion for all surface types using the full brightness temperature vector to obtain the most likely precipitation state.

High-frequency channels are instrumental also in solid precipitation retrieval, with the 150 GHz channel exhibiting the strongest scattering signature due to the precipitation sized ice particles only moderately affected by variations in surface emissivity (Levizzani et al., 2011; Laviola et al., 2015; Panegrossi et al., 2017). Recently, a few methods were proposed to estimate snowfall using diverse approaches such as training against CloudSat/CALIPSO observations and detecting supercooled water (Rysman et al. 2018), using a 1DVar method (Meng et al., 2017), and a hybrid PMW method dwelling on PMW measurements and global weather forecasts (Kongoli et al., 2018).

Recent studies demonstrate the potential of low frequency channels for the retrieval of precipitation over land trough the temporal variation of the brightness temperatures at 19 GHz due to the surface emissivity variation caused by the precipitation impact (You et al., 2018), and the benefits of using a combination of low (10-19 GHz) and high frequency (89-166 GHz) channels for snowfall detection (Ebtehaji and Kummerow, 2017). More details on the use of these channels in retrieval algorithms are provided in the WP2200 Report of this project.

2.2.1 Current status of PMW instruments

In the recent decades PMW sensors underwent a continuous evolution in terms of number of available platforms, acquisition modes (conical and cross-track scanning), spectral channels extended to high frequencies (sounders with channels in the water vapor absorption bands at 183 GHz), and spatial resolution. Moreover, the possibility to combine passive and active MW sensor observations provided a tool for a 3-D description of the precipitating systems. All these aspects contributed to reach the current configuration, where the LEO satellites with PMW sensors are able to obtain a near global coverage every 3h or less. The current constellation of PMW sensors is described in Table 3 (WMO-OSCAR Spaced-based Capability; see also Table 7 and 8 from Report WP1000 for complementary information):

Table 3: LEO PMW satellite sensor fact sheets.

Advanced Microwave Scanning Radiometer-2 (AMSR-2)

Platforms: JAXA GCOM-W1

Channels: 7 frequencies / 14 channels in the range 6.9 to 89 GHz, window channels only

Background: Follow-on of AMSR flown on ADEOS-2 and AMSR-E on EOS-Aqua

Scanning technique: conical scanning

Coverage/cycle: Global coverage once/day

Relevance: MW channels around 10, 19, 23, 37 and 90 GHz, to cover sea and land, heavy and light precipitation. High spatial resolution consistent with the scale of precipitation.

Advanced Microwave Sounding Unit – A (AMSU-A)

Platforms: NOAA-18, 19, EUMETSAT MetOp-A, B, C

Channels: 15 channels from 23.8 to 89.0 including the 54 GHz band

Background: Replacing MSU flown on TIROS-N and NOAA-9 to -14

Scanning technique: cross-track scanning

Coverage/cycle: near-global coverage twice/day

Relevance: MW channels in the 54 GHz band. Suitable for liquid precipitation over sea and land, Insensitive to surface emissivity

---

Advanced Technology Microwave Sounder (ATMS)

Platforms: SNPP, NOAA-20

Channels: 22 channels (23.8 – 183 GHz) including the 54 and 183 GHz bands

Background: development merging AMSU-A and AMSU-B flown on NOAA-15 to 17

Scanning technique: cross-track scanning

Coverage/cycle: near-global coverage twice/day

Relevance: MW channels in the 54 and 183 GHz bands. Suitable for solid and liquid precipitation over sea and land, Insensitive to surface emissivity

---

GPM Microwave Imager (GMI)

Platform: NASA GPM Core Observatory

Channels: 8 frequencies / 13 channels from 10.65 to 183.31 GHz;

Background: evolution of TMI on TRMM

Scanning technique: conical scanning

Coverage/cycle: Near-global coverage in 2 days; high latitudes (> 70°) not covered

Relevance: MW channels around 10, 19, 23, 37 and 90 GHz, to cover sea and land, heavy and light precipitation. High spatial resolution consistent with the scale of precipitation

---

Microwave Humidity Sounder (MHS)

Platforms: EUMETSAT MetOp-A (channel at 183.31 ± 10 GHz noisy since 2009), MetOp-B and C, NOAA-18, 19

Channels: 5 channels from 89 to 190 GHz

Background: Replacing AMSU-B on NOAA 15/16/17

Scanning technique: cross-track scanning

Coverage/cycle: Near-global coverage twice/day

Relevance: MW channels in the 183 GHz band. Suitable for solid precipitation over sea and land, Insensitive to surface emissivity

---

Micro-Wave Humidity Sounder -2 (MWHS-2)

Platforms: CMA FY- 3C, and 3D

Channels: 15 channels from 89 GHz, including band at 183 and 118 GHz

Background: Replacing the MWHS-1 of FY-3A and FY-3B

Scanning technique: cross-track scanning

Coverage/cycle: Global coverage twice/day

In response to ITT: AO/1-9324/18/NL/NA

Relevance: MW channels in the 118 and 183 GHz bands. Suitable for solid and, to a less extent, liquid precipitation over sea and land, Insensitive to surface emissivity

Micro-Wave Radiation Imager (MWRI)
Platforms: CMA FY -3B, 3C and 3D
Channels: 5 frequencies / 10 channels from 10.65 to 89 GHz
Background: New development
Scanning technique: conical scanning
Coverage/cycle: Global coverage once/day
Relevance: MW channels around 10, 19, 23, 37 and 90 GHz, to cover sea and land, heavy and light precipitation.

Sondeur Atmosphérique du Profil d'Humidité Intertropicale par Radiométrie (SAPHIR)
Platform: ISRO-CNES Megha-Tropiques
Channels: 6 channels in the 183 GHz band
Background: New development
Scanning technique: cross-track scanning
Coverage/cycle: Intertropical coverage 2 to 5 times/day depending on latitude (best coverage at 15°N and 15°S)
Relevance: MW channels in the 183 GHz band. Suitable for solid precipitation over sea and land, Insensitive to surface emissivity

Special Sensor Microwave - Imager/Sounder (SSMIS)
Platforms: DoD, NOAA DMSP-F16, 17, and 18
Channels: 21 frequencies / 24 channels from 19.35 to 183.31 GHz, including the 54 and 183 GHz bands
Background: Replacing and merging SSM/I, SSM/T and SSM/T-2 flown on DMSP up to F15
Scanning technique: conical scanning
Coverage/cycle: Global coverage once/day
Relevance: MW channels around 19, 23, 37 and 90 GHz; and in bands 54 and 183 GHz, insensitive to surface emissivity and providing information on atmospheric structure

2.2.2   *The Global Precipitation Measurement mission*

The combined use of passive and active MW instruments has represented a clear step forward in the precipitation retrieval from space since the launch of the Tropical Rainfall Measurement Mission (TRMM) in 1997. For the first time a Precipitation Radar (PR) at Ku-band (13.8 GHz), a PMW multi-frequency imager (TRMM Microwave Imager, TMI), and a Lightning Imaging Sensor (LIS) were hosted on the same platform in a non-Sun-synchronous orbit observing at different times of the day (Kummerow et al., 1998, 2000). TRMM allowed for looking through the precipitation column, providing new insights on the three-dimensional distributions of precipitation and latent heating in the Tropics. In 2014 the GPM mission collected the legacy from TRMM further expanding the rain-sensing capabilities. The key member of the mission is the GPM–Core Observatory (GPM–CO), carrying the most advanced precipitation sensors currently in space, i.e. the first Dual-frequency Precipitation Radar (DPR) provided by JAXA and the multi-frequency GPM Microwave Imager (GMI) from NASA (Skofronick-Jackson et al., 2017, 2018), from a non-Sun-synchronous orbit at 65°inclination. The GPM-CO observations are complemented by the acquisitions of a constellation of international satellite partners of opportunity, including the sensors SSMIS, AMSR-2, SAPHIR, MHS, and ATMS for a total of 11 satellites (Table 4).

Table 4: GPM constellation members (Skofronick-Jackson et al., 2018).

Satellite	Sensor	Launch	Until
TRMM	TMI	27 Nov 1997	8 Apr 2015
TRMM	PR		
DMSP F16	SSMIS	10 Oct 2003	
NOAA 18	MHS	5 May 2005	21 Oct 2018
MetOpA	MHS	19 Oct 2006	
DMSP F17	SSMIS	5 Nov 2006	
NOAA 19	MHS	6 Feb 2009	
DMSP F18	SSMIS	18 Oct 2009	
Megha-Tropiques	SAPHIR	12 Oct 2011	
SNPP	ATMS	28 Oct 2011	
GCOM-W1	AMSR-2	17 May 2012	
MetOpB	MHS	17 Sept 2012	
GPM-CO	GMI	27 Feb 2014	
GPM-CO	DPR		
DMSP F19	SSMIS	3 Apr 2014	11 Feb 2016

In this frame the GPM-CO has the role of calibrator to ensure unified and consistent precipitation estimates from all satellite partners at high temporal (0.5-3.0 h) and spatial (5-15 km) scales, allowing for detailed investigations of the precipitation distribution and variability.

The DPR instrument consists of a Ka-band precipitation Radar (KaPR) operating at 35.5 GHz and a Ku-band Precipitation Radar (Ku-PR) at 13.6 GHz (Hou et al., 2014). The KuPR and KaPR have coaligned 5 km resolution footprints over the cross-track swath widths of 245 and 125 km, respectively (Figure 1), with a nearly simultaneous data acquisition in the inner swath of 120 km.
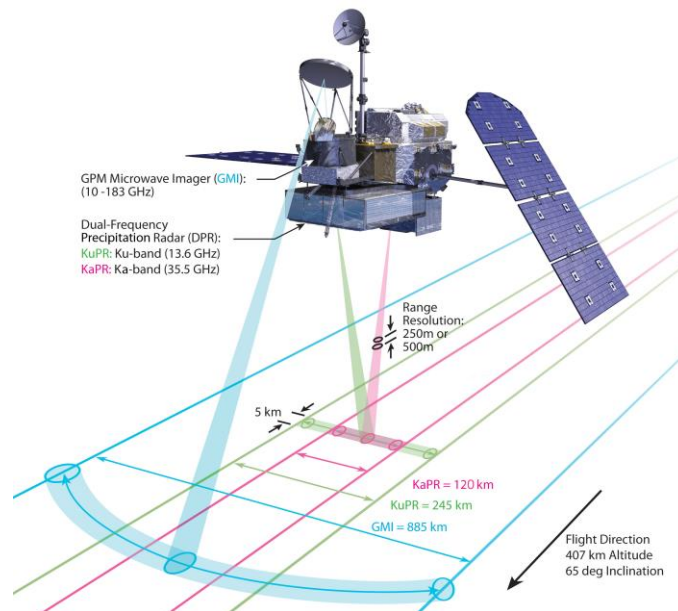
Figure 1: Swath coverage of the GPM–Co sensors. [available at https://pmm.nasa.gov/GPM]

Both radars have a nominal vertical range resolution of 250 m, sampled every 125 m, with a minimum detectable signal of better than 18 dBZ. During the KuPR acquisition of the outer portion of the 245 km swath, the KaPR enters the high-sensitivity acquisition mode, by acquiring data from

the interlaced fields as shown in Figure 2. The KaPR high-sensitivity mode has a minimum detectable signal of approximately 12 dBZ with a vertical resolution of 500 m. Since 21 May 2018 the Ka radar scans like the Ku (see Figure 2b).
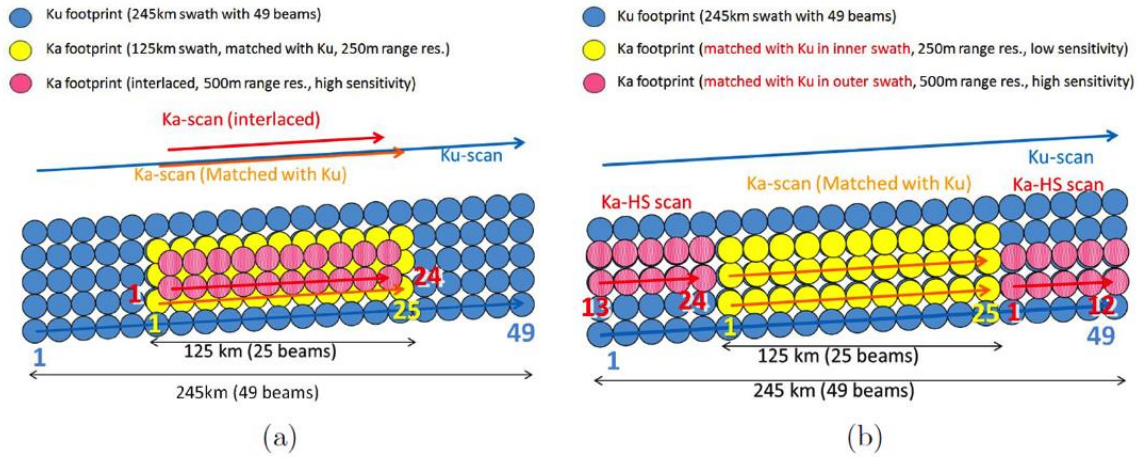
Figure 2: DPR's scan patterns before 21 May 2018 (a) and after 21 May 2018 (b). KaHS beams scan in the inner swath before 21 May 2018, but now they scan in the outer swath and match with KuPR's beams. Numbers in color indicate angle bin numbers for KuPR (blue), KaMS (yellow), and KaHS (red). HS stands for High Sensitivity and MS for Matched Scan

Table 5: Comparison between the GPM DPR and TRMM PR instrument characteristics (Hou et al., 2014).

Instrument	GPM KaPR at 407 km	GPM KuPR at 407 km	TRMM KuPR at 350 km
Antenna type	Active phased array (128)	Active phased array (128)	Active phased array (128)
Frequency (GHz)	35.547 and 35.553	13.597 and 13.603	13.796 and 13.802
Swath width (km)	120	245	215
Horizontal resolution at nadir (km)	5	5	4.3
Transmitter pulse width (μs)	1.6/3.2 (×2)	1.6 (×2)	1.6 (×2)
Range resolution (m)	250/500	250	250
Observation range (km) (mirror image at nadir)	18 to −3	18 to −5	15 to −5
Pulse repetition frequency (Hz)	Variable (4275 ± 100)	Variable (4206 ± 170)	Fixed (2776)
Sampling number	108 ~ 112	104 ~ 112	64
Transmitter peak power (W)	>146	>1013	>500
Minimum detectable Z_e and rain rate*	12 dBZ (500 m res.) (0.2 mm h^{-1})	18 dBZ (0.5 mm h^{-1})	18 dBZ (0.7 mm h^{-1})
Measurement accuracy (dBZ)	<±1	<±1	<±1
Data rate (Kbps)	<78	<112	<93.5
Mass (kg)	<300	<365	<465
Power consumption (W)	<297	<383	<250
Physical dimensions (m)	1.44 × 1.07 × 0.7	2.4 × 2.4 × 0.6	2.2 × 2.2 × 0.6

* Minimum detectable rain rate defined as $Z_e = 200\, R^{1.6}$ for DPR and $Z_e = 372.4\, R^{1.54}$ for TRMM PR.

Thus, although similar to the TRMM PR, the Ku-band channel of the DPR is designed to have higher precision resulting from a greater number of independent samples (used to form the average return power) and greater sensitivity owing to the higher transmitted peak power to achieve a minimum detection threshold of 0.5 mm h^{-1} (or 18 dBZ). The Ka band, when operated in the high sensitivity mode, further extends the DPR sensitivity range to detect precipitation rates down to

about 0.2 mm h^{-1} (12 dBZ). These figures were the ones foreseen for the mission before launch. In reality, the Ku band threshold is ~12 dBZ while the one for the Ka band is ~16dBz. In Table 5 a detailed comparison of the GPM DPR and the TRMM PR is reported.

Besides the higher sensitivity at light rain rates, a key advance of the DPR over the TRMM PR is its ability to provide quantitative estimates of the precipitation particle size distribution from the overlapping portion of the Ku and Ka swaths over a nominal range of precipitation intensities from a few to ~15 mm h^{-1}. DPR measurements provide physical insights into microphysical processes (evaporation, collision/coalescence, and aggregation) and improved capabilities in distinguishing regions of liquid, frozen, and mixed-phase precipitation (Hou et al., 2014).

The GMI is a conical scanning radiometer with a spectral channel equipment ranging from 10 to 183 GHz, thus combining the channels normally hosted on the imagers (TMI included) with high-frequency channels and the water vapor absorption band typical of the sounders. This channel selection was carried out with the intent to optimize the detection of heavy, moderate and light precipitation as detailed in Table 6 (Hou et al., 2014).

Table 6: Key application of the GMI channels.

Frequency (GHz)	Use
10	liquid precipitation
19 & 37	moderate to light precipitation over ocean
21	correction of the emission by water vapor
89	detection of ice particles for precipitation over ocean and land
166	light precipitation, typical outside the tropics
183	scattering signals due to small ice particles and estimating light rainfall and snowfall over snow-covered land

The GMI swath width is 885 km (Figure 1), whose central portion is overlapping the DPR Ku-Ka swaths with an approximately 67 s lag with respect to DPR observations due to geometry and spacecraft motion. The GMI antenna diameter together with the spacecraft altitude (407 km) ensure a higher spatial resolution than the TMI and all other radiometers in the GPM constellation.

New capabilities made possible by the GPM sensor suite concern the detection of snowfall (e.g., Panegrossi et al., 2017; You et al., 2017).

2.2.3   CloudSat and CALIPSO within the A-Train constellation

The synergistic use of satellite sensors is recently the more exploited concept and paves the way to high-level scientific results in the field of cloud and precipitation remote sensing. This concept experienced an evolution since 1997, when the TRMM mission deployed passive and active MW instruments (TMI and PR) on the same platform for the three-dimensional characterization of tropical precipitation. Now the satellite constellations represent the present and the near future for "distributed observing systems" (Stephens et al., 2018), as the previously described GPM or the recent small satellite constellations (see next section). The A-Train constellation belongs to this scenario in its own right and represents one of the most successful demonstrations of the effectiveness of an integrated approach for cloud and precipitation characterization. New insights into cloud and precipitation formation processes came from the observations jointly collected by CloudSat (Stephens et al., 2002, 2008) and the Cloud-Aerosol Lidar and Infrared Pathfinder Satellite Observations (CALIPSO; Winker et al., 2010) satellites since their launch on 28 April 2006, proving

together with TRMM mission and now GPM the importance of vertical profile information for understanding processes of the atmosphere. Table 7 summarizes the characteristics of the main instruments hosted by the two platforms, i.e. the Cloud Profiling Radar (CPR) and the Cloud-Aerosol Lidar with Orthogonal Polarization (CALIOP).

Table 7: Characteristics of CPR and CALIOP instruments.

Cloud Profiling Radar (CPR)
Platforms: *CloudSat*
Channels: 94.05 GHz
Resolution: horizontal - 1.4 km (cross-track) x 3.5 km (along-track); vertical - 500 m
Background: New development. Cooperation with Canadian Space Agency (CSA)
Scanning technique: None. Along-track sampling at 2 km intervals
Coverage/cycle: Global coverage in 16 days
Relevance: W-band sensitive to light precipitation, small drops and ice particles; boundary between precipitating and non-precipitating convective clouds.
Cloud-Aerosol Lidar with Orthogonal Polarisation (CALIOP)
Platforms: CALIPSO
Channels: two wavelengths (532 and 1064 nm), measurements at two orthogonal polarizations
Resolution: horizontal - 70 m IFOV sampled at 333 m intervals along track; vertical - 30 m
Background: New development
Scanning technique: Nadir-only viewing, sampling at 330 m intervals along track, near continuous profiling
Coverage/cycle: Global coverage in 16 days
Relevance: vertical distribution of clouds: cloud optical depth, top height, cloud drop and ice particle effective radius, cloud liquid and ice total column, freezing level height in clouds, melting layer depth in clouds

The combined use of CPR and CALIOP enabled new capabilities in observing clouds and precipitation. Figure 3 shows the multiyear zonally averaged frequency of occurrence of precipitation by type (Figure 3a), and the vertical profile of occurrence of precipitation (Figure 3b). Precipitation systems are much deeper on average in the tropics (Figure 3b), and the frequency of precipitation is strongly enhanced in middle and higher latitudes, where snowfall becomes the more prevalent mode of precipitation poleward of about 60°N and 60°S (Figure 3a) (Stephens et al., 2018).
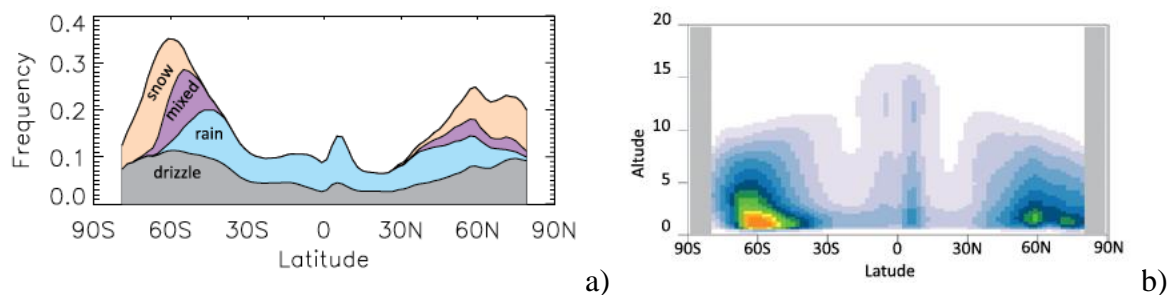
Figure 3: a) multiyear annual-mean precipitation fractional occurrence from CloudSat 2C-COLUMNPRECIP product; b) multiyear latitude–height sections of annual zonal-mean precipitation (attenuation-corrected radar reflectivity >0 dBZ) occurrence (Stephens et al., 2018).

In the CloudSat precipitation product exploited in Figure 3 (2C-COLUMNPRECIP; Haynes et al., 2009) the detection of precipitation is performed over land and ocean (Smalley et al., 2014), including a phase determination (rain, mixed, and snow) based on the maximum tropospheric temperature in the CloudSat observation profile. The precipitation occurrence is determined using the reflectivity profile of the lowest discernible cloud layer, after correction for attenuation.
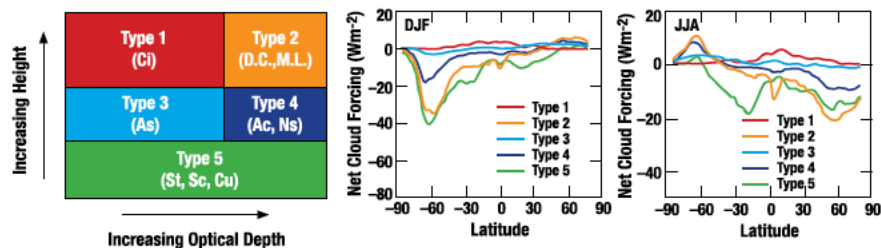
Figure 4: Contributions to the cloud radiation effects. The cloud classification is determined by the radar–lidar data of CloudSat and CALIPSO, where true cloud heights establishing the types and cloud thicknesses (x axis) are from water and ice path information, which is proportional to cloud optical depth.
Ci = cirrus, D.C. = deep convection, M.L. = multilayer, AS = altostratus, AC = altocumulus, NS = nimbostratus, St = stratus, SC = stratocumulus, and Cu = cumulus. (Stephens et al., 2018)

The joint observations of CloudSat and CALIPSO contributed to an updated interpretation of the contribution to the net cloud radiative effect from different cloud types, as shown in Figure 4. The cloud-top height is unambiguously determined using CloudSat-CALIPSO data. The profile information from the radar–lidar instrument pair allow for the identification of multilayered cloud systems, which occur about 60% of the time clouds are observed (Stephens et al., 2008). These multilayered categories, consisting mostly of high clouds over low clouds, are mostly missing in the radiance-based classifications.

CPR data have shown a great potential also for precipitation estimation and snowfall in particular, providing vertical profiles of snowfall rate along with snow size distribution parameters and snow water content (2C-SNOW-PROFILE; Wood and L'Ecuyer, 2018). The assessment of the surface precipitation type as dry snow or snow with a small melted fraction is conducted through the 2C-PRECIP-COLUMN product that provides vertically-resolved information on snowfall and snow properties between 82°N and 82°S together with uncertainty estimates, and treats complications due to radar attenuation and multiple scattering especially relevant for heavier snowfalls. Mind that a priori information is necessary on particle size distributions (PSD), mass, shape and scattering properties since the radar backscattering at the 94 GHz of the CPR is sensitive to all these quantities (e.g., Liu, 2008a; Wood et al., 2015). The phase of precipitation both aloft and at the surface is determined using coincident information on atmospheric temperature from the profiles of the European Centre for Medium-range Weather Forecasts (ECMWF); mind that, given the narrow temperature range 0-4°C where the transition from solid to liquid hydrometeors occurs, small variations in temperature can induce substantial changes in precipitation phase and the associated precipitation (e.g., Liu, 2008b). Issues with the CloudSat products are also linked to both ground clutter and the estimated fall speeds of the hydrometeors. Thus, significant improvements could potentially come from Doppler measurements (e.g., Illingworth et al., 2015) and enhanced resolution to reduce clutter.

The CPR has indeed contributed to advance our knowledge of snowfall distribution and characteristics around the globe. Several studies were made possible addressing science questions, for example, on: snowfall from shallow cumuliform clouds (Kulie et al., 2016; Kulie and Milani, 2018), snowfall over the Poles with first-hand investigations on snowfall over iced background (e.g., Milani et al., 2018;

Palerme et al., 2019), global distribution of solid precipitation and its characteristics (e.g., Adhikari et al., 2018). Figure 5 shows the first global census of snowfall events obtained from CloudSat.
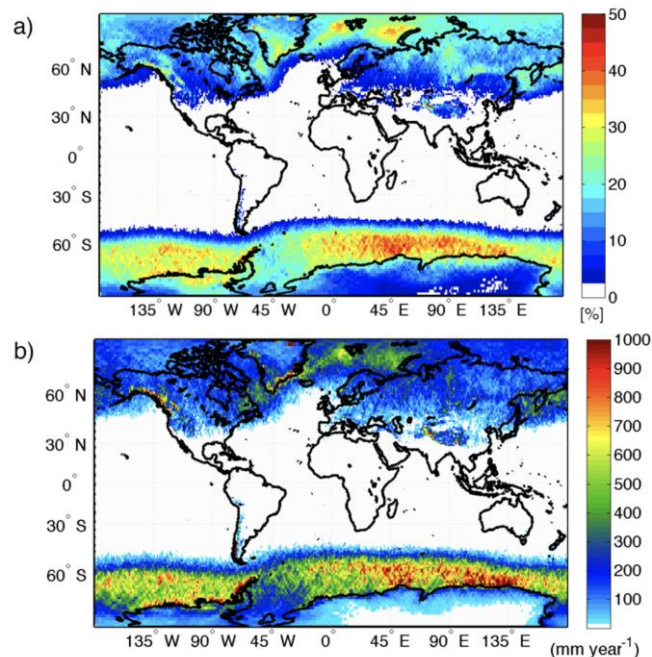
Figure 5: CloudSat-derived (a) snowfall fraction (%) and (b) mean annual liquid equivalent snowfall (mm yr^{-1}) in 1°×1° bins for a 2006–10 dataset. Snowfall fraction is defined as the number of snowfall events divided by the total number of observations in each grid box (Kulie et al., 2016).

2.2.4   Recent studies on spaceborne radars

Currently available technology has enabled the development of spaceborne radar concepts with Ka-band channels capable of achieving sensitivities around -10 dBZ, and electronic scanning radars operating at Ku-, Ka- and W-band (e.g., ACE 2016; Tanelli et al., 2018). This will allow multiple frequency radars such as the airborne Airborne Third Generation Precipitation Radar (APR-3; Ku-, Ka- and W-band) flown in the Olympic Mountain Experiment (OLYMPEX) Campaign (Chase et al., 2018), to be available on space platforms. Other developments include the increase of the spatial resolution and the design of Doppler capabilities. Finally, mm-wave technology advances have enabled the development and demonstration of instruments in the G-band (Battaglia et al., 2014). Inclusion of such capabilities in future radar systems that also operate at W-band (or lower) would allow measurement relative humidity and particle size in ice clouds and thus provide essential information for determining ice crystal growth processes and rates.

3   SMALL SATELLITE CONSTELLATIONS

Recent scientific and operational applications in several different fields, such as climate, meteorology, hydrology, agriculture, have introduced the need for higher space-time monitoring of the Earth's atmosphere and surface. In particular, clouds and precipitation observations for meteorology and climate are natural targets of high space-time resolution Earth-observation

missions, due to their diverse space-time evolving structure and to the high number of unsolved scientific questions on precipitation systems. Such needs cannot be anymore met by the current constellation of environmental and meteorological satellites because of the low revisit time resulting in inadequate coverage and of the costs of large platforms hosting several sensors. Moreover, it is crucial to ensure uninterrupted "heritage" measurements for climate applications, especially in the MW spectral range. New strategies thus become necessary to ensure cost effective and higher space-time resolution Earth-observation (EO) initiatives trying to break the traditional trade-off in EO mission design between GEO and LEO missions.

Small satellites appear to be the clear development avenue both in terms of new observation technologies and replicability of the single sensor translated into constellations that are relatively easy to launch and maintain. In particular, the recent development of High Electron Mobility Transistors (HEMT) or Metamorphic HEMT (MHEMT) promise an economical hardware solution for radiometers operating within the MW and millimeter wave spectrum. Microwave sensors spatial resolution is a function of frequency of operation, orbit altitude, and antenna aperture size. The largest antenna currently deployed is used by AMSR-2 with 2 m diameter. The solid parabolic reflector antennas are very large, heavy, and very expensive to launch to orbit. Deployable antennas for small satellites, e.g. CubeSats, are under development. Using these new technologies, a reflector with 2 m aperture and ~500 grams mass could be stowed into a 102 mm diameter cylinder 323 mm long, thus fitting into a 3U volume of a CubeSat.

As to the radar sensors, combinations of the two approaches that foresee one or few very capable radars vs. many simple radars on small satellites are currently being considered not only to increase global sampling and mapping, but also to provide three dimensional datasets at the meso-gamma scale, necessary to properly interpret the observed vertical profiles.

The Time-Resolved Observations of Precipitation structure and storm Intensity with a Constellation of Smallsats (TROPICS), the Temporal Experiment for Storms and Tropical Systems–Demonstrator (TEMPEST-D), the Radar in a CubeSat (RainCube), the Tropospheric Water and cloud ICE (TWICE), and the IceCube are the most promising small satellite missions focused on cloud and precipitation observations.

3.1 Time-Resolved Observations of Precipitation structure and storm Intensity with a Constellation of Smallsats (TROPICS)

The mission is based on the MicroMAS-2 CubeSats, which are dual-spinning 3U CubeSats (Figure 6) equipped with a 12-channel PMW high-performance radiometer scanning across the satellite track at 30 revolutions per minute (RPM) to provide both sounding (temperature and humidity, 2–3 km vertical resolution) and imaging capabilities. Each radiometer includes seven channels near the 118.75 GHz oxygen absorption line for temperature, 3 channels near the 183 GHz water vapor absorption line for water vapor profiles, a single channel near 90 GHz for precipitation measurements in combination with the previous channels, and a single channel at 206 GHz for cloud ice measurements. The TROPICS baseline configuration envisages a constellation of 6 CubeSats with two satellites in each of three equally spaced orbital planes with 30° inclination and 550 km altitude, which will allow for the mission requirement of 1 hr median revisit time to be achieved even with the failure of up to two satellites. The full swath of the radiometer observations will be fully programmable and extendable to ±60° from nadir, with a 1.5° cross-track sampling interval (81 spots/swath). The spatial resolution (averaged over the swath) is approximately 25 km for the

moisture channels (183–206 GHz) and approximately 40 km for the temperature channels (90–118 GHz).

Figure 6: The TROPICS space vehicle showing CubeSat bus, radiometer payload, and deployed articulated solar array (Blackwell et al., 2018).

TROPICS will provide rapid-refresh MW measurements over the tropics to observe the thermodynamics of the troposphere and precipitation structure for storm systems at the mesoscale and synoptic scale over the entire storm lifecycle. The main science objectives are: relate precipitation structure evolution, including diurnal cycle, to the evolution of the upper-level warm core and associated intensity changes of hurricanes and tropical storms; relate the occurrence of intense precipitation cores to storm intensity evolution; relate retrieved environmental moisture measurements to coincident measures of storm structure (including size) and intensity; and assimilate microwave radiances and/or retrievals in mesoscale and global numerical weather prediction (NWP) models to assess impacts on storm track and intensity. In this respect thanks to its high-resolution and rapid-updated PMW measurements, TROPICS will bridge the gaps between the GEO VIS-IR nearly continuous observations, with storm structure information primarily limited to the evolution of cloud tops, and PMW observations from LEOs, which are able to reveal the tropical cyclone structure beneath the cloud tops, but are relatively infrequent with gaps in time of several hours.

The mission has been selected by NASA as part of the Earth Venture-Instrument-3 (EVI-3) program currently scheduled for launch in late 2019 (Blackwell et al., 2018).

3.2 Temporal Experiment for Storms and Tropical Systems – Demonstrator (TEMPEST-D)

The TEMPEST-D mission (Reising et al., 2017, 2018) is a project of Colorado State University in partnership with NASA/Caltech Jet Propulsion Laboratory (JPL) and Blue Canyon Technologies. It is conceived to demonstrate the feasibility and capability of the TEMPEST Train mission based on a constellation of eight 6U CubeSats and focused on the study of rapidly evolving convective processes on a global scale. The TEMPEST Train mission will make measurements in quick succession using 8 PMW sensors in a single orbital plane (orbit altitude 425-450 km; inclination 50°-60°) with a constellation swath overlap of at least 320 km (Figure 7).
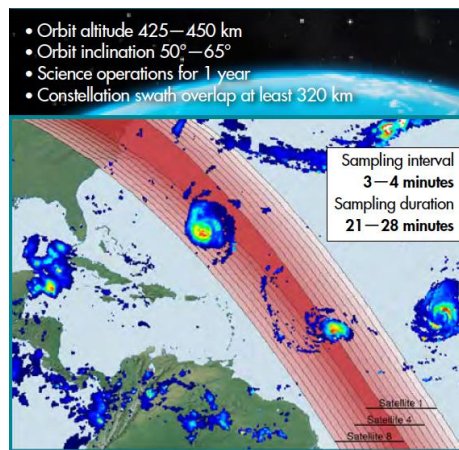
Figure 7: TEMPEST Train mission design. [https://tempest.colostate.edu/TEMPEST-Fact-Sheet.pdf]

The TEMPEST-D satellite was successfully launched on 21 May 2018 in a near circular orbit at an altitude of ~400 km and inclination of 51.6°. It acquired its first full-swath orbital observations capturing Hurricane Florence over the Atlantic Ocean on 11 September 2018, revealing the eye of the storm surrounded by towering, intense rain bands using the millimeter-wave radiometer on a CubeSat (Figure 8).

The Millimeter-wave Radiometer (MM) on board TEMPEST-D performs continuous measurements at five frequencies: 89, 165, 176, 180 and 182 GHz. It is a cross-track scanning instrument, measuring the Earth scene between ±45° nadir angles, and providing an 825-km wide swath from a 400-km nominal orbit altitude.
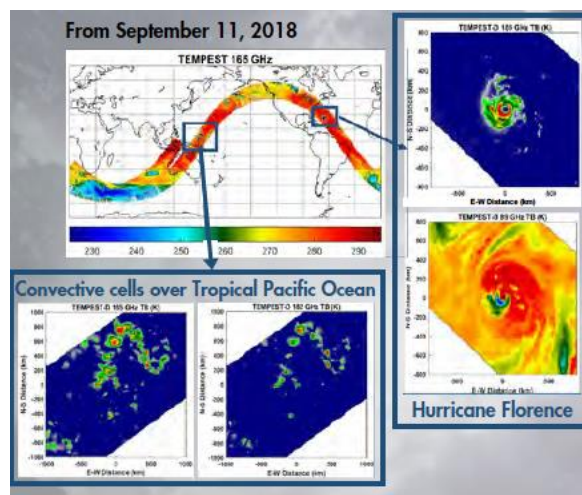
Figure 8: TEMPEST-D data capturing the features of hurricane Florence on 11 September 2018. [https://tempest.colostate.edu/TEMPEST-Fact-Sheet.pdf]

The mission is intended to measure the temporal evolution of clouds from the moment of the onset of precipitation in order to help improving our current understanding of cloud processes at the global scale and constraining one of the largest sources of uncertainty in climate models. Uncertainties in the representation/parameterization of key processes that govern the formation and dissipation of

clouds and control the global water and energy budgets lead to substantially different predictions of future climate in current models.
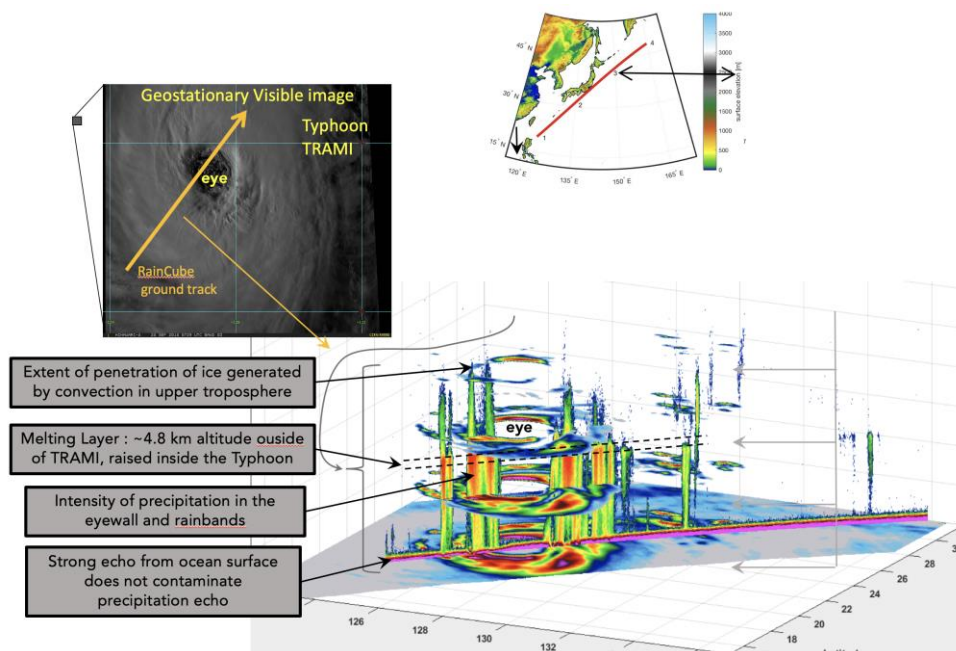
Figure 9: RainCube radar and TEMPEST-D PMW radiometer observe Typhoon Trami south of the Japan archipelago on 28 Sept. 2018. Note that the two satellites observed the typhoon 5 min apart. The radar-radiometer observation of the axi-symmetric structure of Typhoon Trami is particularly effective as its intensity changed rapidly.
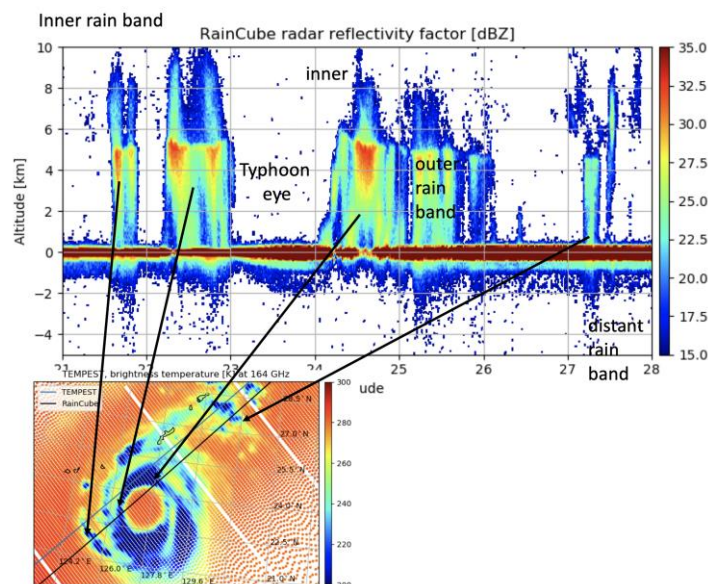
Figure 10: Same overpasses as in Figure 9 but referring to vertical cross section of the RainCube scan (top) and 164 GHz map of the TEMPEST-D radiometer (bottom). The radiometer provides the wider context: the typhoon has an axi-symmetric structure around a well-defined eye, an eyewall, and the outer spiral-like rainbands elongated from the center in the region of the outflow.
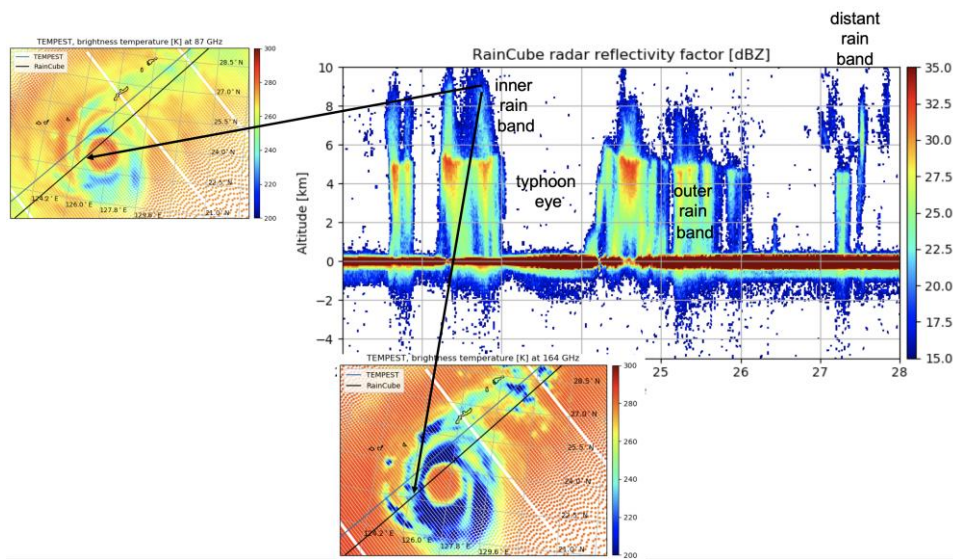
Figure 11: Same as Figure 10 with the addition of the 87 GHz map (top left). As frequency increases, the brightness temperatures are affected by the scattering of the frozen hydrometeors (snowflakes/aggregates): lower brightness temperature areas corresponding to the outflow spiral-like clouds become larger, because of the increasing optical thickness of the ice found in the upper cloud layers even for stratiform precipitation.

The observational capabilities of TEMPEST-D in synergy with the RainCube radar (see next Section) are shown in Figure 9, 10 and 11. The combination of Z and (high frequency) brightness temperatures can improve interpretation of ice microphysics (see Figure 11). The radiometer provides the necessary coverage via a large swath.

TEMPEST-D is supported by NASA's Science Mission Directorate, Earth Science Division and is managed by NASA's Earth Science Technology Office (ESTO). NASA JPL will provide the five-channel millimeter-wave radiometer instrument.

3.3 Radar in a CubeSat (RainCube)

RainCube (Peral et al., 2017) is a technology demonstration mission to enable Ka-band precipitation radar technologies on a low-cost, quick-turnaround platform. It is sponsored by NASA ESTO through the InVEST-15 program and has already led to the development of a 35.75 GHz radar payload to operate within 6U CubeSats. The payload is a Ka-band radar of new architecture equipped with an ultra-compact lightweight deployable antenna (Figure 12). The project completed integration and testing in February 2018 and was delivered in March 2018. RainCube was launched from NASA's Wallops Flight Facility on 21 May 2018 as part of the deployment of CubeSats from the International Space Station (ISS). RainCube has three main objectives: develop, launch, and operate the first radar instrument on a CubeSat (6U); demonstrate new technologies and provide space validation for a Ka-band (35.75 GHz) precipitation profiling radar at platform altitude of 400 km or less (requirements against real figures in flight are shown in Table 8); enable future precipitation profiling Earth science missions on a low-cost, quick-turnaround platform. RainCube wants to fill the current gap in precipitation profiling capabilities, which are limited to a few instruments deployed in Low Earth Orbit (LEO). Such satellites cannot provide the temporal

resolution necessary to observe the evolution of weather phenomena down to the minute time scale. The cost of deploying a LEO constellation of such radar sensors would be prohibitive and thus the CubeSats are a feasible alternative (Peral et al., 2018), which should revolutionize our current capabilities of observing the internal structure of clouds at unprecedented space-time resolution.
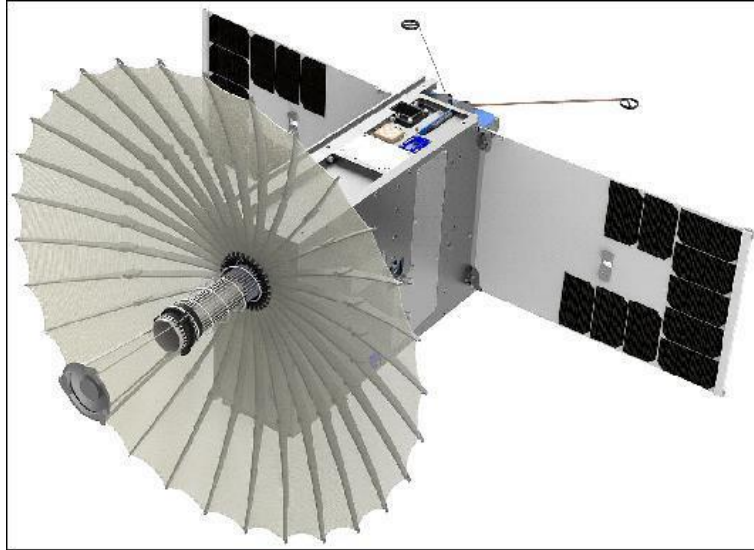
Figure 12: RainCube with its umbrella-like parabolic mesh 0.5 m antenna, which deploys out of its 1.5U canister.

Table 8: Radar electronics and antenna requirements for RainCube.

Requirement Name	Requirement	Measured
Sensitivity @400km	20 dBZ	11.0 dBZ
Horizontal resolution @400km	10 km	**7.9 km**
Nadir Data Window	0-18 km	-3 to 20 km
Vertical resolution	250 m	**250 m**
Downlink data rate (in transmit)	50 kbps	49.57 kbps
Payload power consumption (AntDeployment/STDBY/RXOnly/TXScience)	10 / 8 / 15 / 35 W	5 / 3 / 10 / **22** W
Mass	6 kg	**5.5 kg**
Range sidelobe suppression	>60 dB @ 5 km	>65 dB @ 1 km
Transmit power & Transmit loss	10 W / 1.1 dB	>39 dBm
Antenna gain	42 dB	42.6 dB
Antenna beam width	1.2 deg	1.13 deg

A first cut to RainCube observational capabilities is provided in Figure 13 where observations of different storms are collected and in Figure 14 where the comparison with GPM DPR is summarized.
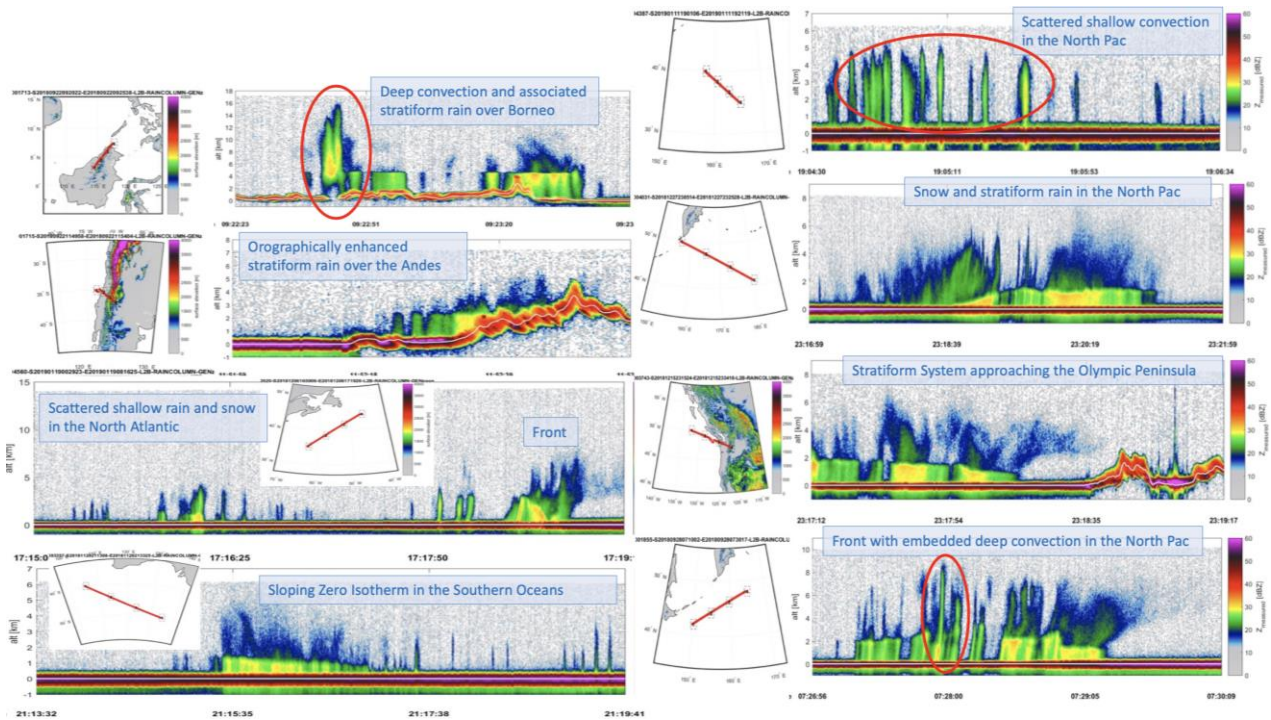
Figure 13: Collection of storms observed by RainCube.
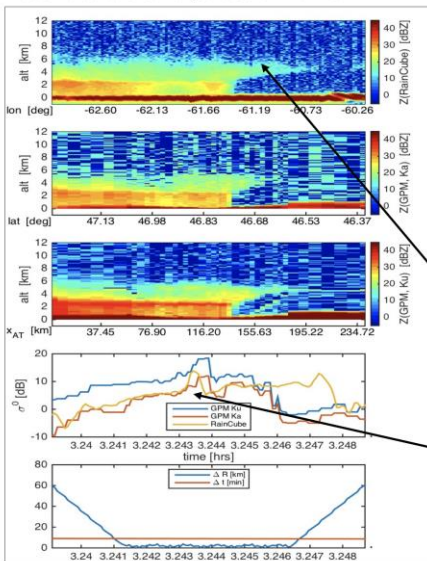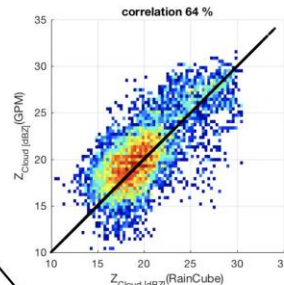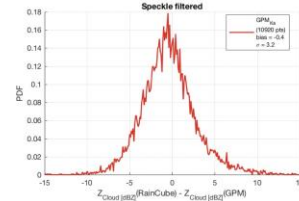
Figure 14: Comparison of the RainCube radar capabilities with GPM DPR's on co-located overpasses.

3.4 Tropospheric Water and cloud ICE (TWICE)

TWICE is led by Colorado State University (Reising et al., 2016) and is based on a PMW radiometer with 4 channels at 118 GHz, 4 channels at 183 GHz, 2 channels at 240 GHz, 4 channels at 310 GHz,

and 2 channels at 670 GHz (V and H polarization). The radiometer aims at providing ice particle size information in both polluted and clean environments, and determining the influence of aerosol pollution on cloud particle size spectrum. The constellation wants to meet the scientific need for a better measurement of water vapor and ice clouds in the upper troposphere at a variety of local times covering the full diurnal cycle to address current limitations of PMW sensors in sun-synchronous orbits. This in order to improve the current limited understanding of upper tropospheric/lower-stratospheric (UTLS) processes in general circulation models (GCMs) for climate modelling. The TWICE instrument will meet the size, weight and power requirements for deployment in a 6U-Class satellite (see Figure 15 for some details on the satellite).
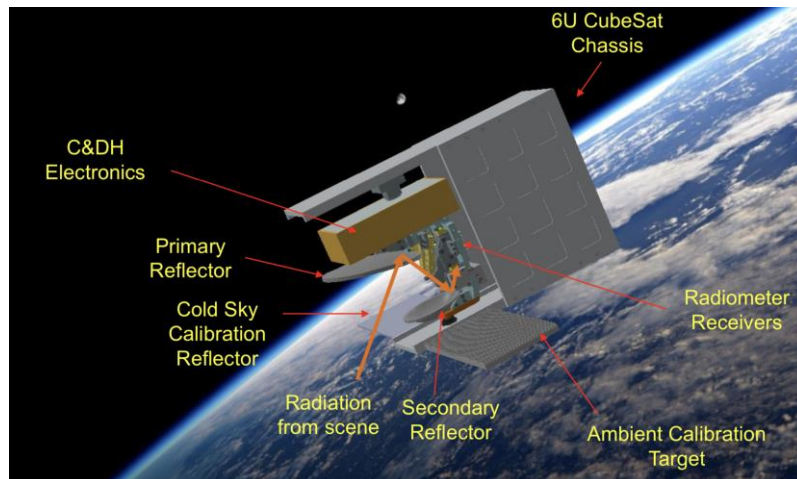
Figure 15: Artist vision in space of the TWICE mission (courtesy S. C. Reising).
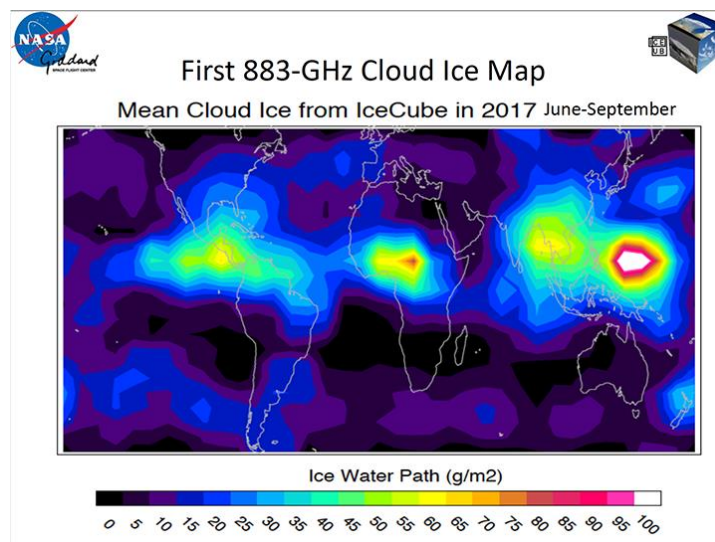
Figure 16: The first ever 883 GHz cloud ice map. [https://atmospheres.gsfc.nasa.gov/climate/index.php?section=259]

_____

3.5   IceCube

IceCube (Esper et al., 2018), deployed from the ISS in May 2017, has demonstrated-in-space a commercial 883 GHz radiometer developed by Virginia Diodes Inc., Charlottesville, VA, under a NASA Small Business Innovative Research contract. The main goal of the mission is the observation of the cloud ice and its role in the Earth's climate system regulating atmospheric radiation and interacting with dynamic, energetic and precipitation processes. Sensing atmospheric cloud ice requires instruments tuned to a broad range of frequency bands. However, it's particularly important to fly submillimeter sensors to fill a significant data gap in the middle and upper troposphere, where ice clouds are often too opaque for IR and VIS sensors to penetrate, and also provide data about the tiniest ice particles that can't be detected clearly in other MW bands.

At this submillimeter wavelength the cloud ice scattering produces a larger brightness temperature depression than at lower frequencies, which can be used to retrieve vertically-integrated cloud Ice Water Path (IWP) and ice particle size (Figure 16).

The next step is to infuse this experience into an ice-cloud imaging radiometer for NASA's next proposed mission. The Aerosol-Cloud-Ecosystems (ACE, 2016) mission was already recommended by the National Research Council with the intent of assessing on a daily basis the global distribution of ice clouds, which affect the Earth's emission of IR energy into space and its reflection and absorption of the Sun's energy over broad areas. However, the mission concept is rapidly evolving and a new mission architecture is being conceived, the Cloud Convection Aerosol Precipitation (CCAP) mission.

4   SENSORS PLANNED FOR THE NEAR FUTURE

The future development of quantitative precipitation estimates from satellite observations is pursued in the near future with a twofold strategy, foreseeing both the continuation of operational missions for hydrometeorological applications and the development of innovative sensors. This section summarizes the planned activities of the main space agencies as reported by the Coordination Group for Meteorological Satellites (CGMS, 2018) and by the Satellite Status web page maintained by WMO on behalf of CGMS (http://www.wmo.int/pages/prog/sat/satellitestatus.php).

EUMETSAT is continuing the development of the Meteosat Third Generation (MTG) satellite system, whose operational exploitation is planned in the 2021-2042 timeframe (https://www.eumetsat.int/website/home/Satellites/FutureSatellites/MeteosatThirdGeneration/index.html). Six new geostationary satellites will be launched from 2021 within the MTG program, including four imaging satellites (MTG-I) (20 years of operational services expected) and two sounding satellites (MTG-S) (15.5 years of operational services expected). The configuration foresees three in-orbit satellites with a prime MTG-I satellite delivering the full disk service, a second MTG-I satellite for the RSS, and an MTG-S satellite providing the new sounding services. The full disk service will be provided at improved temporal and spatial resolutions through the Flexible Combined Imager (FCI) with a basic repeat cycle of 10 min, as well as the European Regional-Rapid-Scan (RRS), which covers one-quarter of the full disc, and will be performed at a repeat cycle of 2.5 min. The FCI will take measurements in 16 channels, eight placed in the solar spectral domain between 0.4 and 2.2 µm, delivering data with a 1 km spatial resolution, and eight channels in the thermal spectral domain between 3.8 and 13.3 µm, delivering data with a 2 km spatial resolution. In the RRS mode two channels in the solar domain will be disseminated with the spatial resolution of 0.5 km, whereas other two channels in the IR will have a spatial resolution of

_____

1 km. The MTG-I platforms will host also a new Lighting Imager sensor (LI). MTG-S will carry a hyperspectral Infrared Sounder (IRS) to provide information on horizontally, vertically, and temporally resolved water vapor and temperature structures (full disk coverage every 60 min, Europe region in 30 min). IRS will work over Europe in synergy with the Copernicus Sentinel-4 instrument Ultraviolet, Visible and Near-Infrared Sounding (UVN) designed for geostationary chemistry applications.

The continuation of the GEO satellite constellation activities will be ensured by the other main space agencies as well. The availability of the GOES satellite system will be extended by NASA-NOAA through 2036 by means of GOES-T and -U satellites. In 2018 JMA started considering the next geostationary satellite program, scheduling by 2023 the beginning of manufacturing the GEO satellites that will be the successors to Himawari-8 and -9, and aiming to put them into operation around 2029. The second generation of the GEO FY-4 series operated by CMA is expected to continue until 2030 with the FY-4 B/C/D/E satellites. An upgraded version of the AGRI sensor is expected, by introducing additional channels at 7.24-7.60 μm and at 2.1 and 3.5 μm (spatial resolution 2 km).

The second-generation of the EUMETSAT Polar System (EPS-SG) program will provide a continuation and enhancement of the service from the mid-morning polar orbit in the 2021-2040 timeframe. The EPS-SG will deploy two platforms, i.e. MetOp-SG A and B (Accadia et al., 2016), providing a new support to precipitation estimate through the Microwave Sounder (MWS) on board to MetOp-SG A, the Microwave Imager (MWI) and the Ice Cloud Imager (ICI) both carried on MetOp-SG B satellites. MWS is a cross-track scanning radiometer with a direct heritage from the microwave instruments AMSU-A and MHS on board EPS and NOAA satellites. Its channels from 23.8 to 229 GHz are similar to the ones of the ATMS on board the NOAA/NASA SNPP satellite with the additional channel at 229 GHz to provide information on cirrus clouds. An innovative set of channels in the oxygen absorption band near 50-60 GHz and 118 GHz will enable the retrieval of low precipitation and snowfall by MWI, a conical scanning radiometer with a spectral coverage from 18 to 183 GHz. The ICI is a millimeter and sub-millimeter wave conically scanning radiometer with 11 channels from 183 GHz to 664 GHz (Buehler et al., 2012). Complementarily to the MWI instrument, ICI will measure primarily ice clouds, providing also vertical profiles of hydrometeors (cloud ice, graupel, snow, rain and cloud liquid), instrumental for the solid precipitation retrieval.

The NOAA-NASA collaborative program Joint Polar Satellite System (JPSS) is the new generation of US polar-orbiting operational environmental satellites in the early afternoon sun-synchronous orbit. The JPSS satellite series started in 2011 with the launch of the SNPP mission recently followed by the JPSS-1/NOAA-20 satellite (2017). For the next future the program will proceed with the JPSS-2, 3, and 4 missions tentatively planned for launch in 2022, 2026, and 2031, respectively. With respect to the precipitation estimate, JPSS missions will ensure the continuation of the ATMS acquisitions started since the SNPP mission.

The second-generation LEO satellites FY-3 of CMA are expected to continue beyond 2024 through a sequence of satellites positioned in the early-morning, morning, and afternoon polar orbits (from the FY-3 E up to FY-3 H), providing continuity to the observations of the MWHS-2 and MWRI instruments for the precipitation retrieval. Another CMA satellite program foresees the deployment of a series of operational satellite at low-inclination specifically addressing precipitation observation in continuity with the GPM mission concept, i.e. the FY-3 Rainfall Measurement (FY-3RM). The satellite payload should include the MWRI and MWHS sensors together with a double frequency Ku/Ka precipitation radar and the time frame of the program would be 2020-2028.

Considering the satellite active sensors, the joint European Space Agency (ESA)/JAXA mission EarthCARE is expected to be launched in 2022. EarthCARE can be considered an evolution of the

very successful CloudSat and CALIPSO joint activity within the frame of the A-Train mission (Illingworth et al., 2015). EarthCARE will carry four instruments on a single platform in a 393-km orbit, among which the 355-nm high-spectral-resolution lidar and the CPR at 94.05 GHz, the first satellite radar with Doppler capability. This unique feature will allow for collecting information on convective motions as well as ice and rain fall speeds, leading to improved retrievals of drizzle, rainfall, and snowfall rates. Moreover, the additional 7 dB of sensitivity (a factor of 5) compared with the CloudSat radar will enable a better detection of thin ice clouds and much more low-level stratus and stratocumulus clouds.

5 REQUIREMENTS FOR FUTURE MISSIONS AND RECOMMENDATIONS

Understanding and predicting changes in weather, hydrology, and the climate system is a complex task, which underlies different needs as to the frequency of observations, their timeliness, their resolution and their uncertainty. We will now briefly examine the different requirements in order to receive some guidance for future mission design.

Weather monitoring and forecasting is a complex task that does not easily reduce to a unique set of requirements, as there is great dependence on the application area: global NWP, high resolution NWP, nowcasting, agricultural meteorology, and ocean state forecasts. The WMO OSCAR is the reference for the requirements expressed in terms of six criteria: uncertainty, horizontal resolution, vertical resolution, observing cycle, timeliness and stability. For each criterion three values are indicated: threshold (minimum value to be met for the data to be useful), breakthrough (intermediate level representing a significant improvement for the targeted application), and goal (requirement above which no further improvements are necessary). If one examines the OSCAR tables for surface precipitation intensity (liquid or solid), the values associated with "goal" capabilities vary in the following way: horizontal resolution (from 0.25 km of agricultural meteorology to 5 km of global NWP), observing cycle (from 5 min for nowcasting and ocean to 60 min of global NWP), timeliness (from 5 min of nowcasting and ocean to 15 min of high resolution NWP), uncertainty (0.1 mm h^{-1} for all applications). The confidence level for liquid precipitation in all these cases is between firm (result of impact studies on actual data used in actual applications) and reasonable (not firm, but based on a strong heritage of experiments with similar data). In the case of solid precipitation intensity at the surface, the confidence level for high resolution NWP is only tentative (positive impact expected but not yet validated due to lack of suitable data). From this analysis, it is clear that the improvement of future precipitation missions with regard to observing cycle, resolution, timeliness and uncertainty level are deemed necessary. Because requirements focus on parameters rather than on individual missions, the overarching goals in the case of precipitation tend to focus both on high quality individual products as well as merged products. Note that robustness of the constellation of passive and active sensors in orbit is a key issue for ensuring the necessary continuity of products (Huffman et al., 2016).

Hydrologic predictions try to meet the fundamental societal need for water, which remains insecure in large portions of the Earth. Needs vary from monitoring and predicting water availability in water-scarce areas (especially developing countries) to ensuring an efficient use of water where it is often used without adequate plans (most of the industrialized countries). Accurate observations are thus a key element of hydrologic predictions (e.g., Lettenmaier, 2017). The US Decadal Survey (2017) underlines the importance of monitoring and modeling the water cycle "…from the accurate quantification of water and energy fluxes at the river basin scale, to accurate snow water equivalent

measurements for water supply forecasting, to improved drought monitoring, to flash flooding hazard prediction, to changes in land use and water quality in highly coupled human-natural systems". And it stretches from recommendations to extend ongoing measurements, to new endeavors in detecting the phase (rain or snow) of precipitation, to measuring snow water equivalent and evapotranspiration, to new fields for application of remotely sensed data, such as water quality, groundwater recharge, effects of urbanization, water modulated biogeochemical cycling, and prediction of hazard chains. Improvements in our observing capabilities from space relate not only to precipitation (rainfall and snowfall), but snow water equivalent (still quite elusive especially in mountain areas in spite of our ability to estimate snow cover), evapotranspiration, snow and ice melt, and recharge and withdrawal of groundwater. Advances are planned in the areas of precipitation, river discharge, evapotranspiration, total storage estimates, soil moisture, and surface water storage (lakes, wetlands and reservoirs) (Lettenmaier et al., 2015), while the US Decadal Survey (2017) further highlights the need for snow water equivalent measurements. It is thus very relevant to conceive new precipitation missions along a future refinement of other present key hydrology-related missions such as the Gravity Recovery and Climate Experiment (GRACE), and the Soil Moisture and Ocean Salinity (SMOS) and Soil Moisture Active Passive (SMAP), or even the Snow Water Equivalent mission that is possible from the Decadal Survey recommendations. This will allow for a much more integrated view of precipitation in the Earth System, as well as monitoring of extreme precipitation in the context of its causes and consequences.

A better understanding of the climate system is critical for global change sustainability and thus for long term decision making. The World Climate Research Program (WCRP) has identified seven Grand Challenges in climate science (https://www.wcrp-climate.org/grand-challenges/grand-challengesoverview), including three that are directly related to observations of precipitation. These include "understanding and predicting the extreme weather", "clouds, circulation and climate sensitivity" and "water for the food baskets of the world". Each of these challenges, in turn, can be addressed in three steps: monitoring the Earth, understanding the process, and improving predictions (Weatherhead et al., 2017). For the first two of them, the contribution of satellite observations is expected to be paramount, while further combination of observation and numerical model research is important for the third step. These scientific/societal demands are broken down into specific science questions, such as: How does climate change affect precipitation, i.e. "is the total rainfall amount increasing?" or "is the extreme rainfall event increasing?" Another question is: "how climate change affects the global water cycle?" To answer these questions, a deeper understanding of each element of the atmospheric water budget (e.g., water vapor, clouds and precipitation), hydrological processes (e.g., runoff, floods and droughts, and biogeoscience aspects such as vegetation and forest), must be combined into a unified view. In particular, it will become necessary to better understand clouds and precipitation processes, which will, in turn, require observations of the process of changes from clouds to precipitation, as well as coincident three-dimensional kinematic observation of convective processes. At the same time future observations will need to address fundamental questions that are still not completely answered on: frequency of rain and snow episodes (e.g., Trenberth and Zhang, 2018); intensity and phase (e.g., Trenberth et al. 2003); frequency and distribution of extremes. Naturally, not all global precipitation products are suitable for each of the tasks described above. Guidance is needed by the satellite precipitation community on the use of such data sets in data assimilation, model validation and verification and for improving physical parameterizations (e.g., Tapiador et al., 2017, 2019). One key aspect that underlies all aspects of climate and climate change is the need for long-term precipitation records that have been collected for more than 20 years by the TRMM-GPM missions. To extract changes in precipitation due to climate change by observation, accurate long-term (more than 30 years) data are necessary

_____

to reduce the effect of long-term variation of the earth (El Niño Southern Oscillation-ENSO, solar cycle, Arctic Oscillation, etc.). Given the time series that is available today, a significant requirement is thus to maintain and extend this time series of high-quality precipitation observations. The plan for the proposed implementation of a global observing system for climate was devised by the Global Climate Observing System (GCOS, 2016) guiding the development of such a system and setting out what is needed to meet increasing and more diverse needs for data and information, including for improved management of the impacts and consequences of climate variability and current and future climate change.

In recent years it has become increasingly clear that direct contributions to societal needs other than meteorology, hydrology and climate are also required (e.g., Kucera et al., 2013; Kirschbaum et al., 2017; Skofronick-Jackson et al., 2017) as the mission of the Earth observation satellite, and construction of a data system for precipitation information on a real time basis is also required for the future mission. At the same time, the development plan should fit the 2030 Agenda for Sustainable Development and the Sustainable Development Goals (SDGs) set up by the Committee on Earth Observation Satellites (CEOS) towards a sustainable society (Paganini et al. 2018). Each goal includes a set of targets countries are working to achieve by 2030. Each target in turn includes a set of indicators that define the quantitative measurement for the targets. Satellites, small satellites in particular, contribute to reaching the goals and to monitor the progress towards the targets (Wood and Stober, 2018; Madry et al., 2018). Outstanding examples of societal needs met by precipitation products are, among others: landslide potential, fire monitoring, high-resolution estimates of terrestrial surface heat and moisture, pests and disease control (vector- and water-borne), agriculture and food production (fight against famine), influence on ocean salinity, and atmospheric aerosol scavenging.

The WMO Integrated Global Observing System (WIGOS; WMO, 2017) has recently anticipated the general trends of the evolution of user requirements in 2040 for space missions in support of weather, water, climate and related environmental applications. It is expected that users will require:

- higher resolution observations, better temporal and spatial sampling/coverage,
- improved data quality and consistent uncertainty characterization of the observations,
- novel data types, allowing insight into Earth system processes hitherto poorly understood,
- efficient and interoperable data representation, given the exponential growth of data volumes.

As to precipitation, in particular, the WIGOS document underlines that "sub-mm imagery for cloud microphysical observations (e.g., phase detection) will be beneficial for cloud modelling and atmospheric water cycle modelling". At the same time, "combinations of active and passive measurements with formation-flying spacecraft provide novel insight into physical processes in the atmosphere: one could also expect that those measurements would help to better define atmospheric initial conditions for numerical modelling; better coverage in space and time with such measurements will be beneficial for capturing rapid hydrological processes such as the temporal evolution of water vapour fields and clouds".

In summary for precipitation, the need for a better definition of the atmospheric state and the vertical structure of clouds and precipitation (Stephens and Kummerow, 2007) to improve the quality of the information extracted from satellite observations is the overarching reason for combining multiple frequency active and passive measurements that offers some hope for constraining the atmospheric states needed to derive unique rain and snow rate signals. Radar improvements and the launch of constellations of high-quality radiometers for an adequate space-time sampling are likely to provide the observations needed for a substantial step forward in the quality of the retrieval algorithms.

_____

This framework will surely evolve from the above concepts to meet the above described needs for a precipitation-oriented constellation of satellites. While the missions may not be fully mature (or at least not mature enough to have a timeline associated with them), the goals are well defined, and the community is moving forward from the scientific and technological points of view.

6 REFERENCES

Accadia, C., S. Di Michele, V. Mattioli, J. Ackermann, S. Thonipparambil, and P. Schlüssel, 2016: Next generation of EUMETSAT microwave imagers and sounders: new opportunities for cloud and precipitation retrieval. 8th IPWG and 5th IWSSM Joint Workshop, 3-7 October, Bologna-Italy. [http://ipwg.isac.cnr.it/meetings/bologna-2016/Bologna2016_Orals/2-4_Accadia.pdf]

ACE 2016: ACE 2011-2015 Progress report and future outlook. NASA Earth Sci. Decadal Survey Studies, GSFC, 154 pp. [https://acemission.gsfc.nasa.gov/documents/ACE_5YWP-FINAL_Redacted.pdf]

Adhikari, A., C. Liu, and M. S. Kulie, 2018: Global distribution of snow precipitation features and their properties from 3 years of GPM observations. J. Climate, 31, 3731-3754, doi:10.1175/JCLI-D-17-0012.1.

Adler, R. F., M. R. P. Sapiano, G. J. Huffman, J.-J. Wang, G. Gu, D. Bolvin, L. Chiu, U. Schneider, A. Becker, E. Nelkin, P. Xie, R. Ferraro, and D.-B. Shin, 2018: The Global Precipitation Climatology Project (GPCP) monthly analysis (New Version 2.3) and a review of 2017 global precipitation. Atmosphere, 9, 138, doi:10.3390/atmos9040138.

Battaglia, A., C. D. Westbrook, S. Kneifel, P. Kollias, N. Humpage, U. Löhnert, J. Tyynelä, and G. W. Petty, 2014: G band atmospheric radars: New frontiers in cloud physics. Atmos. Meas. Tech., 7, 1527-1546, doi:10.5194/amt-7-1527-2014.

Behrangi, A., K.-L. Hsu, B. Imam, and S. Sorooshian, 2010: Daytime precipitation estimation using bispectral cloud classification system. J. Appl. Meteor. Climatol., 49, 1015-1031, doi:10.1175/2009JAMC2291.1.

Blackwell, W. J., S. A. Braun, R. Bennartz, C. Velden, M. DeMaria, R. Atlas, J. Dunion, F. Marks, R. Rogers, B. Annane, and R. V. Leslie, 2018: An overview of the TROPICS NASA Earth Venture Mission. Quart. J. Roy. Meteor. Soc., 144 (S1), 16-26, doi:10.1002/qj.3290.

Buehler, S. A., E. Defer, F. Evans, S. Eliasson, J. Mendrok, P. Eriksson, C. Lee, C. Jiménez, C. Prigent, S. Crewell, Y. Kasai, R. Bennartz, and A. J. Gasiewski, 2012: Observing ice clouds in the submillimeter spectral range: the CloudIce mission proposal for ESA's Earth Explorer 8. Atmos. Meas. Tech., 5, 1529-1549, doi:10.5194/amt-5-1529-2012.

Casella, D., L. Martins Costa do Amaral, S. Dietrich, A. C. Marra, P. Sanò, and G. Panegrossi, 2017: The Cloud Dynamics and Radiation Database algorithm for AMSR2: Exploitation of the GPM observational dataset for operational applications. IEEE J. Sel. Topics Appl. Earth Obs. Remote Sens., 10, 3985-4001, doi:10.1109/JSTARS.2017.2713485.

Casella, D., G. Panegrossi, P. Sanò, A. C. Marra, S. Dietrich, B. T. Johnson, and M. S. Kulie, 2017: Evaluation of the GPM-DPR snowfall detection capability: Comparison with CloudSat-CPR. Atmos. Res., 197, 64-75, doi:10.1016/j.atmosres.2017.06.018.

CGMS, 2018: Report of the 46th Plenary Session of the Coordination Group for Meteorological Satellites (CGMS). 3-8 June, Bengaluru, India, 259, pp. [available at https://www.cgms-info.org/documents/CGMS-46_FINAL.pdf].

Chase, R. J., J. A. Finlon, P. Borque, G. M. McFarquhar, S. W. Nesbitt, S. Tanelli, O. O. Sy, S. L. Durden, and M. R. Poellot, 2018: Evaluation of triple-frequency radar retrieval of snowfall properties using coincident airborne in situ observations during OLYMPEX. Geophys. Res. Lett., 45, 5752–5760, doi:10.1029/2018GL077997.

Decadal Survey, (Ed.), 2017: Thriving on our changing planet: A decadal strategy for Earth observation from space. The National Academies Press, 716 pp, doi:10.17226/24938.

Dinku, T., S. Chidzambwa, P. Ceccato, S. J. Connor, and C. F. Ropelewski, 2008: Validation of high-resolution satellite rainfall products over complex terrain. Int. J. Remote Sens., 29, 4097-4110, doi:10.1080/01431160701772526.

Ebtehaj, A. M., and C. D. Kummerow, 2017: Microwave retrievals of terrestrial precipitation over snow-covered surfaces: A lesson from the GPM satellite. Geophys. Res. Lett., 44, 6154–6162, doi:10.1002/2017GL073451.

Esper, J., D. Wu, B. Abresch, B. Flaherty, C. Purdy, J. Hudeck, J. Rodriguez, T. Daisey, S. Heatwole, R. Stancil, T. Johnson, A. Coleman, N. Ehsan, K. Horgan, and J. Piepmeier, 2018: NASA IceCube: CubeSat demonstration of a commercial 883-GHz cloud radiometer. 32nd Annual AIAA/USU Conf. on Small Satellites, Salt Lake City, UT, 4-9 Aug. [https://digitalcommons.usu.edu/cgi/viewcontent.cgi?article=4063&context=smallsat]

Funk, C., P. Peterson, M. Landsfeld, D. Pedreros, J. Verdin, S. Shukla, G. Husak, J. Rowland, L. Harrison, A. Hoell, and J. Michaelsen, 2015: The climate hazards infrared precipitation with stations—a new environmental record for monitoring extremes. Sci. Data, 2, 150066, doi:10.1038/sdata.2015.66.

GCOS, 2016: The global observing system for climate: Implementation needs. WMO, GCOS-200, 315 pp. [https://gcos.wmo.int/en/gcos-implementation-plan]

Guilloteau, C., E. Foufoula-Georgiu, C. D. Kummerow, and V. Petković, 2018: Resolving surface rain from GMI high-frequency channels: Limits imposed by the three-dimensional structure of precipitation. J. Atmos. Oceanic Technol., 35, 1835-1847, doi:10.1175/JTECH-D-18-0011.1.

Haynes, J. M., T. S. L'Ecuyer, G. L. Stephens, S. D. Miller, C. Mitrescu, N. B. Wood, and S. Tanelli, 2009: Rainfall retrieval over the ocean with spaceborne W-band radar. J. Geophys. Res., 114, D00A22, doi:10.1029/2008JD009973.

Hou, A. Y., R. K. Kakar, S. A. Neeck, A. Azarbarzin, C. D. Kummerow, M. Kojima, R. Oki, K. Nakamura, and T. Iguchi, 2014: The Global Precipitation Measurement mission. Bull. Amer. Meteor. Soc., 95, 701-722, doi:10.1175/BAMS-D-13-00164.1.

Huffman, G. J., R. Ferraro, C. Kidd, V. Levizzani, and F. J. Turk, 2016: Requirements for a robust precipitation constellation. 14th Specialist Meeting on Microwave Radiometry and Remote Sensing of the Environment, MicroRad, Espoo, Finland, 11-14 Apr., doi:10.1109/MICRORAD.2016.7530500.

Illingworth, A. J., H. W. Barker, A. Beljaars, M. Ceccaldi, H. Chepfer, N. Clerbaux, J. Cole, J. Delanoë, C. Domenech, D. P. Donovan, S. Fukuda, M. Hirakata, R. J. Hogan, A. Huenerbein, P. kollias, T. Kubota, T. Nakajima, T.Y. Nakajima, T. Nishizawa, Y. Ohno, H. Okamoto, R. Oki, K. Sato, M. Satoh, M. W. Shephard, A. Velázquez-Blázquez, U. W. Andinger, T. Wehr, and G.-J. van Zadelhoff, 2015: The EarthCare satellite: The next step forward in global measurements of clouds, aerosols, precipitation, and radiation. Bull. Amer. Meteor. Soc., 96, 1311-1332, doi:10.1175/BAMS-D-12-00227.1.

Kidd, C., and G. J. Huffman, 2011: Review – Global precipitation measurement. Meteor. Appl., 18, 334-353, doi:10.1002/met.284.

Kidd, C., and V. Levizzani, 2011: Status of satellite precipitation retrievals. Hydrol. Earth Syst. Sci., 15, 1109-1116, doi:10.5194/hess-15-1109-2011.

Kidd, C., V. Levizzani, and S. Laviola, 2010: Quantitative precipitation estimation from Earth observation satellites. In: Rainfall: State of the science, F. Testik and M. Gebremichael, Eds., AGU, Geophysical Monograph Series, 191, ISBN 978-0-87590-481-8, 127-158.

Kidd, C., A. Becker, G. J. Huffman, C. L. Muller, P. Joe, G. Skofronick-Jackson, and D. B. Kirschbaum, 2017: So, how much of the Earth's surface is covered by rain gauges? Bull. Amer. Meteor. Soc., 98, 69-78, doi:10.1175/BAMS-D-14-00283.1.

Kirschbaum, D. B., G. J. Huffman, R. F. Adler, S. Braun, K. Garrett, E. Jones, A. McNally, G. Skofronick-Jackson, E. Stocker, H. Wu, and B. F. Zaitchik, 2017: NASA's remotely sensed precipitation: A reservoir for applications users. Bull. Amer. Meteor. Soc., 98, 1169-1198, doi:10.1175/BAMS-D-15-00296.1.

Kongoli, C., H. Meng, J. Dong, and R. R. Ferraro, 2018: A hybrid snowfall detection method from satellite passive microwave measurements and global weather forecast models. Quart. J. Roy. Meteor. Soc., 144 (S1), 120-132, doi:10.2002/qj3270.

Kucera, P. A., E. E. Ebert, F. J. Turk, V. Levizzani, D. B. Kirschbaum, F. J. Tapiador, A. Loew, and M. Borsche, 2013: Precipitation from space: Advancing Earth system science. Bull. Amer. Meteor. Soc., 94, 365-375, doi:10.1175/BAMS-D-11-00171.1.

Kulie, M. S., and L. Milani, 2018: Seasonal variability of shallow cumuliform snowfall: A CloudSat perspective. Quart. J. Roy. Meteor. Soc., 144(S1)329-343, doi:10.1002/qj.3222.

Kulie, M. S., L. Milani, N. B. Wood, S. A. Tushaus, R. Bennartz, and T. S. L'Ecuyer, 2016: A shallow cumuliform snowfall census using spaceborne radar. J. Hydrometeor., 17, 1261-1279, doi:10.1175/JHM-D-15-0123.1.

Kummerow, C. D., W. Barnes, T. Kozu, J. Shiue, and J. Simpson, 1998: The Tropical Rainfall Measuring Mission (TRMM) sensor package. J. Atmos. Oceanic. Technol., 15, 809-817, doi:10.1175/1520-0426(1998)015%3C0809:TTRMMT%3E2.0.CO;2.

Kummerow, C. D., D. L. Randel, M. S. Kulie, N.-Y. Wang, R. R. Ferraro, S. J. Munchak, and V. Petkovic, 2015: The evolution of the Goddard Profiling Algorithm to a fully parametric scheme. J. Atmos. Oceanic Technol., 32, 2265-2280, doi:10.1175/JTECH-D-15-0039.1.

Kummerow, C. D., J. Simpson, O. Thiele, W. Barnes, A. T. C. Chang, E. F. Stocker, R. F. Adler, A. Y. Hou, R. Kakar, F. Wentz, P. Ashcroft, T. Kozu, Y. Hong, K. Okamoto, T. Iguchi, H. Kuroiwa, E. Im, Z. S. Haddad, G. J. Huffman, B. Ferrier, W. S. Olson, E. Zipser, E. A. Smith, T. T. Wilheit, G. North, T. Krishnamurti, and K. Nakamura, 2000: The status of the Tropical Rainfall Measuring Mission (TRMM) after two years in orbit. J. Appl. Meteor., 39, 1965-1982, doi:10.1175/1520-0450(2001)040<1965:TSOTTR>2.0.CO;2.

Laviola, S., J. Dong, C. Kongoli, H. Meng, R. R. Ferraro, and V. Levizzani, 2015: An intercomparison of two passive microwave algorithms for snowfall detection over Europe. IEEE Int. Geoscience Remote Sens. Symp. (IGARSS), Volume 2015-November, 886-889, doi:10.1109/IGARSS.2015.7325907.

Lettenmaier, D. P., 2017: Observational breakthroughs lead the way to improved hydrological predictions. Water Resour. Res., 53, 2591–2597, doi:10.1002/2017WR020896.

Lettenmaier, D. P., D. Alsdorf, J. Dozier, G. J. Huffman, M. Pan, and E. F. Wood, 2015: Inroads of remote sensing into hydrologic science during the WRR era. Water Resour. Res., 51, 7309-7342, doi:10.1002/2015WR017616.

Levizzani, V., S. Laviola, and E. Cattani, 2011: Detection and measurement of snowfall from space. Remote Sens., 3, 145-166, doi:10.3390/rs3010145.

Levizzani, V., C. Kidd, D. B. Kirschbaum, C. D. Kummerow, K. Nakamura, and F. J. Turk, (Eds.), 2019: Satellite precipitation measurement. Springer Nature, Dordrecht, 1339 pp, in press.

Levizzani, V., C. Kidd, K. Aonashi, R. Bennartz, R. R. Ferraro, G. J. Huffman, R. Roca, F. J. Turk, and N.-Y. Wang, 2018: The activities of the International Precipitating Working Group. Quart. J. Roy. Meteor. Soc., 144 (S1), 3-15, doi:10.1002/qj.3214.

Liu, G., 2008a: A database of microwave single-scattering properties for nonspherical ice particles. Bull. Amer. Meteor. Soc., 89, 1563-1570, doi:10.1175/2008BAMS2486.1.

Liu, G., 2008b: Deriving snow cloud characteristics from CloudSat observations. J. Geophys. Res., 113, D00A09, doi:10.1029/2007JD009766.

Madry S., P. Martinez, and R. Laufer R., 2018: Small satellites and the U.N. sustainable development goals. In: Innovative Design, Manufacturing and Testing of Small Satellites, 65-79, Springer Praxis Books, Springer, Cham, doi:10.1007/978-3-319-75094-1_5.

Marra, F., E. I. Nikolopoulos, E. N. Anagnostou, A. Bárdossy, and E. Morin, 2019: Precipitation frequency analysis from remotely sensed datasets: A focused review. J. Hydrol., 574, 699-705, doi:10.1016/j.jhydrol.2019.04.081.

Mazzoglio, P., F. Laio, S. Balbo, P. Boccardo, and F. Disabato, 2019: Improving an extreme rainfall detection system with GPM IMERG data. Remote Sens., 11, 677, doi:10.3390/rs11060677.

Meng, H., J. Dong, R. R. Ferraro, B. Yan, L. Zhao, C. Kongoli, N.-Y. Wang, and B. Zavodsky, 2017: A 1DVAR-based snowfall rate retrieval algorithm for passive microwave radiometers. J. Geophys. Res., 122, doi:10.1002/2016JD026325.

Michaelides, S., V. Levizzani, E. N. Anagnostou, P. Bauer, T. Kasparis, and J. E. Lane, 2009: Precipitation: Measurements, remote sensing, climatology and modeling. Atmos. Res., 94, 512-533, doi:10.1016/j.atmosres.2009.08.017.

Milani, L., M. S. Kulie, D. Casella, S. Dietrich, T. S. L'Ecuyer, G. Panegrossi, F. Porcù, P. Sanò, and N. B. Wood, 2018: CloudSat snowfall estimates over Antarctica and the Southern Ocean: An assessment of independent retrieval methodologies and multi-year snowfall analysis. Atmos. Res., 213, 121-135, doi:10.1016/j.atmosres.2018.05.015.

Palerme, C., C. Claud, N. B. Wood, T. L'Ecuyer, and C. Genthon, 2019: How does ground clutter affect CloudSat snowfall retrievals over ice sheets? IEEE Geosci. Remote Sensing Lett., 16, 342-346, doi:10.1109/LGRS.2018.2875007.

Panegrossi, G., J.-F. Rysman, D. Casella, A. C. Marra, P. Sanò, and M. S. Kulie, 2017: CloudSat-based assessment of GPM Microwave Imager snowfall observation capabilities. Remote Sens., 9(12), 1263, doi:10.3390/rs9121263.

Peral, E., T. Imken, J. Sauder, S. Statham, S. Tanelli, D. Price, N. Chahat, and A. Williams, 2017: RainCube, a Ka-band Precipitation Radar in a 6U CubeSat. 31st Annual AIAA/USU Conf. on Small Satellites, Logan, UT, Aug 31-3 Sept., SSC17-III-03. [https://digitalcommons.usu.edu/cgi/viewcontent.cgi?article=3611&context=smallsat]

Peral, E., E. Im, L. Wye, S. Lee, S. Tanelli, Y. Rahmat-Samii, S. Horst, J. Hoffman, S.-H. Yun, T. Imken, and D. Hawkins, 2018: Radar technologies for Earth remote sensing from CubeSat platforms. Proc. IEEE, 106, 404-418, doi:10.1109/JPROC.2018.2793179.

Prigent, C., F. Aires, and W. B. Rossow, 2006: Land surface microwave emissivities over the globe for a decade. Bull. Amer. Meteor. Soc., 87, 1573-1584, doi:10.1175/BAMS-87-11-1573.

Rasmussen, R. M., B. Baker, J. Kochendorfer, T. Meyers, S. Landolt, A. P. Fischer, J. Black, J. M. Theriault, P. A. Kucera, D. Gochis, C. Smith, R. Nitu, M. Hall, K. Ikeda, and E. Gutmann, 2012: How well are we measuring snow? Bull. Amer. Met. Soc., 93, 811-829, doi:10.1175/BAMS-D-11-00052.1.

Reising, S. C., P. Kangaslahti, E. Schlecht, J. Jiang, X. Bosch-Lluis, M. Ogut, Y. Goncharenko, S. Padmanabhan, R. Cofield, N. Chahat, S. T. Brown, W. Deal, A. Zamora, K. Leong, S. Shih, and G. Mei, 2016: Tropospheric water and cloud ICE (TWICE) millimeter and submillimeter-wave

radiometer instrument for 6U-Class nanosatellites. 41st Int. Conf. Infrared, Millimeter and Terahertz Waves (IRMMW-THz), Copenhagen, Denmark, 25-30 Sept., doi:10.1109/IRMMW-THz.2016.7758396.

Reising, S. C., T. C. Gaier, C. D. Kummerow, S. Padmanabhan, B. H. Lim, C. Heneghan, W. K. Berg, V. Chandrasekar, J. P. Olson, S. T. Brown, J. Carvo, and M. Pallas, 2017: Global measurement of temporal signatures of precipitation: Development of the temporal experiment for storms and tropical systems technology demonstration mission. IGARSS 2017, Ft. Worth, TX, 23-28 July, 5931-5933, doi:10.1109/IGARSS.2017.8128359.

Reising, S. C., T. C. Gaier, S. Padmanabhan, B. H. Lim, C. Heneghan, C. D. Kummerow, W. K. Berg, V. Chandrasekar, C. Radhakrishnan, S. T. Brown, J. Carvo, and M. Pallas, 2018: An Earth Venture in-space technology demonstration mission for Temporal Experiment for Storms and Tropical Systems (Tempest). IGARSS 2018, Valencia, Spain, 22-27 July, 6301-6303, doi:10.1109/IGARSS.2018.8517330.

Rysman, J.-F., G. Panegrossi, P. Sanò, A. C. Marra, S. Dietrich, L. Milani, and M. S. Kulie, 2018: SLALOM: An all-surface snow water path retrieval algorithm for the GPM Microwave Imager. Remote Sens., 10, 1278, doi:10.3390/rs10081278.

Sanò, P., G. Panegrossi, D. Casella, A. C. Marra, F. Di Paola, and S. Dietrich, 2016: The new Passive microwave Neural network Precipitation Retrieval (PNPR) algorithm for the cross-track scanning ATMS radiometer: Description and verification study over Europe and Africa using GPM and TRMM spaceborne radars. Atmos. Meas. Tech., 9, 5441-5460, doi:10.5194/amt-9-5441-2016.

Sanò, P., G. Panegrossi, D. Casella, A. C. Marra, L. P. D'Adderio, J.-F. Rysman, and S. Dietrich, 2018: The Passive Microwave Neural Network Precipitation Retrieval (PNPR) algorithm for the conical scanning Global Microwave Imager (GMI) radiometer. Remote Sens., 10, 1122, doi:10.3390/rs10071122.

Shige, S., S. Kida, H. Ashiwake, T. Kubota, and K. Aonashi, 2013: Improvement of TMI rain retrievals in mountainous areas. J. Appl. Meteor. Climatol., 52, 242-254, doi:10.1175/JAMC-D-12-074.1.

Skofronick-Jackson, G., D. B. Kirschbaum, W. A. Petersen, G. J. Huffman, C. Kidd, E. F. Stocker, and R. Kakar, 2018: The Global Precipitation Measurement (GPM) mission's scientific achievements and societal contributions: reviewing four years of advanced rain and snow observations. Quart. J. Roy. Meteor. Soc., 144(S1), 27-48, doi:10.1002/qj.3313.

Skofronick-Jackson, G., W. A. Petersen, W. Berg, C. Kidd, E. F. Stocker, D. B. Kirschbaum, R. Kakar, S. A. Braun, G. J. Huffman, T. Iguchi, P. E. Kirstetter, C. Kummerow, R. Meneghini, R. Oki, W. S. Olson, Y. N. Takayabu, K. Furukawa, and T. Wilheit 2017: The Global Precipitation Measurement (GPM) mission for science and society. Bull. Amer. Meteor. Soc., 98, 1679-1695, doi:10.1175/BAMS-D-15-00306.1.

Smalley, M., T. S. L'Ecuyer, M. D. Lebsock, and J. M. Haynes, 2014: A comparison of precipitation occurrence from the NCEP Stage IV QPE product and the CloudSat Cloud Profiling Radar. J. Hydrometeor., 15, 444-458, doi:10.1175/JHM-D-13-048.1.

Sohn, B. J., G.-H. Ryu, H.-J. Song, and M.-L. Ou, 2013: Characteristic features of warm type rain producing heavy rainfall over the Korean peninsula inferred from TRMM measurements. Mon. Wea. Rev., 141, 3873–3888, doi:10.1175/MWR-D-13-00075.1.

Song, H.-J., and B. J. Sohn, 2015: Two heavy rainfall types over the Korean peninsula in the humid East Asian summer environment: A satellite observation study. Mon. Wea. Rev., 143, 363–382, doi:10.1175/MWR-D-14-00184.1.

Stephens, G. L., and C. D. Kummerow, 2007: The remote sensing of clouds and precipitation from space: A review. J. Atmos. Sci., 64, 3742-3765, doi:10.1175/2006JAS2375.1.

Stephens, G. L., D. G. Vane, R. J. Boain, G. G. Mace, K. Sassen, Z. Wang, A. J. Illingworth, E. J. O'Connor, W. B. Rossow, S. L. Durden, S. D. Miller, R. T. Austin, A. Benedetti, C. Mitrescu, and the CloudSat Science Team, 2002: The CloudSat mission and the A-Train - A new dimension of space-based observations of clouds and precipitation. Bull. Amer. Meteor. Soc.,83, 1771-1790, doi:10.1175/BAMS-83-12-1771.

Stephens, G. L., D. G. Vane, S. Tanelli, E. Im, S. Durden, M. Rokey, D. Reinke, P. Partain, G. G. Mace, R. Austin, T. L'Ecuyer, J. Haynes, M. Lebsock, K. Suzuki, D. Waliser, D. Wu, J. Kay, A. Gettelman, Z. Wang, and R. Marchand, 2008: CloudSat mission: Performance and early science after the first year of operation. J. Geophys. Res., 113, D00A18, doi:10.1029/2008JD009982.

Stephens, G. L., D. Winker, J. Pelon, C. Trepte, D. Vane, C. Yuhas, T. L'Ecuyer, and M. Lebsock, 2018: CloudSat and CALIPSO within the A-Train: Ten years of actively observing the Earth system. Bull. Amer. Meteor. Soc., 99, 569-581, doi:10.1175/BAMS-D-16-0324.1.

Sun, Q., C. Miao, Q. Duan, H. Ashouri, S. Sorooshian, and K.-L. Hsu, 2018: A review of global precipitation data sets: Data sources, estimation, and intercomparisons. Rev. Geophys., 56, 79-107, doi:10.1002/2017RG000574.

Tanelli, S., Z. S. Haddad, E. Im, S. L. Durden, O. O. Sy, G. A. Sadowy, and M. Sanchez-Barbetty, 2018: Radar concepts for the next generation of spaceborne observations of cloud and precipitation processes. IEEE Radar Conference (RadarConf18), Oklahoma City, OK, 1245-1249.

Tao, Y., K.-L. Hsu, A. Ihler, X. Gao, and S. Sorooshian, 2018: A two-stage deep neural network framework for precipitation estimation from bispectral satellite information. J. Hydrometeor., 19, 393-408, doi:10.1175/JHM-D-17-0077.1.

Tapiador, F. J., R. Roca, A. Del Genio, B. Dewitte, W. Petersen, and F. Zhang, 2019: Is precipitation a good metrics for model performance? Bull. Amer. Meteor. Soc., 100, 223-233, doi:10.1175/BAMS-D-17-0218.1.

_____

Tapiador, F. J., F. J. Turk, W. A. Petersen, A. Y. Hou, E. García-Ortega, L. A. T. Machado, C. F. Angelis, P. Salio, C. Kidd, G. J. Huffman, and M. de Castro, 2012: Global precipitation measurement: Methods, datasets and applications. Atmos. Res., 104, 70–97, doi:10.1016/j.atmosres.2011.10.021.

Tapiador, F. J., A. Navarro, V. Levizzani, E. García-Ortega, G. J. Huffman, C. Kidd, P. A. Kucera, C. D. Kummerow, H. Masunaga., W. A. Petersen, R. Roca, J.-L. Sánchez, W.-K. Tao, and F. J. Turk, 2017: Global precipitation measurements for validating climate models. Atmos. Res., 197, 1–20, doi:10.1016/j.atmosres.2017.06.021.

Trenberth, K. E., and Y. Zhang, 2018: How often does it rain? Bull. Amer. Meteor. Soc., 99, 289-298, doi:10.1175/BAMS-D-17-0107.1.

Trenberth, K. E., A. Dai, R. M. Rasmussen, and D. B. Parsons, 2003: The changing character of precipitation. Bull. Amer. Meteor. Soc., 84, 1205-1218, doi:10.1175/BAMS-84-9-1205.

Weatherhead, E. C., B. A. Wielicki, V. Ramaswamy, M. Abbott, T. P. Ackerman, R. Atlas, G. Brasseur, L. Bruhwiler, A. J. Busalacchi, J. H. Butler, C. T. M. Clack, R. Cooke, L. Cucurull, S. M. Davis, J. M. English, D. W. Fahey, S. S. Fine, J. K. Lazo, S. Liang, N. G. Loeb, E. Rignot, B. Soden, D. Stanitski, G. L. Stephens, B. D. Tapley, A. M. Thompson, K. E. Trenberth, and D. Wuebbles, 2017: Designing the climate observing system of the future. Earth's Future, 6, 80-102, doi:10.1002/2017EF000627.

Winker, D. M., J. Pelon, J. A. Coakley Jr., S. A. Ackerman, R. J. Charlson, P. R. Colarco, P. Flamant, Q. Fu, R. M. Hoff, C. Kittaka, T. L. Kubar, H. Le Treut, M. P. McCormick, G. Mégie, L. Poole, K. Powell, C. Trepte, M., A. Vaughan, and B. A. Wielicki, 2010: The CALIPSO Mission: A global 3D view of aerosols and clouds. Bull. Amer. Meteor. Soc., 91, 1211–1229, doi:10.1175/2010BAMS3009.1.

WMO, 2017: Vision for the WIGOS component system in 2040-WIGOS Vision in Space. WMO, IPET-SUP-3/INF 6.1, 16 pp. [http://www.wmo.int/pages/prog/sat/meetings/documents/IPET-SUP-3_INF_06-01_WIGOS-Vision-Space2040-Draft1-1.pdf]

Wood, D., and K. J. Stober, 2018: Small satellites contribute to the United Nation's sustainable development goals. Proc. 32nd Annual AIAA/USU Conf. on Small Satellites, Logan UT, 4-9 Aug., SSC18-WKVIII-08. [https://digitalcommons.usu.edu/smallsat/2018/all2018/437/]

Wood, N. B., and T. S. L'Ecuyer, 2018: Level 2C snow profile process description and interface control document, Product Version P1_R05, NASA JPL CloudSat project document revision 0, 26 pp. [http://www.cloudsat.cira.colostate.edu/sites/default/files/products/files/2C-SNOWPROFILE_PDICD.P1_R05.rev0_.pdf]

Wood, N. B., T. S. L'Ecuyer, A. J. Heymsfield, and G. L. Stephens, 2015: Microphysical constraints on millimeter-wavelength scattering properties of snow particles. J. Appl. Meteor. Climatol., 54, 909-931, doi:10.1175/JAMC-D-14-0137.1.

_____

Xu, W., R. F. Adler, and N.-Y. Wang, 2014: Combining satellite infrared and lightning information to estimate warm-season convective and stratiform rainfall. J. Appl. Meteor. Climatol., 53, 180-199, doi:10.1175/JAMC-D-13-069.1.

Yamamoto, M. K., S. Shige, C.-K. Yu, and L.-W. Cheng, 2017: Further improvement of the heavy orographic rainfall retrievals in the GSMaP algorithm for microwave radiometers. J. Appl. Meteor. Climatol., 56, 2607-2619, doi:10.1175/JAMC-D-16-0332.1.

You, Y., N.-Y. Wang, R. R. Ferraro, and S. Rudlosky, 2017: Quantifying the snowfall detection performance of the GPM Microwave Imager channels over land. J. Hydrometeor., 18, 729-751, doi:10.1175/JHM-D-16-0190.1.

You, Y., C. Peters-Lidard, N.-Y. Wang, F. J. Turk, S. Ringerud, S. Yang, and R. R. Ferraro, 2018: The instantaneous retrieval of precipitation over land by temporal variation at 19 GHz. J. Geophys. Res., 123, 9279–9295, doi:10.1029/2017JD027596.

7 ACRONYMS

ABI	Advanced Baseline Imager
ACE	Aerosol-Cloud-Ecosystems mission
ADEOS	Advanced Earth Observing Satellite
AGRI	Advanced Geostationary Radiation Imager
AHI	Advanced Himawari Imager
AMI	Advanced Meteorological Imager
AMSR-2	Advanced Microwave Scanning Radiometer-2
AMSU-A	Advanced Microwave Sounding Unit–A
ATMS	Advanced Technology Microwave Sounder
CALIOP	Cloud-Aerosol Lidar with Orthogonal Polarization
CALIPSO	Cloud–Aerosol Lidar and Infrared Pathfinder Satellite Observations
CCAP	Cloud, Convection, Aerosol and Precipitation mission
CDRD	Cloud Dynamics and Radiation Database
CEOS	Committee on Earth Observation Satellites
CMA	China Meteorological Administration
CNES	Centre National d'Études Spatiales
COMS	Communication, Ocean, and Meteorological Satellite
CONUS	Conterminous United States
COSMIC-2	Constellation Observing System for Meteorology, Ionosphere and Climate-2
CPR	Cloud Profiling Radar
DMSP	Defense Meteorological Satellite Program
DoD	Department of Defense
ECMWF	European Centre for Medium-range Weather Forecasts
ENSO	El Niño Southern Oscillation
EO	Earth Observation
EOS	Earth Observation System
EPS-SG	EUMETSAT Polar System-Second Generation
ESA	European Space Agency
ESTO	Earth Science Technology Office
EUMETSAT	European Organization for the Exploitation of Meteorological Satellites
EVI-3	Earth Venture-Instrument-3 program
FCI	Flexible Combined Imager
FY	Feng-Yun
FY-3RM	FY-3 Rainfall Measurement
GCM	General Circulation Model
GCOM-W	Global Change Observation Mission for Water
GCOS	Global Climate Observing System
GEO	Geostationary Earth Orbit
GIIRS	Geo Interferometric Infrared Sounder
GK-2A	GEO-KOMPOSAT-2A
GMI	GPM Microwave Imager
GOES	Geostationary Operational Environmental Satellite
GPM	Global Precipitation Measurement mission
GPROF	Goddard Profiling algorithm

GRACE	Gravity Recovery and Climate Experiment
HEMT	High Electron Mobility Transistors
ICI	Ice Cloud Imager
IFOV	Instantaneous Field of View
IODC	Indian Ocean Data Coverage
IPWG	International Precipitation Working Group
IR	Infrared
IRS	IR Sounder
ISRO	Indian Space Research Organization
ISS	International Space Station
IWP	Ice Water Path
JAXA	Japan Aerospace Exploration Agency
JMA	Japan Meteorological Agency
JPL	Jet Propulsion Laboratory
JPSS	Joint Polar Satellite System
KaHS	Ka High Sensitivity scan (GPM)
KaMS	Ka Matched Scan (GPM)
KMA	Korea Meteorological Administration
KOMPSAT-2A	Korea Multi-Purpose Satellite-2
LEO	Low Earth Orbit
LI	Lightning Imager
LMI	Lightning Mapping Imager
MHEMT	Metamorphic HEMT
MHS	Microwave Humidity Sounder
MI	Meteorological Imager
MM	MilliMeter wave radiometer
MSU	Microwave Sounding Unit
MTG	Meteosat Third Generation
MTG-I	Meteosat Third Generation-Imaging
MTG-S	Meteosat Third Generation-Sounding
MW	Microwave
MWHS-2	Micro-Wave Humidity Sounder-2
MWI	Microwave Imager
MWIR	Medium-Wavelength IR
MWRI	Micro-Wave Radiation Imager
MWS	Microwave Sounder
NASA	National Aeronautics and Space Administration
NIR	Near IR
NOAA	National Oceanic and Atmospheric Administration
NWP	Numerical Weather Prediction
OLYMPEX	Olympic Mountain Experiment
OSCAR	Observing Systems Capability Analysis and Review Tool
OSSI	Operational Service Status Indicator
PMW	Passive Microwave
PNPR	Passive microwave Neural network Precipitation Retrieval
PR	Precipitation Radar
PSD	Particle Size Distribution

RainCube	Radar in a CubeSat
RPM	Revolutions Per Minute
RRS	Regional Rapid Scan
RSS	Rapid Scanning Service
SAPHIR	Sondeur Atmosphérique du Profil d'Humidité Intertropicale par Radiométrie
SDG	Sustainable Development Goals
SEP	Space Environment Package
SEVIRI	Spinning Enhanced Visible and Infra-Red Imager
SMAP	Soil Moisture Active Passive
SMOS	Soil Moisture and Ocean Salinity
SSM/I	Special Sensor Microwave/Imager
SSMIS	Special Sensor Microwave-Imager/Sounder
SSM/T	Special Sensor Microwave/Temperature
SNPP	Suomi National Polar-orbiting Partnership
SSP	Sub Satellite Point
SWIR	Short-Wavelength IR
TEMPEST-D	Temporal Experiment for Storms and Tropical Systems–Demonstrator
TIR	Thermal IR
TIROS	Television and Infra-Red Observation Satellite
TMI	TRMM Microwave Imager
TRMM	Tropical Rainfall Measuring Mission
TROPICS	Time-Resolved Observations of Precipitation structure and storm Intensity with a Constellation of Smallsats
TWICE	Tropospheric Water and cloud ICE
UTLS	Upper Tropospheric/Lower Stratospheric
UVN	Ultraviolet, Visible and Near-Infrared Sounding
VIS	Visible
WCRP	World Climate Research Program
WIGOS	WMO Integrated Global Observing System
WMO	World Meteorological Organization

RAINCAST

WP2200 REPORT

Radar and radiometer retrieval algorithms

A. Battaglia[1], G. Panegrossi[2], E. Cattani[2], V. Levizzani[2],
P. Kollias[3], M. Wolde[4]

1. University of Leicester, Leicester UK
2. CNR-ISAC, Italy
3. McGill University, Montreal, Canada
4. NRC Canada

1. INTRODUCTION

In order to derive requisite microphysical, meteorological and climatological parameters from measured quantities such as radar reflectivity, it is necessary to apply an algorithm that relies upon utilizing recognized relationships between the quantities being measured and the parameters being sought. This process constitutes a retrieval, and the derived parameters result from the best fit that the algorithm can provide by operating on the input data. This method of deriving useful parameters from measured quantities may also be applied to spaceborne and airborne radars and radiometers. Such algorithms may function, for example, by applying a straightforward relationship between the measured radar reflectivity and the rain rate (L'Ecuyer and Stephens, 2002). However, such approaches, although relatively easy to implement and generally computationally inexpensive, may encounter difficulties imposed by the assumptions that go into them. In the case of rain, the particular drop size distribution used will have a significant bearing on the nature of the relationship between the rain rate and the reflectivity. An alternative solution that has found favour within many areas including the cases of radiometer- and radar-based retrievals, and hence which has been applied repeatedly and for a variety of situations, e.g. Mitrescu et al. (2010), is the optimal estimation approach (Rogers, 1976; 2000). This method uses a forward model to minimize the cost function, which, for the example of radar-based retrievals, contains among other parameters the measured reflectivity, the modelled reflectivity, an a priori error covariance matrix, and an error covariance matrix associated with the observations. In order for accurate results to be obtained using this method, it is essential that adequate error covariance matrices be used. As such, it is possible to control precisely the information being used in the retrieval problem, by filtering out that which is less reliable. The optimal estimation procedure then seeks the solution through successive iterations and does not require the introduction of a separate inversion model as it only uses the forward model formulation. A clear advantage of such an approach resides in its simplicity, flexibility and universality. Moreover, additional constraints can easily be added or removed from the particular formulation being utilized. However, for complex problems, optimal estimation may become computationally demanding, e.g. for deep cloud structures, since it requires several matrix computations. For example, for the situation deep within the cloud, the effects of multiple scattering become important and the iterative method quickly becomes unstable as the cost function increases dramatically. In this case, the value of the cost function may be used to identify when multiple scattering becomes significant.

The retrieval algorithms utilized by spaceborne and airborne radar and radiometer systems, including the systems used by the CloudSat and GPM missions, will be covered in the rest of this report. Section 2 will cover algorithms used by passive microwave sensors. The discussion following this will then turn to radar-only algorithms using single-frequency (section 3), dual-frequency (section 4) and triple-frequency (section 5) retrieval methods. Covered will be techniques relating to the Cloud Profiling Radar (CPR) aboard the CloudSat satellite, and the Dual-frequency Precipitation Radar (DPR) aboard the GPM Core satellite. This report will conclude its discussion of algorithms with section 6, which covers algorithms relating to a combined radar-radiometer approach. Finally, comparisons between results obtained using different precipitation algorithms are presented in section 7.

2. PASSIVE MICROWAVE PRECIPITATION RETRIEVAL ALGORITHMS

Remote sensing of precipitation from passive microwave radiometers is based on the complex interaction of microwave radiation emitted by the Earth's surface with gases (oxygen and water vapour) and liquid and solid hydrometeors within the clouds.

The emitted radiation from the surface depends on the surface emissivity and surface temperature. The frequency-dependent surface emissivity depends primarily on the dielectric properties of the material and the roughness of the surface (Ulaby et al., 1986). Very large distinctions are visible between ocean, land, and ice/snow covered surfaces. In particular, oceans have relatively low emissivity across the microwave spectrum while for land it is considerably higher (closer to unity) but sensitive to soil moisture, particularly for lower frequencies (i.e. < 10 GHz). Snow- and ice-covered surfaces can vary significantly based on the snow and ice properties.

The incident radiation is absorbed and/or scattered by the atmospheric constituents. The absorption by gases is shown in Figure. 1. There is some continuum absorption, modest for frequencies below 100 GHz, a weak water vapour absorption band at 22.235 GHz, a strongly absorbing oxygen band between 54 and 60 GHz, another oxygen band at 118 GHz and a second, stronger water vapour absorption band at 183.31 GHz.
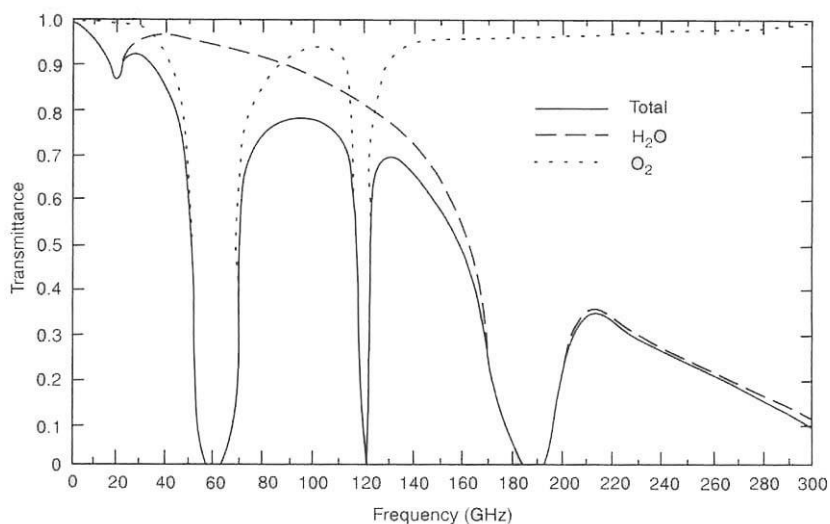
Figure. 1: Atmospheric transmittance (oxygen and water vapour) as a function of frequency in the microwave region. (From An Introduction to Atmospheric Radiation, 2002, Liou, K. N. p. 415.)

For water the dielectric property is responsible for very broad absorption across the microwave frequency range, increasing with frequency, while ice exhibits relatively little absorption, particularly at the lower end of commonly used frequencies (typically < 10 GHz).

As long as water droplets are small compared to the wavelength (generally true for cloud drops in the microwave regime), Rayleigh absorption and scattering apply. In this regime absorption is directly proportional to the liquid water content of the cloud with no sensitivity to drop sizes. This makes it difficult to separate small non-precipitating drops from larger precipitating ones, but makes the retrieval of liquid water content over radiometrically cold oceans relatively straightforward. Scattering is sensitive to the cloud drop sizes but is relatively small for cloud particles and raindrops at frequencies below 30 GHz. Higher frequencies are needed before the scattering signal by liquid hydrometeors can be differentiated from instrument noise or background surface.

For ice particles, the imaginary component of the refractive index is quite small and absorption is negligible. The scattering behaviour is similar to that of water which implies little scattering below 30 GHz but increased effects as the frequency increases.

Once particles get larger, they enter into the Mie (1908) regime. Here, the absorption and scattering relations become more complex. Details of the particle size, shape, and density become important. A number of approaches have been used to compute absorption and scattering parameters for ice particles at microwave frequencies (e.g. Liu, 2004; Kuo et al., 2016).

The earliest attempts to retrieve precipitation from passive microwave sensors in space can be traced back to the Electronically Scanning Microwave Sensor, ESMR, (Wilheit, 1972) aboard the Nimbus-5 Satellite launched in 1972, operating at 19.35 GHz. At this frequency, the ocean appears cold, and water vapour, clouds, and precipitation all act to increase the observed radiances, or warm the brightness temperatures. The early emission-based algorithms tended to use thresholds of a minimum temperature above which the rainfall would be assigned to the pixel based upon the excess Tb above the threshold. At the same time, a number of groups, including Savage and Weinman (1975) began to show that brightness temperatures could be reliably calculated using radiative transfer models for cloud and precipitation. Such studies hinted that more quantitative approaches for rainfall estimation were possible over oceans. With the launch of ESMR on Nimbus-6 in 1975 (Wilheit, 1975), operating at 37 GHz, the first studies investigated the scattering signal observed from space in the presence of intense precipitation, even though it was often not visible over ocean. The next milestone in the development of rainfall algorithms came with the launch of the Scanning Multichannel Microwave Radiometer (SMMR) on Nimbus-7 (Gloerson and Hardis, 1978). SMMR was a 5-channel instrument, with frequencies at 6.6, 10.7, 19.35, 23 and 37 GHz, measuring both horizontal and vertical polarizations at a constant incidence angle of approximately 49° from nadir. Multiple channels on SMMR made it possible to simultaneously retrieve a number of geophysical parameters. With multiple channels and polarizations, a better surface characterization, and the water vapour information from the 23 GHz channel, allowed for more physical retrievals of clouds and precipitation over oceans. Most methods were based on linear regression against a number of channel combinations either based on radiative transfer models (Chang and Milman, 1982), or on empirical approaches Alishouse et al., (1990). From the scattering perspective, Rodgers and Siddalingaiah (1983) used the 37 GHz channels together with theoretical computations performed earlier by Savage and Weinman (1975) to develop a rain classification algorithm over land, exploiting polarization difference (large for wet or water-covered surfaces, and small or zero when the emission is due to rain drops).

Spencer (1986) correctly noted that the 37 GHz of SMMR had a non-unique relationship with precipitation – increasing first as cloud water and light precipitation filled the field of view, and then decreasing again as more and more ice scattering associated with convection filled the field of view. The polarization difference, however, continued to decrease as the rainfall increased. Based upon comparisons with ground-based radar data from different parts of the world, an equation for rainfall based on the polarization difference at 37 GHz was derived. Starting with the SMMR era, more physical algorithms started being developed (e.g., Olson, 1989) where the inversion techniques were based on the minimization of the difference between observed TBs and simulated TBs derived from radiative transfer computations.

The launch of the first Special Sensor Microwave/Imager (SSM/I) in 1987 (Hollinger, 1987) generated great interest in precipitation retrieval, thanks to the availability of 7 channels (19.35, 22.235, 37.0 and 85.5 GHz, all in horizontal and vertical polarization, except 22.235 GHz) and higher spatial resolution. Several studies were dedicated to demonstrate SSM/I potential for quantitative precipitation estimates (e.g., Mugnai et al., 1990; Smith et al., 1992, Wilheit et al.,

_____

1994). The various algorithms designed for SMMR were adapted to SSM/I, and new approaches were developed to exploit the higher frequency channels. With SSM/I the microwave remote sensing of precipitation entered a new era, mostly because of its long, and stable time series for over 20 years. Instead of reviewing all algorithms that were developed in this era, only a few select examples are presented here that represent the different types of algorithms that were developed.

Wilheit et al. (1991) developed a technique for rainfall rate retrieval based on the combination of TBs at 22 GHz and 19 GHz (vertical polarization channels) ($2Tb_{19V} - T_{22V}$). This channel combination showed a well defined peak corresponding to non-raining conditions, followed by a more or less linear portion (in log space) corresponding to precipitating pixels. The technique worked only over ocean, where the emission signal was evident, and it required data aggregated at monthly, $5° \times 5°$, scale to ensure robust relations between brightness temperatures and rainfall rate distributions. Versions of this algorithm formed the basis for the Global Precipitation Climatology Project (GPCP; Adler et al., 2003) for the entire lifecycle of the SSMI and future SSMIS instrument series, as well as early TRMM and AMSR-E products.

Scattering-based methods grew significantly in the SSM/I era due to the addition of the 85 GHz channels that exhibit much greater scattering signals than 37 GHz (SMMR). Ice scattering processes at 85 GHz in deep convection cause brightness temperatures to fall below 100 K and even below 50 K on rare occasions. To exploit this scattering signal, Spencer (1989) defined the Polarization Corrected Temperature (PCT) that remains broadly in use today. The relationship between rain rate and PCT was left for the community to adjust, and a series of algorithms quickly emerged (e.g. Ferraro et al., 1996; Kidd, 1998; Connor and Petty, 1998). While these algorithms all tend to use more than one channel to discriminate raining scenes or to provide additional information about the background state, the rainfall determination remained largely a function of the 85 GHz channel.

Another category of algorithms was the physically based retrieval approach, such as that used by Wentz and Spencer (1998). The algorithm simultaneously retrieves near-surface wind speed, column water vapour, column-integrated cloud water, and rain rate over water. It does so by relying on the fact that the brightness temperature is directly related to the transmittance of water in the atmosphere. The first step in the retrieval is thus to simultaneously retrieve this atmospheric transmittance, along with the water vapour, and surface properties - wind speed, and effective radiating temperature. This is possible as each of the individual parameters has a unique radiometric signature in the 19- through 37-GHz range. Once this is accomplished, the difference between the 19 and 37 GHz channels is used to determine the beam filling, or inhomogeneous rain effect. A correction is applied for the total attenuation due to liquid. The formulation then used is Mie theory and an assumed relationship between cloud- and rain-water to derive a column rain water and, together with an assumed rain column height based upon the SST, a surface rainfall rate.

The simultaneous inversion work that was started by Olson (1987) continued into the SSMI era, but the minimum variance solution was more or less replaced by Bayesian schemes. The overarching difficulty with the minimum variance schemes was ultimately the severely under-constrained nature of the retrieval (Stephens and Kummerow, 2015). There are simply far too many variables in a precipitating cloud related to the hydrometeor types and their vertical distribution, than can be uniquely retrieved with radiometers carrying a limited number of frequencies. More investigators adopted Bayesian schemes (e.g. Kummerow 1994; Evans et al., 1995; Marzano et al., 1999). The greatest challenge in Bayesian schemes was to find the correct distribution of observed rainfall rates. This relied mostly on various cloud resolving model (CRM) output to represent hydrometeor profiles that would be observed in nature, coupled with a radiative transfer model (RTM). CRM model-based approaches had to tackle the critical issue of being representative of actual observations and to ensure that Bayesian schemes accounted for uncertainties in both the modelled

_____

microphysical profiles and the radiative transfer modelling used to simulate multi-channel brightness temperatures (Panegrossi et al., 1998). However, since cloud resolving models of that era were regional and typically simulated only individual precipitating cloud systems, the Bayesian scheme needed to first screen non-raining pixels so that these would not be included in the statistics. Much of the early work was thus focused on producing realistic cloud model simulations and screening of non-raining pixels, particularly over complex coasts and topography. Uncertainties had to be estimated as they include many of the assumptions in the cloud resolving models and radiative transfer computations and remain an area of research 20 years after the first Bayesian schemes were introduced. These early radiative transfer computations formed the basis for most of today's "satellite simulators" in the microwave regime (e.g. Matsui et al., 2013) that simulate observable radiances from cloud resolving model output.

With the advent of the TRMM satellite, in 1997, a new era started. Algorithms originally developed for SSM/I were adapted to the TRMM Microwave Imager (TMI) and, successively, also to the SSMIS that succeeded the SSM/I in late 2005, and then to the Advanced Microwave Sounding Radiometers on EOS (AMSR-E). The focus turned more to physical algorithms such as Wilheit et al., (1991) that could produce uniform results across the entire constellation of passive microwave sensors.

Over-ocean rainfall retrieval algorithms such as the Remote Sensing Systems (RSS) also continued developing (Wentz and Spencer, 1998), later re-named the Unified Microwave Ocean Retrieval Algorithm (UMORA; Hilburn and Wentz, 2008). The algorithm uses the 19 and 37 GHz observations common to a wide variety of microwave sensors (AMSR, GMI, SSMI, SSMIS, TMI). The small differences in frequency and incidence angle present between these sensors are removed using the RSS radiative transfer model (Meissner and Wentz, 2012; Wentz and Meissner, 2016). As before, atmospheric transmittance is estimated from the difference between the vertically and horizontally polarized brightness temperatures (Tbs), while beam filling effects are corrected for by using the ratio of 19 and 37 GHz absorption that is used to infer the sub-pixel variance of absorption. Improvements (Hilburn and Wentz, 2008) also incorporated the effects of footprint size, in order to remove systematic biases among rain retrievals from the various sensors. The resulting estimate of absorption is directly related to the total amount of liquid water path (LWP) in the footprint, but is indirectly related to the surface rain rate (RR). To estimate the RR, the contribution of cloud water to the LWP is removed using a global relationship between rain and cloud water. Then the algorithm estimates RR from the rain water by assuming that the liquid is distributed uniformly between the surface and the freezing layer estimated from the sea surface temperature. It is worth mentioning that this is a key assumption underpinning all emission-based PWM algorithm, and remains one of the greatest unknowns in cloud physics.

JAXA's microwave algorithm developed for their GSMAP algorithm (Aonashi et al., 2009) made direct use of TRMM's precipitation radar data to deal with some of the non-uniqueness problems in passive microwave inversions. In their case, mean rainfall profiles were constructed from TRMM's precipitation radar observations and radiative transfer calculations were used to predict observed radiances not only for TRMM's TMI but for all other orbiting radiometers as well.

The Bayesian approaches that relied heavily on cloud resolving models to provide a priori information on cloud structures also began using the TRMM radar provided cloud hydrometeor profiles. The Goddard profiling algorithm, GPROF (Kummerow et al., 2015), in particular, was adapted for the TRMM and later the GPM imagers and constellation satellites. The a priori database needed to describe Pr(R) came directly from the radar retrievals. Because the TRMM radar observed raining and non-raining pixels in the correct proportions, the GPROF scheme no longer needed to screen pixels for rainfall before applying the Bayesian scheme. While the early versions of GPROF

developed for TRMM and AMSR-E (Kummerow et al., 2001) still used scattering algorithms over land, that aspect was eventually replaced by a fully parametric Bayesian scheme in the GPM era. The fully parametric approach can also be coupled, as was done by Casella et al., (2013; 2017a) to more fully exploit meteorological data to help minimize the non-uniqueness of solutions, particularly over land areas.

While the approaches discussed above were generally motivated by and developed for microwave imagers, there is a long history of microwave sounders. Operational sounders have typically operated in the 54-60 GHz oxygen complex, and the 183 GHz water vapour absorption line to retrieve temperature and water vapour profiles. They often also carried lower frequency channels to correct for surface radiation, and had window channels mostly at 89 GHz and 150 GHz.

An early algorithm is due to Spencer (1993) who used relative warming in the histograms of channels 1 and 2 (50.3 and 53.74 GHz) of the Microwave Sounding Unit (MSU) to infer the total cloud and rain water content of clouds at 2.5° grid scales – that approximate footprint size of those channels. The background temperature fluctuations from the air mass itself were corrected for by channel 3 (54.96 GHz) that is sensitive to the temperature itself. By using a series of seven satellites, he was able to produce a climatology of oceanic precipitation from 1978 – 1991.

With the advent of the Advance Microwave Sounding Unit (AMSU), much higher spatial resolutions were available than with its predecessor. This made scattering approaches feasible. Ferraro et al., (2000) used NOAA-15's AMSU instrument to detect the scattering signal from precipitation-sized particles at the 89 and 150 GHz channels. This algorithm used the scattering indices that have been described earlier but separated convective from stratiform rainfall in order to account for the difference in the vertical hydrometeor structures of these two types of system. Scattering indices were converted to surface precipitation by matching the index to ground-based observations over the United States.

Other approaches were developed to exploit also the opaque channels around 183.31 GHz, originally designed to retrieve water vapour profiles, but showing great potential for precipitating cloud characterization (Hong et al., 2005) and for precipitation retrieval (Laviola and Levizzani, 2011). Both emission and scattering algorithms were refined over time but the more physical approaches being developed for the microwave imagers were slow to develop because the information content pertaining to precipitation was more limited in sounders – particularly over oceans where imagers had good information from the emission channels. Among these, approaches based on artificial neural networks, successfully applied only to microwave sounders (Surussavadee and Staelin, 2008, Sanò et al., 2015, 2016), have been recently applied to imagers (e.g., GMI, as in Sanò et al., 2018).

A unique algorithm that was developed for sounders is the MIRS algorithm (Boukabara et al., 2011). MIRS is a 1-D Optimal Estimation (OE) solution that inverts the radiative transfer equation by finding radiometrically appropriate profiles of temperature, moisture, liquid cloud, and hydrometeors, as well as the surface emissivity spectrum and skin temperature. As for earlier minimum variance solutions, the OE approach minimizes the difference between observed and simulated brightness temperatures but includes an a priori term that prevents the solution from deviating too far from expected values. While OE procedures, particularly if clouds and precipitation are included, usually suffer from insufficient constraints on the solution as described earlier, MIRS's approach to tackle this problem is to constrain the inversion problem by using eigenvalue decomposition and employing a limited number of eigenvectors that are consistent with the information content present in the observations. It also has the option to use a forecast model to provide good a priori information, instead of the default climatology background. Because of the variable-reduction approach, MIRS is highly flexible, and it could be used as a retrieval tool,

independent of numerical weather prediction. The MIRS system was implemented operationally at the U.S. National Oceanic and Atmospheric Administration (NOAA) in 2007 for the NOAA-18 satellite. Since then, it has been extended to the microwave sensors aboard Metop-A and B (AMSU/MHS), DMSP (SSMIS), SNPP and JPSS (ATMS), as well as to research missions such as Megha-Tropiques (SAPHIR).

Although most passive microwave sensors are equipped with high frequency channels (90-190 GHz) that are highly sensitive to the scattering of ice hydrometeors, detecting and quantifying surface snowfall rates using spaceborne microwave radiometers remains a challenging task (Levizzani et al. 2011, Skofronick-Jackson et al. 2017). The low and variable emissivity of snow or ice-covered surfaces (e.g., Prigent et al., 2006) can mask snowflake scattering signatures (Ebtehaj and Kummerow 2017). In addition, the snow microphysics is very complex and snow precipitating systems are often composed of a wealth of snow particles with a variety of densities, shapes, particle size distributions and radiative properties (e.g., Kuo et al., 2016). Moreover, supercooled droplets and melting snow also frequently occur and can strongly affect the observed signal (Kneifel et al. 2010; Liu and Seo 2013, Panegrossi et al., 2017). Several model-driven (Skofronick-Jackson and Johnson, 2011; Kulie et al., 2010; Eriksson et al., 2015) and empirically driven approaches based on DPR or CPR snowfall observations (Liu and Seo, 2013; You et al., 2017; Panegrossi et al., 2017; Takbiri et al., 2019), have provided instructive insights on microwave multi-frequency signals associated with snowfall in cold regions. Based on these studies snowfall retrieval algorithm have been developed, both for imagers (such as You et al., 2015 for SSMIS), and sounders (e.g., Kongoli et al. 2003; 2018; Ferrato et al., 2005). These algorithms largely rely on the use of a database or a look-up table that relates brightness temperatures of snowing clouds to the spaceborne (or ground-based) radar snowfall observations, along with ancillary model-derived variables, such as atmospheric temperature and moisture profiles. More recently, Rysman et al. (2018) developed a new snowfall retrieval algorithm for GMI (SLALOM), suitable also for higher latitudes, based on observational datasets built from the CloudSat Cloud Profiling Radar (CPR) snowfall products, and model-based environmental conditions, while all GMI channels are exploited for background surface characterization and snowfall retrieval.

Conclusion: Following the TRMM heritage, GPM has employed Bayesian algorithms for precipitation retrieval from all constellation radiometers. But, unlike TRMM-era radiometer retrievals, which use a model-generated a priori hydrometeor database, GPM radiometer retrievals use an observation-constrained global database consistent with GPM Core sensor measurements. Since the common hydrometeor database used for constellation radiometer retrievals contains DPR information, GPM radiometer retrievals may be characterized as "radar-enhanced".

_____

3. SINGLE-FREQUENCY RADAR ALGORITHMS

Many radar algorithms assume that the particles in the target volume are much smaller than the wavelength of the incident radiation and use the Rayleigh approximation for the backscatter cross-section (L'Ecuyer and Stephens, 2002). At the frequencies used in most spaceborne applications, the Rayleigh approximation breaks down in rain, and the scattering properties are more accurately described using Mie theory (Mie, 1908). For the Rayleigh approximation, the radar reflectivity is obtained from a simple relationship between it and the particle size distribution (e.g. Lhermitte, 1990; Matrosov et al., 2005). In the Mie regime, this relationship between the reflectivity and the particle size distribution is less straightforward due to the more complicated nature of the backscattering cross-section. Importantly, the measured radar reflectivity is also affected by attenuation of the signal that can occur at higher radar frequencies.

The profiling capabilities of spaceborne radars were confirmed by the Tropical Rainfall Measuring Mission (TRMM), which carried the first radar operating from space that was specifically designed for precipitation measurements. One of the first algorithms developed for this 14-GHz (Ku-band) precipitation radar (PR) used the TRMM PR rainfall profile algorithm, which selected a drop size distribution based on the rain type and the presence or absence of a bright band and corrected the drop size distribution based on an estimate of the path-integrated attenuation (Iguchi et al. 2000). This algorithm operated iteratively by assuming a power-law relationship between the reflectivity and the extinction coefficient. The importance of developing algorithms better suited to combining information from a variety of different sources led to the development of a first-generation combined PR–TRMM Microwave Imager (TMI) rainfall algorithm. This employed a Bayesian approach to retrieve parameters relating to the drop size distribution from PR reflectivities with an estimate of the path-integrated attenuation derived from the 10.6-GHz channel of the TMI (Haddad et al. 1997).

The successful deployment of TRMM was of course followed by the placement into orbit of CloudSat, with its 94-GHz (W-band) Cloud Profiling Radar (CPR). Detailed and extensive descriptions of CloudSat retrieval algorithms applied to rain have been provided by, for example, Austin and Stephens (2001), L'Ecuyer and Stephens (2002) and Leinonen et al. (2016). L'Ecuyer and Stephens (2002) state that many radar algorithms assume a particle size distribution (PSD) and Rayleigh scattering to obtain relations, usually in the form of a power law, between the rain rate and the radar reflectivity and between the rain rate and the extinction coefficient. These are directly invertible, allowing the rain rate to be derived from the radar reflectivity measurements. These methods allow the problem to be presented in a simple analytical form, which results in a computationally quick and relatively simple retrieval algorithm. These assumptions also lead to two potential sources of uncertainty: (1) the assumption of a PSD strongly influences the values used to specify the power-law relationship, and (2) the Rayleigh assumption is not valid for radars with frequencies in excess of 10 GHz, a characteristic of both the TRMM PR and CloudSat CPR.

The increased complexity of implementing retrieval algorithms at frequencies above 10 GHz motivated the adoption of alternative techniques in order to undertake retrievals using single-frequency observations at these frequencies. One particularly effective method is that of optimal estimation based upon a Bayesian formalism (Rodgers, 1976; 1990; 2000; Marks and Rodgers; 1993) and applications of this (Engelen and Stephens, 1999; Miller et al., 2000). This approach allows a degree of generality to be maintained when constructing an appropriate algorithm, which permits varying the assumed particle size and shape and facilitates the incorporation of complementary information from additional sensors if deemed necessary.

The general optimal estimation method has been described in detail for retrievals from attenuating radars by, for example, L'Ecuyer and Stephens (2002). An appropriate forward model to be used in

_____

the retrieval can be selected from criteria such as rain type, freezing level, or the presence of a bright band, and uncertainties in the vector of parameters must be explicitly accounted for in the inversion approach. As a general comment when considering the probability distributions of the parameters being retrieved, Jaynes (2001) argues that the Gaussian distribution is the ''most honest'' representation of errors if only the mean and variance of a probability distribution are known. Alternative distributions, unless rigorously justifiable, add spurious information to the retrieval, therefore biasing the results. For this reason, uncorrelated and unbiased Gaussian statistics are often adopted to ensure that only distribution mean and variance information are introduced in the retrieval. The retrieval process may be summarized as follows:

- Infer an initial rain rate and extinction coefficient for the uppermost rain layer using the appropriate Z–R and k–R relations.
- Correct the measured reflectivity in the next layer for the attenuation due to the one above it and determine an initial rain rate and extinction coefficient for that layer.
- Repeat for all layers, correcting the measured reflectivity of each layer for the attenuation due to all layers above it.
- Using this initial profile of rain rate, simulate reflectivities using the radar forward model.
- Compute a new rain-rate profile.
- Iterate until such time as the covariance-weighted square difference between successive estimates is much less than the total number of independent variables being retrieved.

Because of the severity of attenuation by rainfall at high radar frequencies (also in the Ka-band), it is not sufficient to rely exclusively on a profile of radar reflectivity to make estimates of rainfall profiles. Fortunately, many spaceborne platforms such as TRMM offer additional sources of information from other instruments. Microwave radiometers can be used to obtain an estimate of the total precipitation water path (PWP), which is defined as the column-integrated liquid water that is in the form of precipitation. This estimate complements the radar reflectivity measurements in that it imposes a constraint on the total attenuation through the rain column. An accurate estimate of PWP forces the algorithm to operate with the correct atmospheric water mass while the radar reflectivities determine how this mass is distributed vertically. This emphasizes the complementarity of active and passive microwave data in rainfall retrievals. It is also apparent that the optimal constraint accuracy increases with increasing rain rate and with decreasing altitude: the greater the attenuation, the more accurate the PWP estimate must be to correct for it. Depending on the specific goals for the application of the algorithm, an estimate of PWP with only moderate accuracy might be all that is required to constrain the retrieval. In applications involving the use of a high-frequency radar to supplement rainfall information obtained at lower frequency, for example, retrievals in rainfall lighter than 4 or 5 mm h^{-1} may be of primary importance, in which case a PWP estimate accurate to 20% is sufficient.

The path-integrated attenuation (PIA) approach to correct for attenuation, which makes use of the surface-return echo to estimate the total attenuation through the rain column, is stable and yields much more accurate results when attenuation is severe (Iguchi and Meneghini 1994). This is confirmed by the remarkable improvement in the retrieval when a precipitation water path constraint is imposed on the retrieval. Since the PIA derives from the precipitation water path, both constraints perform essentially the same function. Either method (or both) can be used with very little modification. It is important to note that the above discussion covering application of this algorithm to the CloudSat radar is explicitly for the purpose of retrieving very light rain that may not be detectable at lower frequencies.

3.1 Retrieval algorithms for rain

It is important to note that all retrieval algorithms depend critically upon the assumptions that go into them. Furthermore, transforming remote-sensing observations into actual rainfall rate products is based on a priori assumptions on the typology of precipitation (ongoing microphysical processes, stratiform vs convective) and introduces unavoidable uncertainties. That is, it is often the case that particular Z_e-R relations, to highlight one example, are selected to characterize specific precipitation regimes. This will necessarily tend to exclude a wider class of precipitation types that could also be considered. For example, for the TRMM PR rainfall estimates were affected by the choices made for the Z_e-k and Z_e-R relations. However, part of this difficulty was alleviated by taking advantage of the peculiarity of the spaceborne radar, i.e., the surface echo. The use of the surface reference method enabled the possible range of the raindrop size distribution to be narrowed. However, it was acknowledged that the non-uniform rain distribution within the radar resolution cell could represent a large source of error when the attenuation was severe (Iguchi et al., 2000), and a first-order correction for this effect was provided by the algorithm.

An example of TRMM rainfall data has been provided by Shukla et al. (2019), who evaluated TRMM rainfall estimates from the Upper Ganga Basin (Himalayan catchment) by comparing them with gauge-based India Meteorological Department (IMD) gridded precipitation records. They found that the spatial distribution of rainfall during post-monsoon and winter season is captured adequately, but the limited efficiency of TRMM is reflected for the pre-monsoon and monsoon seasons. A bias correction has satisfactorily enhanced the spatial distribution of rainfall obtained from TRMM for almost all the seasons except for data collected during the monsoon season. A seasonal evaluation of bias-corrected TRMM precipitation against IMD is represented in the form of scatter plots in Figure 2, which corresponds to Figure 6 in Shukla et al. (2019). Overall, a significant improvement in monthly precipitation has been observed post bias correction in all the seasons. The correlation between the two precipitation datasets for the post-monsoon and winter season has improved from 0.57 and 0.55 to 0.65 and 0.64, respectively. The R^2 value for the pre-monsoon season also improved from 0.24 to 0.32 post bias correction, but remained lower than for the other seasons. Overall, bias correction has significantly improved the TRMM rainfall estimates especially for pre-monsoon, post-monsoon and winter and the corrected rainfall can be used as a climate input for various hydrological studies.
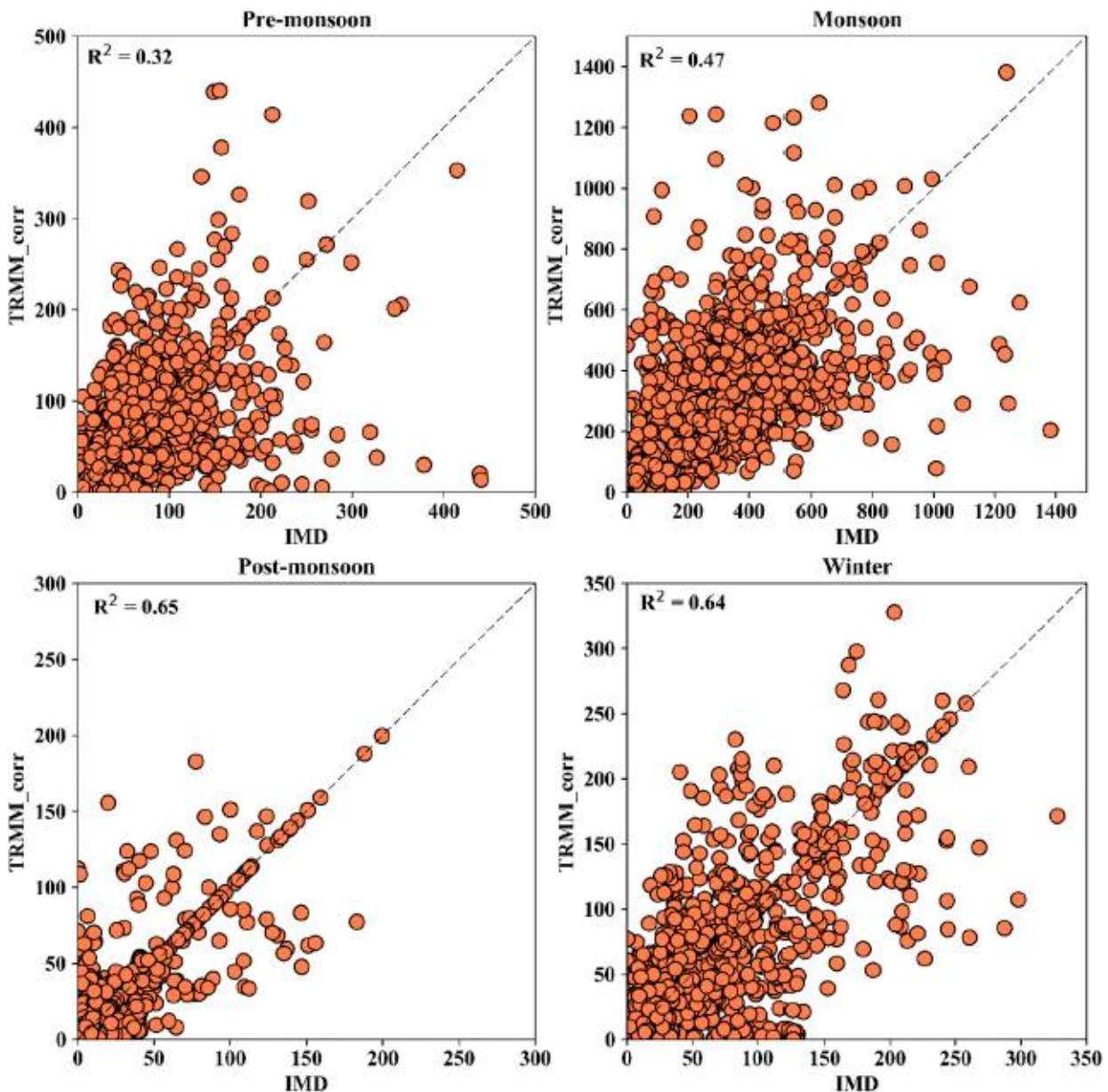
Figure 2: Scatter plot of IMD precipitation against bias corrected TRMM precipitation representing correlation for four seasons (pre-monsoon, monsoon, post-monsoon and winter) in the Upper Ganga basin. (Reproduced from Shukla et al., 2019)

After the successful use of TRMM to obtain rainfall estimates, this approach was also adapted to the CloudSat CPR. The objective of the CloudSat 2C-RAIN-PROFILE rainfall product (Lebsock, 2018) is to infer profiles of precipitation liquid and ice water content along with an associated surface rain rate from the CPR reflectivity profiles and a constraint on the path-integrated attenuation (PIA) of the radar beam. Key inputs to the algorithm flow from the 2C-PRECIP COLUMN product, which flags profiles for precipitation, determines the freezing level, determines the precipitation type (convective/stratiform/shallow), and provides an estimate of the magnitude and uncertainty of the PIA. The algorithm further makes use of ancillary temperature and humidity estimates from the ECMWF analysis provided in the ECMWF-AUX product. Because the CPR operates at the strongly attenuated frequency of 94 GHz, the attenuation constraint given by the PIA

is central to the retrieval to avoid the propagation of errors discussed by Hitschfeld and Bordan (1954). The problem of estimating the rain rate from the observations is underconstrained and requires a number of simplifying assumptions. These assumptions take the form of simple physical models that are imposed upon the problem to make the necessary radiative calculations possible. These models include (1) a model to distribute cloud water in the vertical and determine the cloud DSD, (2) a model of evaporation of rain below cloud base, (3) a model of the precipitation DSD, and (4) a description of the thermodynamic phase of the hydrometeors in each radar bin. Cloud water must be modelled not because of its influence on the reflectivities themselves but rather due to its influence on the PIA. As a result, the location of the cloud water within the vertical profile is of secondary importance. It is assumed within the algorithm that the cloud water content is uniform with height below the freezing level and the cloud water path (CWP) is given by a parameterization based on the work by Lebsock and L'Ecuyer (2011). The CWP is then distributed evenly between the cloud base and the top of the liquid layer. A model of evaporation of rain water from cloud base to the surface is taken from Comstock et al. (2004).

In the original iteration of the 2C-RAIN-PROFILE product three distinct rain drop size distributions were used to describe deep precipitation, shallow convection, and shallow stratiform. In the most recent version of the code, the algorithm's maintainers implemented a single moment parameterization of the DSD as a function of the rain liquid water content taken from Abel and Boutle (2012). This was originally developed to improve model simulations of rainfall intensity but has much broader applicability. The parameterization assumes an exponential size distribution that, using model parameters from Abel and Boutle (2012), provides the best fit to a diversity of rain types from heavy deep convective rain to stratocumulus drizzle. Using this parameterization allows the retrieval to avoid sudden transitions in the assumed DSD, and therefore the retrieval parameters, which was sometimes observed in an older version of the algorithm. The vertical structure of thermodynamic phase is based on the stratiform/convective flag input from the 2C-PRECIP-COLUMN data product. This provides an output value for precipitation type (convective/stratiform/shallow) along with the freezing level (based on ECMWF analysis) and the rain top height. Cloud liquid water is distributed uniformly throughout the liquid portion of the profile. An estimate of precipitation incidence is provided in the 2C-PRECIP-COLUMN product.

It should be noted that there are certain additional aspects to consider when determining the effectiveness of the algorithm. For example, profiles over land surfaces are currently treated as missing pixels by the algorithm due to the inherent difficulty in estimating the PIA over land. Future versions of the algorithm may attempt to address these profiles. In the heaviest precipitation, the surface return may be completely saturated making an estimate of the surface cross-section impossible. In this situation only an estimate of the lower bound on the PIA may be made. In this case the 2C-RAIN-PROFILE algorithm is not run, and a negative rain rate is passed through from the 2C-PRECIP-COLUMN product. The absolute value of this rain rate may be interpreted as a minimum possible rain rate. Care should be taken when working with a dataset in which the fraction of pixels that meets this criterion exceeds 0.5% because this condition is set in the heaviest rainfall events that contribute the most to accumulations. Output profiles are only reported for the lowest cloud layer beginning at the first instance of that layer exceeding -15 dBZ. The product does not therefore provide a complete description of the entire profile of liquid and ice hydrometeors. Furthermore, there is a systematic data loss for heavy precipitation cases. Profiles are also not available when the algorithm does not converge to a valid solution.
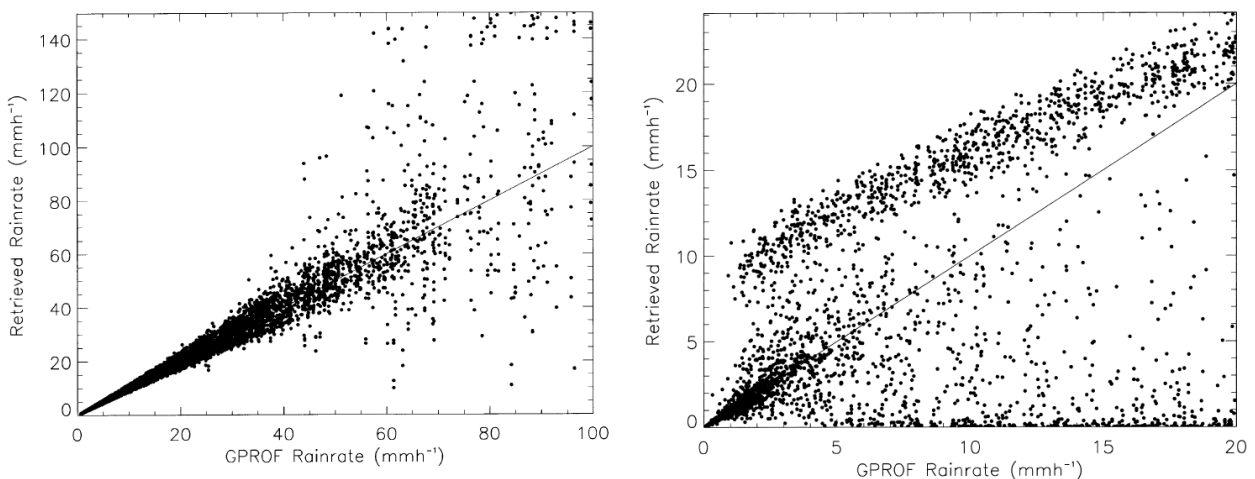
Figure 3: The left-hand panel shows retrieved rain rates at 14 GHz, with input from a database used for testing GPROF. The right-hand panel shows the same but at 94 GHz. There is a clear discrepancy at 94 GHz for rain rates greater than about 1.5 mm hr^{-1} (Reproduced from L'Ecuyer and Stephens, 2002).

L'Ecuyer and Stephens (2002) used synthetic retrievals in order to demonstrate the utility of the technique. The algorithm was tested using a cloud database (consisting of approximately 10 000 cloud and rainfall profiles) used in the Goddard Profiling Algorithm (GPROF; Kummerow et al., 2001; 2015), which has been employed in rainfall retrievals from the TRMM Microwave Imager (Kummerow and Giglio, 1994; Olson et al., 1996). A scatterplot of retrieved surface rain rate against the GPROF input at 14 GHz is presented in the left-hand panel of Figure 3, corresponding to Figure 2 of L'Ecuyer and Stephens (2002). The results show excellent agreement for surface rain rates below 40 mm h^{-1}. Significant attenuation by large raindrops at higher rain rates, however, degrades the quality of the retrievals. The right-hand panel of Figure 3, corresponding to Figure 3 of L'Ecuyer and Stephens (2002), shows similar results obtained from a retrieval using reflectivities at 94 GHz. Attenuation is severe for all rainfall at 94 GHz and only rain rates less than 1.5 mm h^{-1} are retrieved accurately in the absence of additional information.

Another description of retrieving parameters associated with light precipitation has been provided by Mitrescu et al. (2010), and the profiling and retrieval algorithm used comprises a number of components. These include a cloud microphysical model, a 94-GHz reflectivity model, a model for multiple-scattering effects, consideration of surface effects and a melting layer model. The CPR on board CloudSat measures backscatter reflectivity as a function of distance from both distributed (i.e., hydrometeors) and solid (i.e., surface) targets. The profiling algorithm relies on the physical relationship between the returned power, measured as a function of distance to the target, and the cloud, precipitation, and surface properties. Because electromagnetic radiation at 94 GHz, the operating frequency of the CloudSat CPR, is affected by absorption resulting from atmospheric water vapour, the measured signal is subject to both cloud and atmospheric attenuation, and this must be taken into account. Because of the large volume sampled by the CPR, the returned power at a given range is often increased because of multiply scattered photons. A component of this multiply scattered energy leads to a loss of correct ranging capability, since the signal may have come from other regions of the cloud. These effects increase with the penetration depth and with the size of cloud particles. Therefore, the ability to accurately simulate CPR observations (and thereby retrieve physical parameters) becomes increasingly more challenging for range gates closer to the ground (i.e., farther away from radar), which is where the precipitation occurs.

Since clouds are composed of a distribution of particles (ice and/or water), of particular interest are physical parameters relating to these, such as number concentration, geometrical dimension, mass, fall velocities, and rain rates. Moreover, even if clouds at some point in their evolution are in fact composed of a bimodal distribution of cloud particles and precipitating particles, the radar is mostly sensitive to the latter. Therefore, it is often the case that clouds are represented through a single particle distribution that is chosen to best describe precipitating particles. Obviously this approach would be valid only in precipitating clouds. A common assumption is that all clouds can be described in terms of a Marshall–Palmer droplet size distribution. The retrieval (or inversion) method chosen by Mitrescu et al. (2010) for inferring profiles of precipitation rate is the optimal estimation technique. Described in detail in many papers (e.g., Jazwinsky 1970; L'Ecuyer and Stephens 2002; Rodgers 1976), it uses the forward model to minimize the cost function.

Mitrescu et al. (2010) validated their results by applying their retrieval algorithm to an orbital segment that was collected when CloudSat was over the KLIX Next Generation Weather Radar (NEXRAD), near New Orleans, Louisiana, on 31 July 2006. Figure 4 corresponds to Figure 2 in Mitrescu et al. (2010) and the uppermost panel of Figure 4 shows the radar profile as recorded by the CPR. Evident in the radar return is a nimbostratus cloud structure with echo tops around 12 km and with its base obscured by the rain signal. The bright band (BB), which can be clearly distinguished, is just below the freezing level as indicated by the temperature profile. Strong echoes near the surface suggest that precipitation was likely. The second panel of Figure 4 demonstrates the profiling capabilities of CloudSat and both the performances and limitations of the Mitrescu et al. (2010) retrieval algorithm as it shows profiles of the retrieved LWC and ice water content (IWC) only for cases where the precipitation flag is set. The third panel of Figure 4 shows the unattenuated 94-GHz reflectivity. This is nothing more than the application of the forward model to the retrieved LWC and IWC profiles. The bottom panel of Figure 4 shows the rain rates inferred using CloudSat data applied to three different algorithms and one using KLIX radar data (extracted along CloudSat track). The latter is converted into rainfall rates using the default (Z–R) relationship for the WSR-88D radar network and shown with the green line. The black line denotes results using the algorithm developed by Mitrescu et al. (2010). As an additional comparison, the blue line represents the approach described by Matrosov (2007), where an extinction versus rain-rate (k–R) relationship is being employed. The red line shows the rain rates equivalent to a uniform cloud layer as described by Haynes et al. (2009), where only PIA information is used to infer a rain rate. Finally, the along-CloudSat track rain rates as retrieved using the AMSR-E passive microwave sensor on board Aqua are presented with an orange line. For this particular case, the agreement between all these various retrieval schemes (and/or sensors) is satisfactory.

Conclusion: CloudSat products that return rainfall estimates will function well during conditions where the levels of precipitation are not too high. Conversely, heavy rain will result in significant attenuation that will produce appreciable effects in the derived rain rates. CloudSat returns reliable estimates of rain rates when these lie between about 0.1 and 5.0 mm h^{-1}.
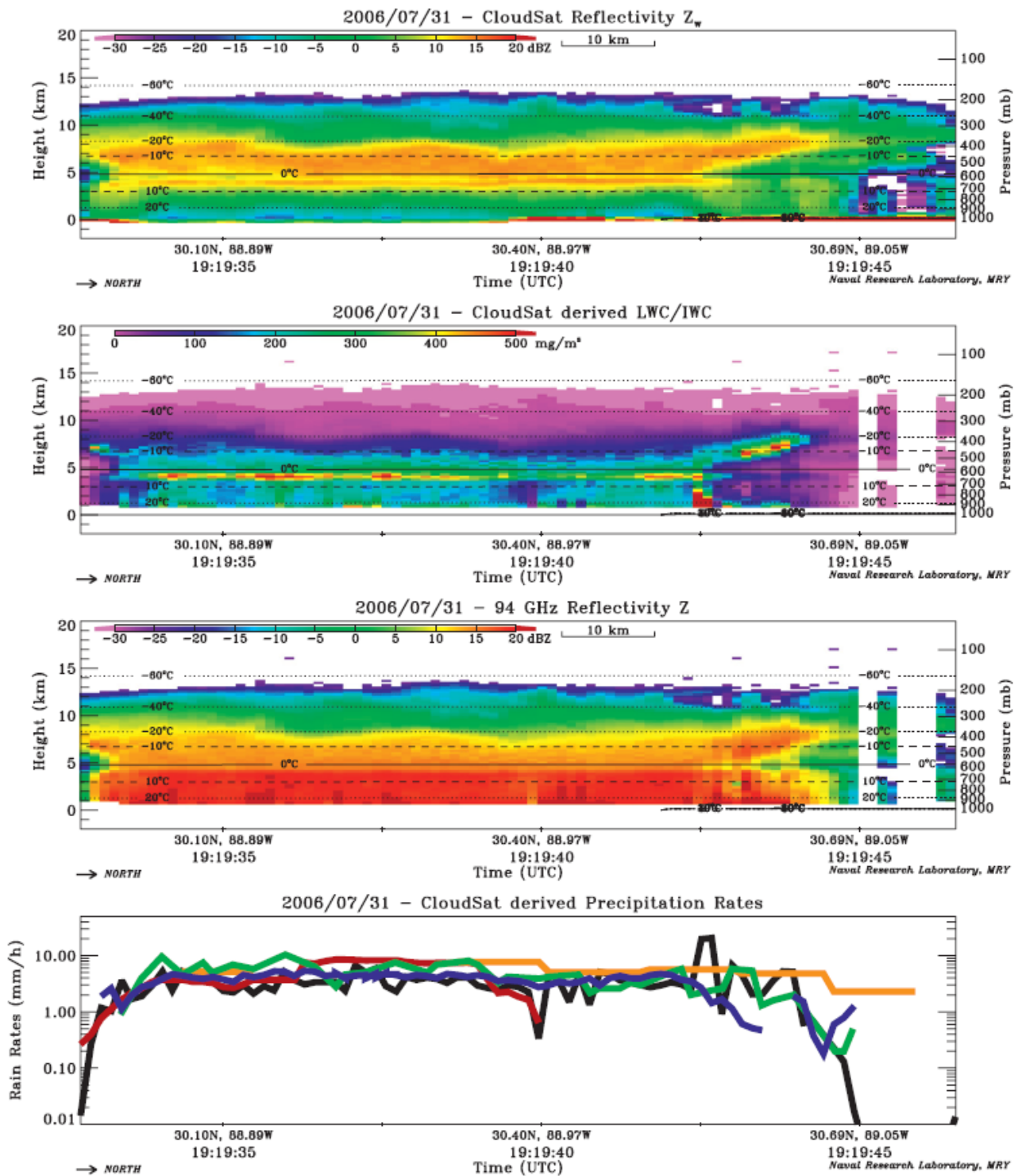
Figure 4: Case study of 31 Jul 2006 near KLIX NEXRAD radar. (top) CloudSat reflectivity, (second from top) retrieved profiles of LWC and IWC, (third from top) simulated 94-GHz reflectivities using retrieved LWC and IWC profiles, and (bottom) rainfall rates using (i) Mitrescu et al. (2010) method (black line), (ii) k–R method (Matrosov, 2007; blue line), (iii) PIA-based method (Haynes et al., 2009; red line), (iv) KLIX Z–R relationship (green line), and (v) AMSR-E-derived precipitation rates (orange line). (Reproduced from Mitrescu et al., 2010).

3.2 Retrieval algorithms for snow

As well as estimates of the rain rate, the CloudSat CPR can also calculate levels of snowfall. The CloudSat Snow Profile product (2C-SNOW-PROFILE) provides estimates of vertical profiles of snowfall rate along with snow size distribution parameters and snow water content for radar reflectivity profiles observed by the CloudSat CPR which, based on an evaluation of the profile and ancillary data, appear to coincide with snow at the surface (Wood et al., 2013). For these profiles, the product also estimates snowfall rate at the surface. Because of ground clutter, the CPR cannot reliably measure reflectivities near the surface. To overcome this limitation, the product algorithm estimates snow properties using a truncated reflectivity profile, terminated somewhat above the surface, then uses the estimated snow properties in the bottom-most portion of the profile to estimate the surface snowfall rate. For the truncated reflectivity profile, profiles of size distribution parameters are retrieved using an optimal estimation algorithm which incorporates a priori information about snow microphysical properties, radar scattering properties, and size distribution parameters. Retrievals are performed only for profiles which appear likely to contain snow at the surface, either dry snow or snow with a small melted mass fraction. The retrieved size distribution parameter profiles and the a priori information are then used to calculate profiles of snowfall rates and snow water contents. The optimal estimation method produces uncertainty estimates for the retrieved size distribution parameters, and these uncertainties are then used to estimate uncertainties for the snowfall rates and snow water contents.

Snowfall rate depends on the abundance of snow particles of different sizes (the particle size distribution or PSD), the masses of those particles, and their fall speeds. Fall speeds in turn depend on particle masses, their shapes, and environmental conditions. As is true for lower-frequency precipitation radars, radar backscattering at the 94 GHz frequency used by the CPR is sensitive to PSD and particle masses; however, at this higher frequency, backscattering is also sensitive to particle shape. With even simple models for the PSD, the particle masses and the shapes, observations of 94 GHz radar reflectivity alone are insufficient to constrain the models sufficiently to determine snowfall rates. To address this insufficiency, optimal estimation is used as the retrieval method for 2C-SNOW-PROFILE. This method enables the use of explicit a priori information which can help constrain the retrievals. Additionally, optimal estimation allows uncertainties in the retrieval assumptions and observations to be propagated into estimates of uncertainties in retrieval products such as snowfall rate (Wood et al., 2014). Wood et al. (2013) note that there is the potential for ground-clutter effects to produce anomalously high levels of snowfall close to the ground.

Several studies have shown the utility of CloudSat in obtaining snowfall estimates, e.g. Heymsfield et al. (2018) who covered alternative methods for deriving snowfall rate, Palerme et al. (2014) who discussed the amount of snow falling on the Antarctic ice sheet, and Matrosov (2019) who compared results with ground-based radars. CloudSat has also been used to evaluate other snowfall algorithms, e.g. SLALOM for the GMI (Rysman et al., 2018). CloudSat remote-sensing observations were also compared with two in situ micro-rain radars (MRR) at the coastal French Dumont d'Urville and mountainous Belgian Princess Elisabeth stations in East Antarctica (Lemonnier et al., 2019). This assessment of the CloudSat uncertainties provided confidence in the retrieval given the different climatic and geographical conditions of the two stations. It also justifies further analysis of this dataset in this region of the globe, where snowfall is critical and poorly known. Figure 5 shows results from the study by Lemonnier et al. (2019) and corresponds to Figure 3 presented by them. Focusing on the Dumont d'Urville station, Figure 5a shows a good agreement between CloudSat and the MRR's snowfall rates for each vertical level. Indeed, an averaged satellite precipitation rate at all levels is included within the 95% MRR confidence interval. The MRR profile presents a

maximum of the snowfall rate of 0.75 mm h^{-1} at 750 m and an inversion of the precipitation rate likely due to low-level sublimation processes, whereas the ground clutter prevents CloudSat from seeing the inversion. According to Durán-Alarcón et al. (2019), this precipitation event is representative of the climatology of the DDU station as it lies between the 20th and 80th quantiles (indicated by grey dashed line) with a shape similar to the average climatology in solid black line. According to Figure 5b, there is a poor concordance between the two datasets for low snowfall rate values. The MRR recorded low-level strong values until a null signal of precipitation from 1000 m upward, where CloudSat still recorded small but significant rates. An inversion of the precipitation rate at low levels is also observed under the maximum precipitation rate of 1 mm h^{-1} at 600 m. The strong gradient of this inversion is likely due to katabatic wind effects, which can drastically dry out atmospheric layers when blowing down from the ice cap. This event shows that the use of CloudSat for surface precipitation determination may be problematic in certain conditions for a specific event. It is also important to note that this event is an anomalous climatological event at the DDU station, in comparison with the quantiles of the vertical structure of precipitation both in terms of snowfall rate and shape.

Figure 5c shows a good agreement between the four lowest values of CloudSat observations and the MRR profile. Indeed, every averaged satellite measurement is included in the 40%-confidence interval, but the standard deviations indicate a large dispersion. Above this altitude the precipitation rate is small and the agreement is weaker. This is similar to what is observed in Figure 5b. CloudSat observes again a small signal of precipitation where MRR recorded a null snowfall rate, suggesting some limitations in the sensitivity or attenuation of the MRRs but also a satellite sensitivity for low snowfall rates. This event is an important anomalous climatological event at the PE station because the observed snowfall rates are much higher than the snowfall rates of the Durán-Alarcón et al. (2019) climatology. This is caused by the passage of an atmospheric river over the station. Figure 5d snowfall rates observed by both CloudSat and MRRs are quite low compared to the three other cases but the agreement remains good for the five lower satellite levels. According to Durán-Alarcón et al. (2019), this precipitation event is representative of the climatology of the PE station with in particular the presence of virga with very low precipitation rates included between the high and low quantiles.

Conclusion: CloudSat provides snowfall estimates with no identification of possible error for snowfall rates up to 5.0 mm h^{-1}. If the near-surface snowfall rate exceeds this value, then an indication of possible error in the retrieval is output in the retrieval status. There is also potential for ground clutter to give anomalously high values for snowfall close to the ground.
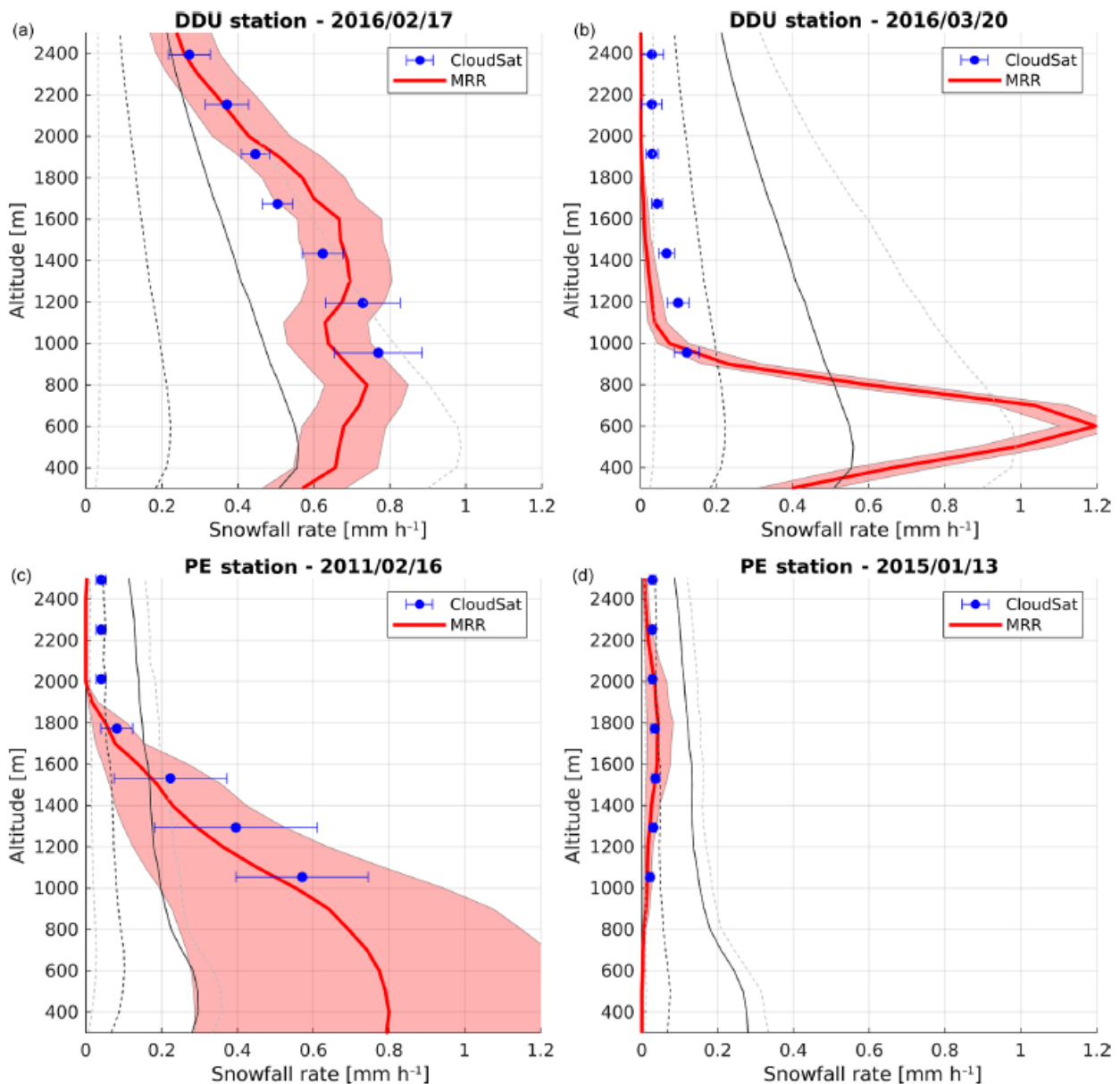
Figure 5: (a) Comparison between CloudSat (blue dots with 2-standard-deviation bars) and MRR (red solid line with shaded area representing a 95% confidence interval) for the 17 February 2016 precipitation event at the DDU station. (b) Same as panel (a) for the 20 March 2016 event at the DDU station. (c) Comparison between CloudSat (blue dots with 2standard deviation bars) and MRR (red solid line with shaded area representing a 40% confidence interval) for the 15 February 2011 precipitation event at the PE station. (d) Same as panel (c) for the 13 January 2015 event at the PE station. The mean precipitation profile obtained over a long period of observation is also shown and separated into quantiles. The grey dashed lines represent the 20th and 80th quantiles, the dark dashed line represents the 50th quantile and the solid line represents the average of the vertical structure of precipitation. (Reproduced from Lemonnier et al., 2019)

3.3 Retrieval algorithms for ice

This discussion on single-frequency algorithms will conclude with CloudSat algorithms relating to ice. An example of an algorithm pertaining to ice is given by Austin et al. (2009), who describe a retrieval procedure used to extract ice cloud microphysical parameters using CloudSat CPR data and temperature measurements. This technique is based upon that developed by Benedetti et al. (2003), but proceeds without an independent measure of the visible optical depth being required. It follows the standard approach of applying an optimal estimation algorithm in order to extract parameters associated with the particle size distribution.

The earliest versions of the retrieval algorithm, which occasionally failed to converge, represented the ice particles as spheres of fixed density whose size was modelled using a three-parameter modified gamma distribution. The retrieval would solve for the characteristic diameter, and the particle number concentration and particle distribution width were assigned fixed values and uncertainties based on climatology, field data or other considerations. These forward model parameters were constrained to be invariant with height. Values of typical microphysical parameters such as effective radius and ice water content (IWC) were easily calculated in terms of the size distribution parameters. A key improvement was made by incorporating dependence of the particle size distribution parameters on the height and the temperature. The augmented forward model utilized a log-normal distribution of ice crystals that is completely characterized by three parameters: the ice particle number concentration, the geometric mean diameter and the width of the distribution. Assuming thin ice clouds allows the particles to be described as Rayleigh scatterers. To compensate for the case where the reflectivity is overestimated due to the presence of non-Rayleigh scatterers, a correction based on Mie scattering properties was applied. The actual retrieval uses the optimal estimation approach described by Rodgers (1976; 1990), Marks and Rodgers (1993), and Rodgers (2000), where a vector of measured quantities is related to a state vector of unknowns by the specified forward model.

A validation of algorithms for ice has been provided by Austin et al. (2009). In order to have a common basis for comparison, the then current and previous retrievals described in Austin et al. (2009) were run on the same data sets used by Heymsfield et al. (2008). Plots of the ratio of retrieved to measured IWC ($r = IWC_{retr}/IWC_{meas}$) are shown in Figure 6, corresponding to Figure 5 of Austin et al., (2009), where the then previous algorithm is denoted ''R03'' and the then current algorithm is labelled ''R04.'' The plots show individual retrievals as small dots, with mean and standard deviation values for a given parameter range plotted as a large black dot and horizontal line, respectively. Figure 5 shows that the then current algorithm (R04) generally performed better than the then previous algorithm (R03), but there are situations where the opposite is true. The R04 algorithm is seen to have less low bias at low Z_e values (ignoring Z_e below the 30 dBZ minimum detectable signal of CloudSat) at a cost of more low bias at high Z values.
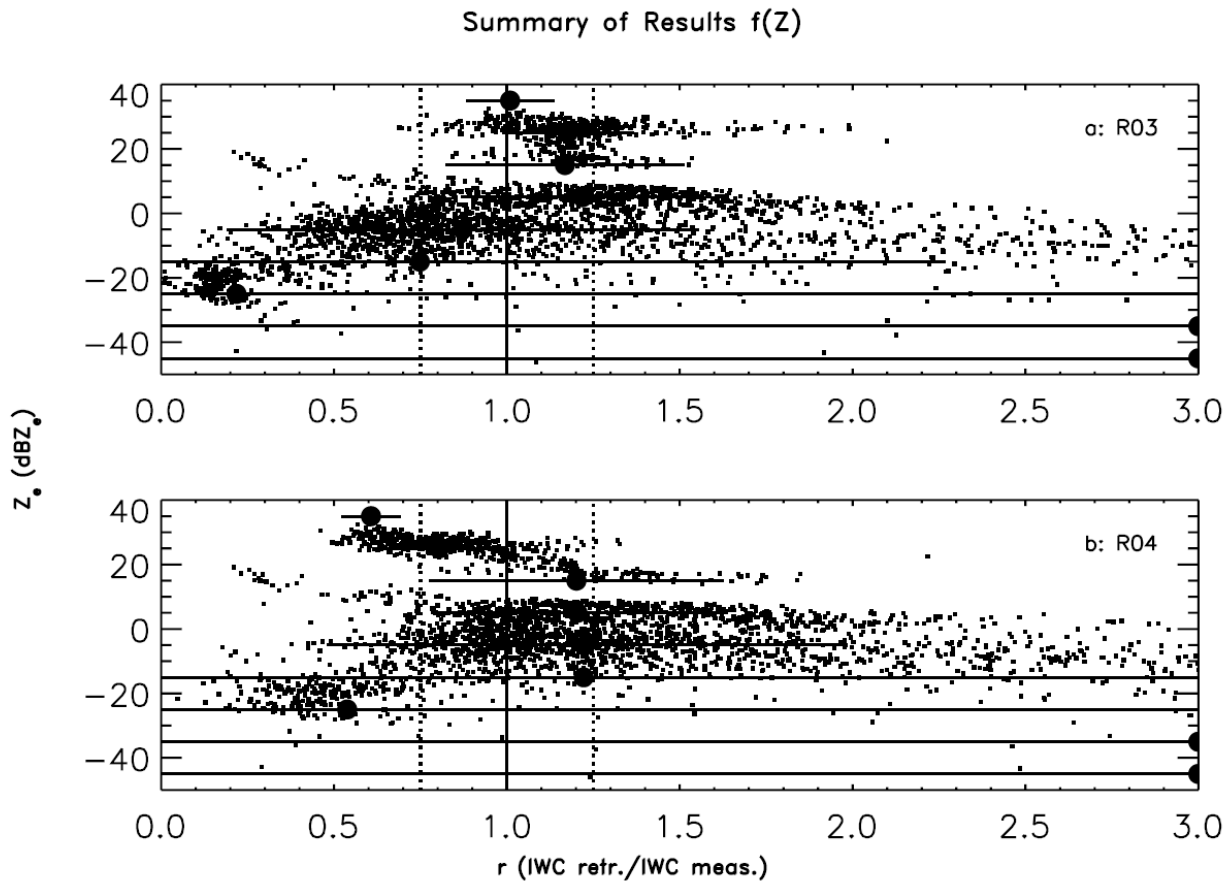
Figure 6: Ratio of retrieved to measured IWC for data from the intercomparison study described by Heymsfield et al. (2008), plotted as a function of radar reflectivity Z_e, for (a) the previous algorithm ''R03'' and (b) the current algorithm ''R04.'' Small points represent the individual measurements, while the circles and horizontal lines represent the mean and standard deviation of values in a given parameter range. The newer algorithm performs more effectively than the older version (Reproduced from Austin et al., 2009).

Another example of validation applied to ice clouds is provided by Matrosov (2015), who considered precipitating systems. For the 15 November 2010 observational case, WSR-88D-based IWP estimates are depicted in Figure 7, which corresponds to Figure 5 of Matrosov (2015). The vertical dashed lines indicate the boundaries of the ''cone of silence,'' where NEXRAD IWP estimates either are not available or are diminished because of the maximum tilt limitation. MH08, 2B-CWC-RO, and 2C-ICE IWP estimates from CloudSat are also shown in this figure. 2B-CWC-RVOD IWP values differ from 2B-CWC-RO IWP values by only a few percentage points and are not depicted. The negligible difference between IWC values corresponding to these products was also noted by Protat et al. (2010) who analysed a large set of retrievals near Darwin, Australia. It can be seen from the presented data that outside the cone of silence there is an overall good correspondence between locations of IWP maxima and minima from the ground-based retrievals and all CloudSat products. For this event, IWP values change from the maximum values of about 10 kg m^{-2} to very small values near the latitude of 31.6°. The 2B-CWC-RO product provides the smallest IWP values from all the retrievals considered here.
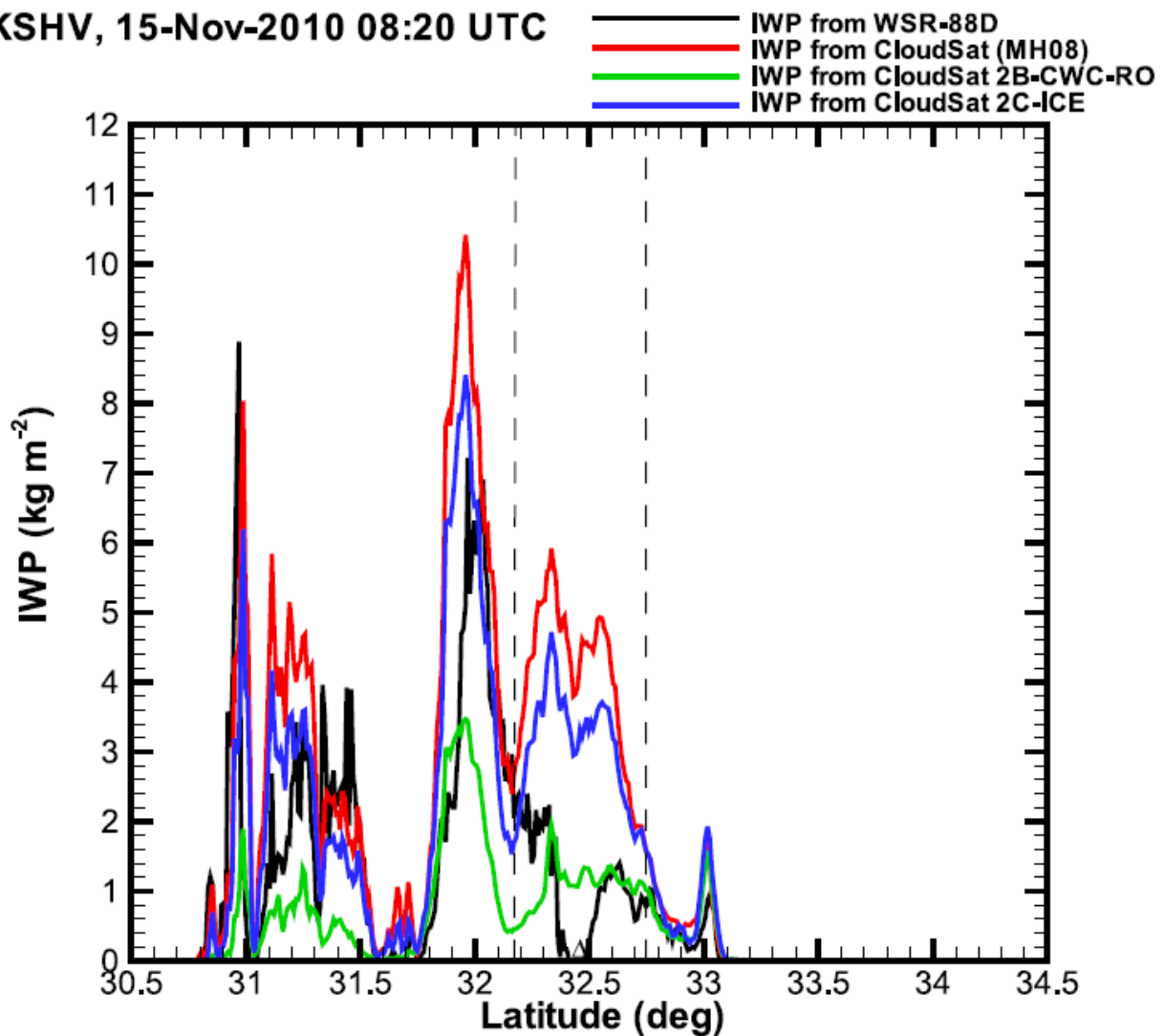
Figure 7: KSHV and CloudSat IWP retrievals along the satellite ground track on 15 Nov 2010. The black line shows WSR-88D-based IWP estimates and the vertical dashed lines represent the boundaries of the cone of silence where WSR-88D measurements are absent or not available for the whole vertical extent of the observed precipitation system. MH08, 2B-CWC-RO, and 2C-ICE IWP estimates from CloudSat are also shown in this figure. (Reproduced from Matrosov, 2015).

Conclusion: There is clearly considerable variability, and hence uncertainty, in the estimates of IWP obtained from different CloudSat data products, which each rely on particular Z_e-S relations. The CloudSat IWP produced by the various products is only in general and qualitative agreement, i.e. high or low, at certain locations.

4. DUAL-FREQUENCY RADAR ALGORITHMS
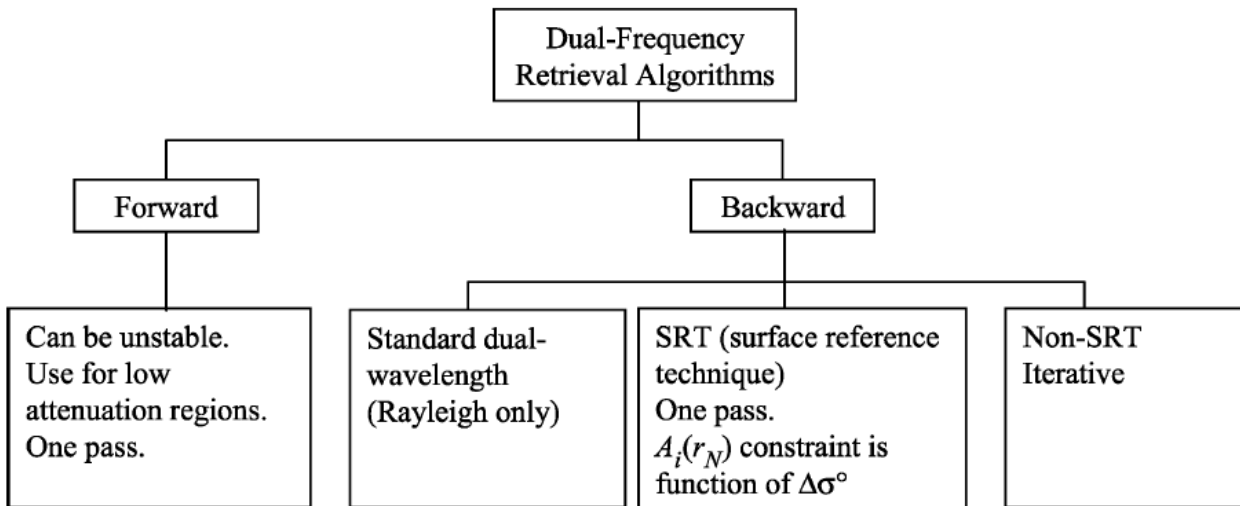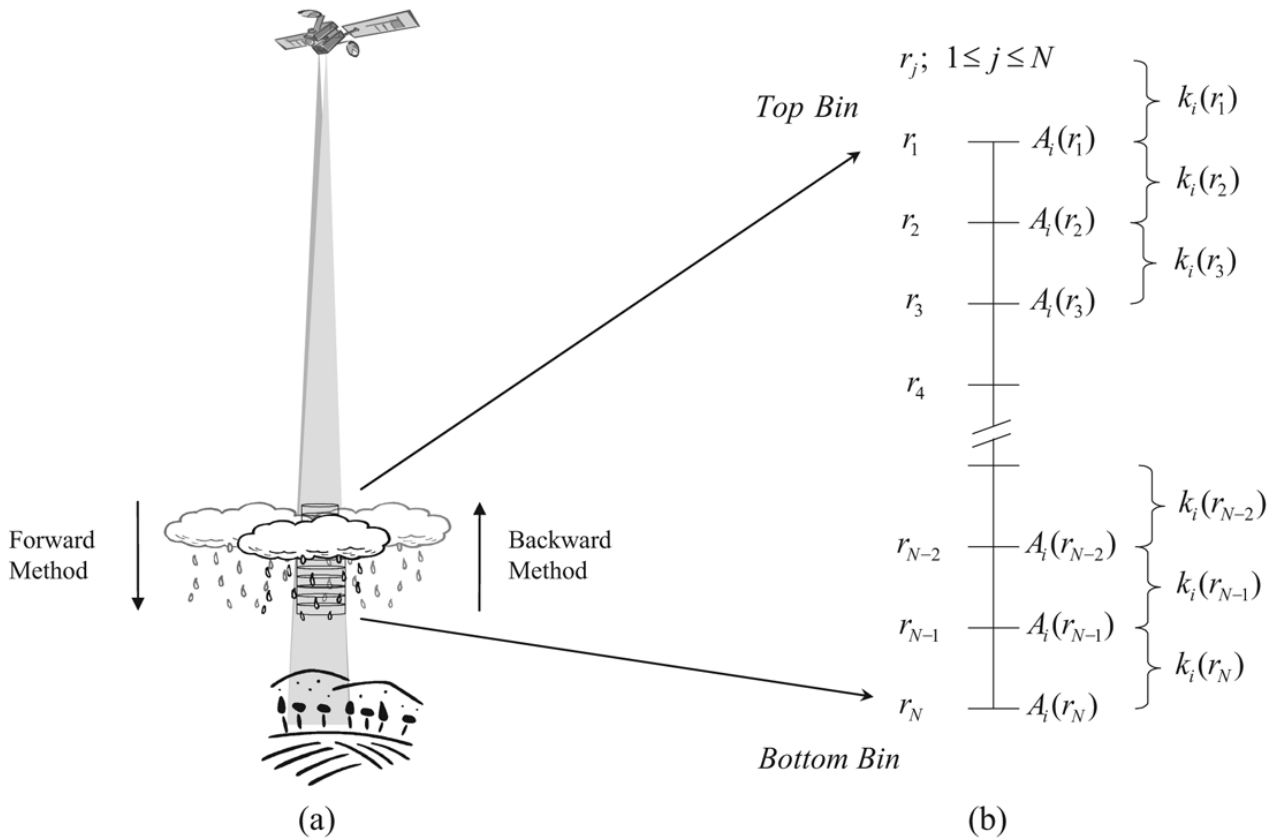
Figure 8: (a) Depiction of a downward-looking GPM satellite. The horizontal discs represent sampling volumes. The forward method calculates DSD values starting at the top and moving to the bottom. The backward method calculates from the bottom to the top. (b) Shows how the bin nomenclature and specific attenuation are defined. The lower part of the figure shows the two general types of dual-frequency retrieval algorithms: forward and backward. There are three types of backward retrieval algorithms: standard dual-wavelength, single-pass SRT-based, and non-SRT-based iterative. (Reproduced from Rose and Chandrasekar, 2005).

The Dual-frequency Precipitation Radar (DPR), deployed on the GPM Core Satellite, offers several improvements relative to its single-frequency counterpart (Hou, 2010). These include improvements in hydrometeor identification, particularly in convective rain, higher accuracy in the estimates of rain rate and water content, and information on the particle size distribution (PSD) in both rain and snow. With regard to the PSD, the DPR provides a characteristic size parameter (such as the median mass diameter, D_0) estimated from the difference (in dB) between Ku- and Ka-band attenuation-corrected radar reflectivity factors for a reasonable range of assumed gamma distribution shape parameters or snow mass densities. A characteristic number concentration of the PSD can then be found from D_0 and the radar equation. Attenuation correction, which is key to the success of any radar algorithm at these frequencies, can be accomplished either by the use of the surface as reference target or by an iteration where the PSD itself is used in a step-wise correction procedure (e.g., Meneghini et al. 1997, Mardiana et al. 2004, Rose and Chandrasekar 2006). Potentially more robust formulations (e.g. Grecu et al., 2011) have also been created using the dual-frequency airborne precipitation radar.

Dual-frequency methods have been described by Matrosov et al. (2005), who highlighted the ability to obtain independent estimates of hydrometeor effective size, particularly for the non-spherical particles that constitute ice clouds and snow. Such dual-frequency methods are covered by Rose and Chandrasekar (2005), who describe the algorithm utilized by the GPM dual-frequency precipitation radar, with operating frequencies in the Ku (13.6 GHz) and Ka (35.6 GHz) bands. Figure 8 corresponds to Figures 1 and 2 of Rose and Chadrasekar (2005) and Figure 8(a) is a depiction of the downward-looking satellite showing two rays, one for each wavelength, projected through a simple storm cloud and precipitation region. The small discs represent the resolution volumes of the radars. The DPR brought new algorithms to measure and retrieve precipitation parameters such as the DSD in each resolution volume. The underlying microphysics of precipitation structures and DSDs dictate the types of models and retrieval algorithms that can be used to estimate precipitation. One such retrieval algorithms is a dual-wavelength type that does not use the surface-reference technique (SRT). The dual-frequency retrieval approach has been known since the 1970s and has found renewed interest with the GPM DPR. Considerable work has already been done to evaluate the algorithm as a hybrid-SRT method (Meneghini et al., 1997) and as a standalone method with no SRT (Mardiana et al., 2003). Additional work has been done by Liao et al. (2003) to use the algorithm in the snow region. Inherent in the application of the dual-frequency algorithm are assumptions about the types of hydrometeors in each region: above the melting layer in snow; within the melting layer; and below the melting layer in rain. The types of hydrometeors assumed in the melting layer and above can significantly affect the retrieved DSDs and subsequent rain rate in the rain region. For GPM radar frequencies, the dual-frequency method appears to work best in low to moderate rain rates, and yields more detailed DSD information than does the single-frequency approach. Because of the potentially large attenuation of the Ka-band signal in high rain rates, the algorithm has a firm limitation on the maximum rain-rate that it can be used to measure.

Generally, there are two main types of dual-frequency algorithms that can be used with a downward-looking radar: (1) the forward method, where the DSDs are calculated at each bin starting from the top bin and moving to the bottom, see Figure 8(a); and (2) the backward method, where the algorithm begins at the bottom bin and moves upward to the top calculating the DSD parameters and attenuation along the way (Mardiana et al., 2003; Meneghini et al., 2002). The lower part of Figure 8 shows a summary diagram of these methods. The assumption with the forward method is that there is known or at least assumed attenuation above the top bin. The integral equations are solved in a single pass through the hydrometeor regions. The forward method can be unstable in moderate to high attenuation levels coincident with moderate to high rain rates (Meneghini et al.,

2002). Although backward-calculation algorithms tend to be more stable than the forward types, they also require an a priori knowledge of the total two-way path-integrated attenuation (PIA) for each ray or an ability to calculate it. The backward type of algorithm can be further divided into three groups: (1) standard dual-wavelength; (2) surface-reference technique; and (3) iterative non-SRT. The basic principle of the standard dual-wavelength approach is to estimate the path attenuation (and rain rate) using the radar equation and the ratio of the returned power of both wavelengths. This method requires one or two assumptions: first, the rain rate must be uniform over the measurement interval; or second, the reflectivity factor must be wavelength-independent, implying Rayleigh scattering at both frequencies (Chandrasekar et al., 2003). The SRT method uses a backward calculation method assuming a total path-integrated attenuation value at the bottom for each wavelength. The third method, the non-SRT algorithm, is a self-consistent algorithm wherein the total PIA for each frequency is first estimated using an initial guess, and then optimized iteratively (Mardiana et al. 2004).

Considerable work has been done to evaluate backward-calculating dual-frequency algorithms, such as a hybrid SRT method (Meneghini et al. 1997, 2002). Additionally, another retrieval algorithm is an iterative, dual-frequency type that does not use PIA derived from the SRT but instead estimates it as part of an iterative process (Mardiana et al. 2004). For GPM, the iterative dual-frequency method appears to be best suited for low-to-moderate rain rates below about 12–18 mm h^{-1} (assuming a uniform rain column, 3 km in height), and yields more detailed DSD information than does the single-wavelength method used in TRMM. Liao and Meneghini (2004) stated that under relatively high rain rates the iterative approach does not converge. Rose and Chandrasekar (2005) later showed that the dual-wavelength single-loop model (which incorporates the iterative model) can converge to incorrect DSD values when the retrieved intercept-diameter pairs are in the incorrect convergence region. Both the forward and backward methods described above suffer from multivalued solutions when retrieving the median volume diameter for rain. This outcome is described in detail by Liao et al. (2003), Mardiana et al (2004), and Meneghini et al. (2002). Rose and Chandrasekar (2006) proposed a supplementary method, using a linear model for vertical profiles of the median volume diameter and the intercept parameter in the rain region to avoid the multivalued solutions. Le et al. (2009) proposed and evaluated a hybrid approach combining the advantages of the forward method and the recursive backward method. Le et al. (2009) applied the forward method to the ice and melting ice regions to avoid large attenuation while a linear assumption was applied in the rain region. No SRT information is needed in this algorithm, which used an iterative procedure to optimize DSD parameters at the bottom of rain region by constructing the cost function along the whole vertical profile.

Kubota et al. (2014) evaluated the success of precipitation estimates using synthetic data. This study focused on evaluating the estimated precipitation rates from the single and dual-frequency algorithms at a 2-km altitude over ocean within the 125 km KaPR observation swath width. A precipitation rate calculated from the assumed DSD in the synthetic data was regarded as the true value. Figure 9, which corresponds to Figure 5 in Kubota et al. (2014), shows probability density functions (pdfs) for precipitation rates at an altitude of 2 km over the ocean for the 7 orbits of the KaPR sampling-experiment data. The units of both axes are taken to be the precipitation rate in decibels, dB Pr, i.e., $10 \times \log_{10}$ (precipitation rate). The KuPR estimates were in good agreement with the true values. For the KaPR results, distinct underestimates were found for precipitation rates of more than 6 dB Pr (about 4 mm h^{-1}), while overestimates were found for precipitation rates of less than about 4 mm h^{-1}. Differences between the KaMS and the KaHS results were small. In Figure 9(c), estimates of the DPR show underestimation in the precipitation rate for values less than 10 mm h^{-1}, and overestimation for precipitation rates of above 10 mm h^{-1}. The DSD in the synthetic data

were estimated from the PR2A25 product, and the relationship between k/Z_e and D_0 in the synthetic data was identical to that used in the algorithms. Thus, the assumptions used in the KuPR-only algorithm are consistent with the assumed DSD which provides an accuracy for the KuPR-only algorithm better than can normally be expected.
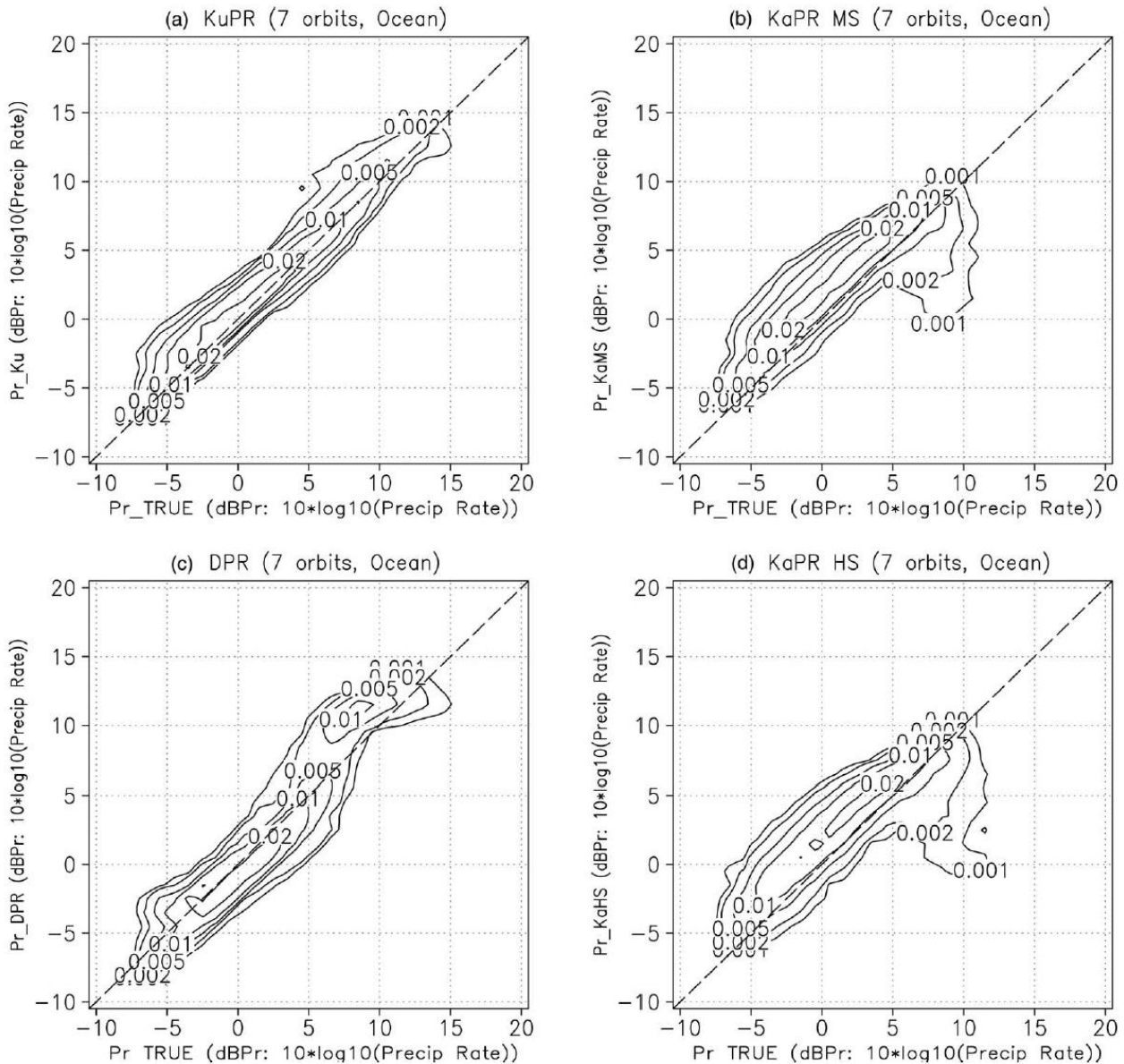
Figure 9: Pdfs of precipitation rates at an altitude of 2 km over the ocean in 7 orbits during the KaPR sampling experiment. Vertical axes are precipitation rates of (a) KuPR, (b) KaMS, (c) DPR, and (d) KaHS. All horizontal axes are precipitation rates from the true values. The units of both axes are decibel-precipitation-rate, dB Pr, i.e., $10 \times \log_{10}$ (precipitation rate). The values, -10, 0, 10, and 20 dB Pr correspond to 0.1, 1.0, 10.0, and 100 mm h^{-1}, respectively. The contours show labelled values (Reproduced from Kubota et al., 2014)
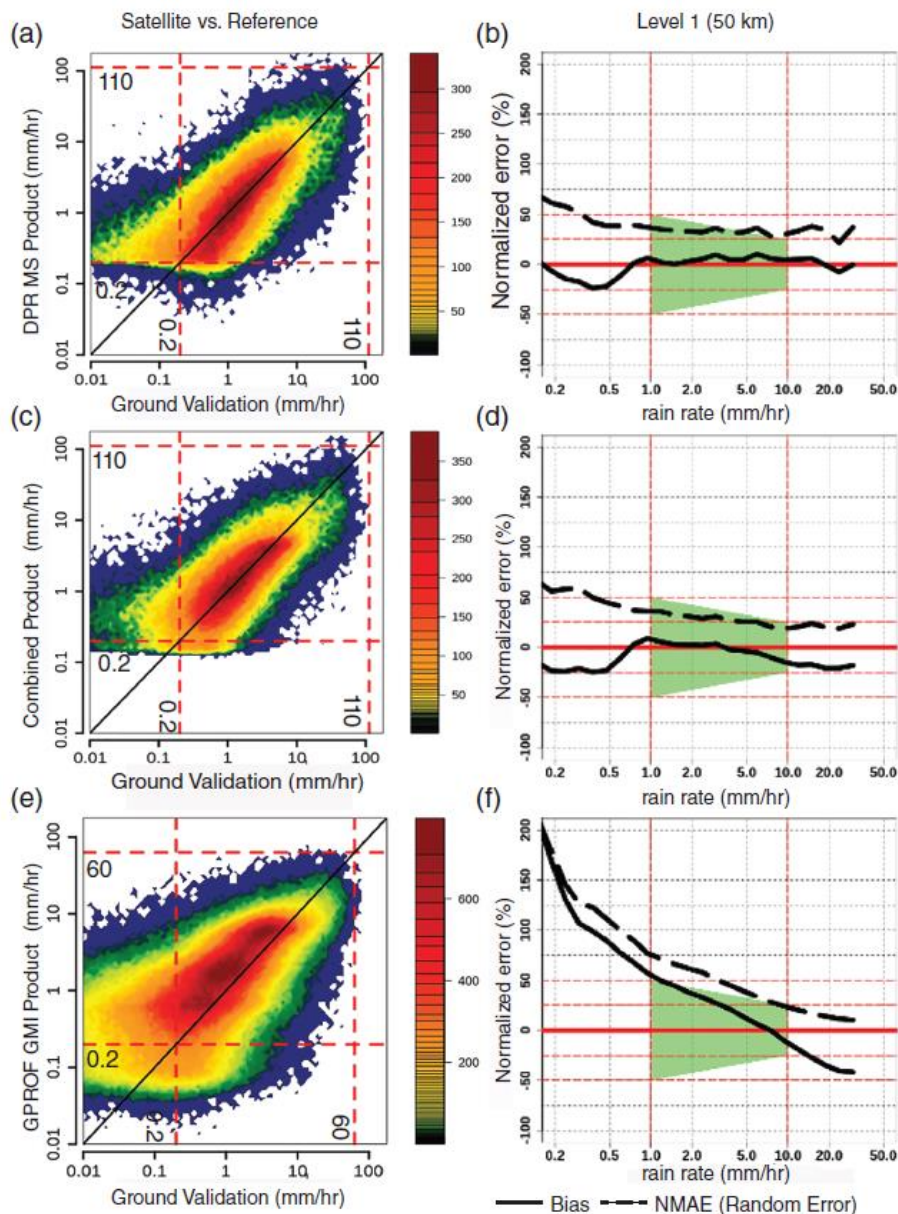
Figure 10: Validation of (a, b) DPR, (c, d) CORRA, and (e, f) GPROF GMI Products. The left column shows the satellite product versus ground validation reference for instantaneous rain rates at native resolution (5 km footprint for DPR and CORRA and 15 km effective field of view (EFOV) for GPROF GMI). Dashed lines in left column indicate that each product meets the requirements of 0.2–110 mm/h for DPR and 0.2–60 for GMI. The right column shows results averaged over 50 km for bias and normalized mean absolute error (NMAE) random error to be <25% at 10 mm/h and <50% at 1 mm/h as indicated in the green shaded area. The DPR data are from Version 05 and are the Matched Scan (Ku+Ka) retrievals (Reproduced from Skrofonick-Jackson et al., 2018)

Further to evaluations undertaken using synthetic data, Skrofonick-Jackson et al., (2018) have provided a comparison between actual GPM-derived rain rates and those obtained from ground data. Figure 10 corresponds to Figure 4 of Skrofonick-Jackson et al. (2018) and presents comparisons between rain rate estimates obtained using three GPM data products, (1) DPR (radar only), (2)

CORRA (combined radar-radiometer) and (3) GMI (radiometer only), and a value obtained at the ground that is assumed to be correct. Figure 10 demonstrates that the DPR and CORRA quantify rain rates between 0.2 and 110 mm h^{-1}, while GMI estimates rain rates up to 60 mm h^{-1} due to the averaging of strong convective cells by the coarser-resolution radiometer observations. Note that at the DPR (GMI) 5 km (15 km) footprint scales, rain rates $\geq$ 110 mm h^{-1} (60 mm h^{-1}) are very infrequent, and make up less than 0.1% of the rain occurrences over the 2.5-year sample shown. Figure 10 (right) demonstrates that GPM-CO's instantaneous rain rate bias and uncertainty are excellent, being less than 50% at 1 mm h^{-1} and less than 25% at 10 mm h^{-1}. The errors are less at 10 mm h^{-1} since this is where both the Ku and Ka channels on DPR are sensitive to the rain and provide additional constraints for both the DPR and CORRA algorithms. In Figure 10e, the GMI biases run a little high at 1 mm h^{-1}, probably due to the GMI mistaking some land surface features for low rain rates. See section 6 below for a discussion regarding combined radar-radiometer algorithms.

An important objective of the GPM mission is the detection of falling snow, since it accounts for a significant fraction of precipitation in mid to high latitudes (Casella et al., 2017b). The GPM DPR is designed with enhanced sensitivity to detect lighter liquid and solid precipitation. Casella et al. (2017b) assessed the DPR's ability to identify snowfall using near-coincident CloudSat CPR observations and products as an independent reference dataset. CloudSat's near global coverage and the high sensitivity of its W-band CPR make it suitable for snowfall-related research. While DPR/CPR radar sensitivity disparities contribute substantially to snowfall detection differences, other factors such as precipitation phase discriminators that produce snowfall identification discrepancies are also analysed. Results show that even if the occurrence of snowfall events correctly detected by DPR products is quite small compared to CPR (around 5–7%), the fraction of snowfall mass is not negligible (29–34%). A direct comparison of CPR and DPR reflectivities illustrates that DPR misdetection is worsened by a noise-reducing DPR algorithm component that corrects the measured reflectivity. This procedure eliminates the receiver noise and side lobe clutter effects, but also removes radar signals related to snowfall events that are associated with relatively low reflectivity values. In an effort to increase DPR signal fidelity associated with snowfall, Casella et al. (2017b) propose a simple algorithm using matched DPR Ku/Ka radar reflectivities producing an increase in the fraction of snowfall mass detected by DPR of up to 59%.
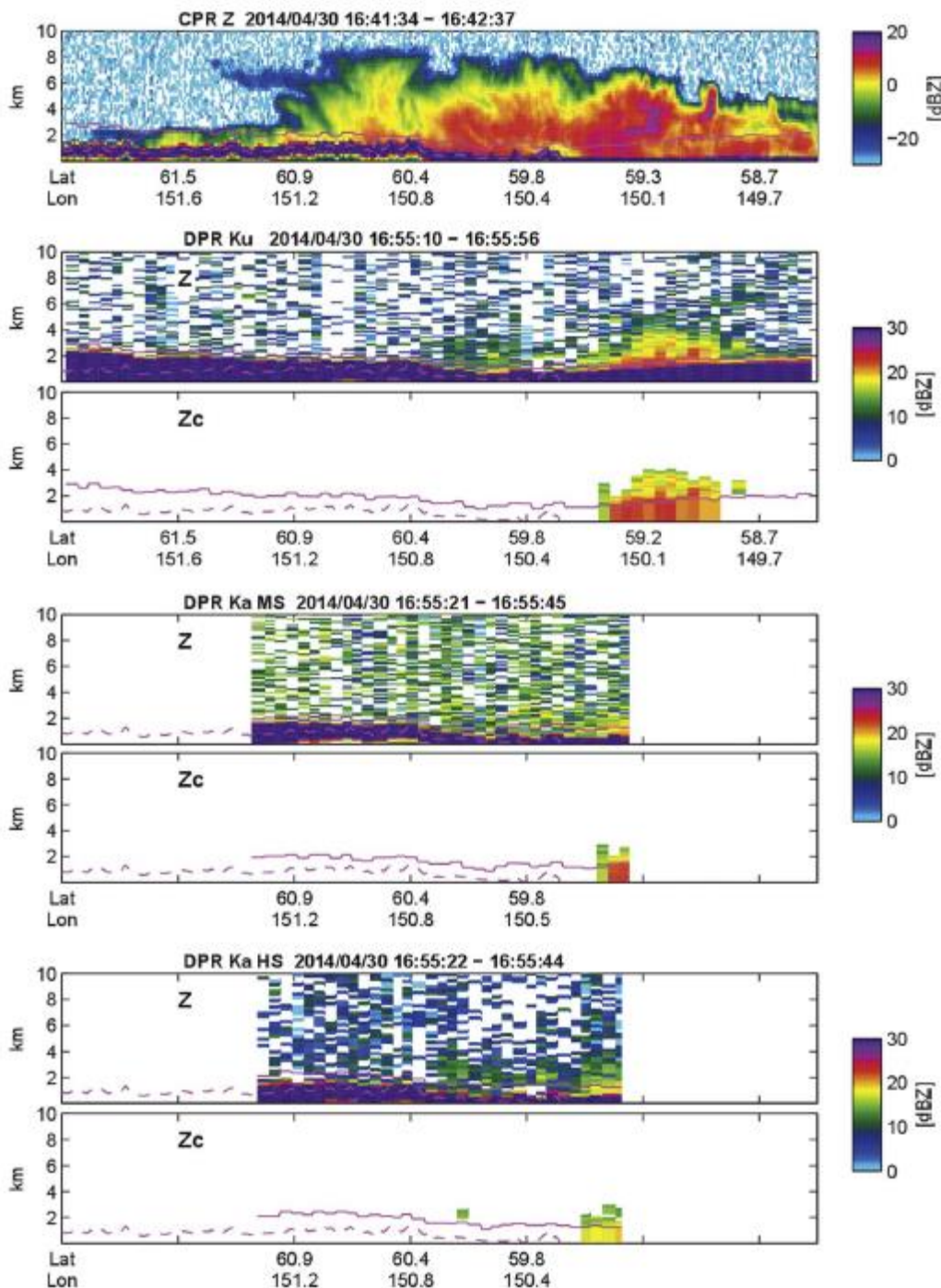
Figure 11: Cross section of one coincident observation from CloudSat CPR and GPM DPR for a snowfall case study on 30 April 2014. Figure panels show from top to bottom CPR reflectivity, DPR Ku Normal Scan (NS) measured and corrected reflectivity, DPR Ka Matched Scan (MS) reflectivity and Ka High Sensitivity scan (HS) measured and corrected reflectivity (version 4). Every panel shows also the surface level (from CPR) and the clutter-free bin height (from DPR) as dashed and continuous magenta lines. (Reproduced from Casella et al., 2017b)

Figure 11 corresponds to Figure 2 of Casella et al. (2017b) and shows CPR reflectivity profiles, as well as both the measured (Z) and corrected (Zc) DPR reflectivity profiles as they appear in 2ADPR

product version 4, for a coincident observation of a snowfall event on 30 April 2014. This widespread frontal snowfall event, which is part of the combined CPR-DPR snowfall dataset, occurred over Eastern Russia north of the Sea of Okhotsk. The more sensitive CPR indicated maximum echo top height between ~5–8 km from ~58.5° to 61° latitude. Typical maximum radar reflectivity values were between 10 and 15 dBZ, with some embedded regions exceeding these values. The CPR also observed shallower cloud structures with echo top height less than ~2 km capable of producing snow north of 61° latitude. CPR reflectivity values associated with the shallower snowfall are consistently weaker than the deeper snowfall located further south. The DPR Ku uncorrected reflectivity profiles reveal some structure below ~4 km in the deeper snowfall segment of this event between ~58.8°–60° latitude, but most of the event north of 60° latitude and at higher altitudes is missed by the DPR due to the relatively poor radar sensitivity. The DPR footprint size may also have an impact on the detection capabilities especially when observing smaller cloud structures. The DPR Ka-MS and Ka-HS products indicate minimal structure in the inner DPR scan swath. Maximum Ku DPR reflectivities appear higher than the CPR reflectivities near the surface in the most intense precipitation cores, as maximum Ku reflectivities exceed 20 dBZ. Ku/W reflectivity discrepancies are an expected manifestation of non-Rayleigh scattering effects, as well as attenuation from supercooled liquid water (Hiley et al., 2011), that can suppress W-band reflectivity values associated with larger frozen hydrometeors compared to coincident Ku-band observations.

It is also clear that the measured reflectivity has values near the limit of the radar sensitivity and it is affected by a significant receiver noise component that can be as intense as around 12 dBZ (Ku and Ka-HS) or 18 dBZ (Ka-MS). While this effect is common in the database analysed by Casella et al. (2017b), the corrected reflectivity shows the complete suppression of receiver noise and also the correction for attenuation to levels below the surface clutter level. Unfortunately the suppression of the receiver noise also eliminates part of the weak signal that is related to snowfall (e.g. in the Ku cross section between 60.1° and 59.4° in latitude). Comparing the CPR and DPR reflectivity, it is clear that the regions where some signal is detected are more limited for the DPR both in the horizontal and vertical scale, even considering the different minimum height where these instruments are not affected by ground clutter. The presence of an intense receiver noise in the DPR data is a strong limitation for the measurement of the weak signals related to snowfall, however the presence of strong echoes due to sidelobe clutter is probably more detrimental to precipitation retrievals.

Conclusion: Rain rates up to 110 mm h^{-1} can be quantified by the GPM DPR rainfall algorithm. The errors are lower at 10 mm h^{-1} than at, say, 1 mm h^{-1} since this is where both the Ku and Ka channels on the DPR are sensitive to the rain and provide additional constraints for both the radar-only and radar-radiometer algorithms. Snowfall is also well characterized by the DPR, although data corresponding to lower snowfall rates are sometimes lost because of a correction used to remove receiver noise and sidelobe clutter effects.

5. TRIPLE-FREQUENCY RADAR ALGORITHMS

Triple-frequency techniques have been discussed by Mason et al. (2019), who covered radar observations of snow, Grecu et al. (2018), who investigated a nonparametric method for estimating precipitating ice, Leinonen et al. (2018), who developed an algorithm to retrieve microphysical properties pertaining to snow, and Battaglia et al. (2019), who discussed the application of a triple-frequency retrieval technique to data from aircraft. Battaglia et al. (2019) covered the possibility of retrieving DSD parameters if triple-frequency radar measurements are available and effective DFRs for the pairs Ku-Ka and Ka-W can be derived. The main obstacle to performing such a triple-frequency retrieval resides however in the assumption that effective DFR can be derived from the measurements. For rain, attenuation increases rapidly with frequency and with rain rate and can be challenging to account for, and it can reduce the received radar power significantly, e.g. from ranges beyond those corresponding to heavy rain layers down into the noise level. Additional sources of attenuation (e.g. caused by cloud liquid droplets or melting particles; Matrosov, 2008) can further complicate the problem. For ice and snow, when combining frequencies for which different parts of the size distribution transition from the Rayleigh to the non-Rayleigh scattering regime, Z_e of the frequency which is more affected by non-Rayleigh scattering will be reduced. Once three frequencies are combined, a separation between aggregates and the more spheroidal shapes appears. Because of the only recent availability of triple-frequency airborne radar observation datasets, the development and testing of triple-frequency retrieval are topics of current research. When attenuation severely affects the higher frequency channels (as for when supercooled liquid or heavily rimed precipitation is present and/or when the microphysical retrieval is run for the entire precipitation column) triple-frequency retrievals are based on optimal estimation (L'Ecuyer and Stephens, 2002; Grecu et al., 2011; Mason et al., 2017) approaches, which disentangle non-Rayleigh and attenuation effects by optimizing a cost function via an iterative process based on a forward model radar operator (e.g. Haynes et al., 2007; Hogan and Battaglia, 2008; Battaglia et al., 2016a). Bayesian approaches have also been recently developed for retrieving ice-only microphysics under the assumption that effective reflectivities can be recovered (Leinonen et al., 2018). But to date only a few cases have been applied to three (or more) frequency radar observations (Battaglia et al., 2016b; Battaglia et al., 2015; Battaglia et al., 2016a; Leinonen et al., 2018).

An example of an optimal estimation retrieval applied to the data collected by the Airborne Third Generation Precipitation Radar (APR-3; Sadowy et al., 2003) flown on board the NASA DC-8 aircraft during the OLYMPEX field campaign (details in Houze et al., 2017) is depicted in Figure 12, corresponding to Figure 5 in Battaglia et al. (2019). Results are presented for two different retrieval methodologies. The first is the method proposed in Tridon et al. (2018) (TRI18) and is applicable to the whole precipitation column (left-hand panels) except the melting layer (white band). A preliminary classification mask identifies the ice, melting and rain region (bottom right panel in Figure 4 of Battaglia et al., 2019) and roughly categorizes the different types of ice. Only results for one scattering model, the lightly rimed B-model with LWP = 100 g m^{-2} proposed by Leinonen and Szyrmer (2015), are shown here (left panels). Such a model was found to be the best one for reconciling in-situ and radar remote sensing measurements for the whole campaign. The second is the retrieval described in Leinonen et al. (2018) (LEI18), which is applicable only for the ice phase and uses lookup tables mapping the measurement space to the state space (right-hand columns). The microphysics is here illustrated in terms of mean mass-weighted particle size (top panels) and equivalent water content (centre panels). The bulk ice density as defined in Leinonen et al. (2018) (bottom right) clearly shows a vertical evolution of ice particles from bulk ice density at the top of the cloud (small ice crystals) to much smaller densities corresponding to fluffier

snowflakes close to the freezing level. From a direct comparison of the two retrievals it is clear that LEI18 produces ice particles smaller than TRI18 and slightly larger ice water contents. Figure 12 also shows that for the full-column retrieval (left) there is a reasonable flux continuity between the top and the bottom of the melting level (bottom panel). In-situ validation data are provided by the Citation aircraft that was flying below the DC-8 (track highlighted in the top panels of Figure 4 in Battaglia et al., 2019). An intercomparison between in-situ and retrieved microphysical properties in the ice part for the upper leg is shown in Figure 6 of Battaglia et al. (2019). The retrieved values are comparable but it remains challenging, given the uncertainties in the in-situ measurements and the collocation/sampling issues, to draw definitive conclusions about the quality of the two retrievals.
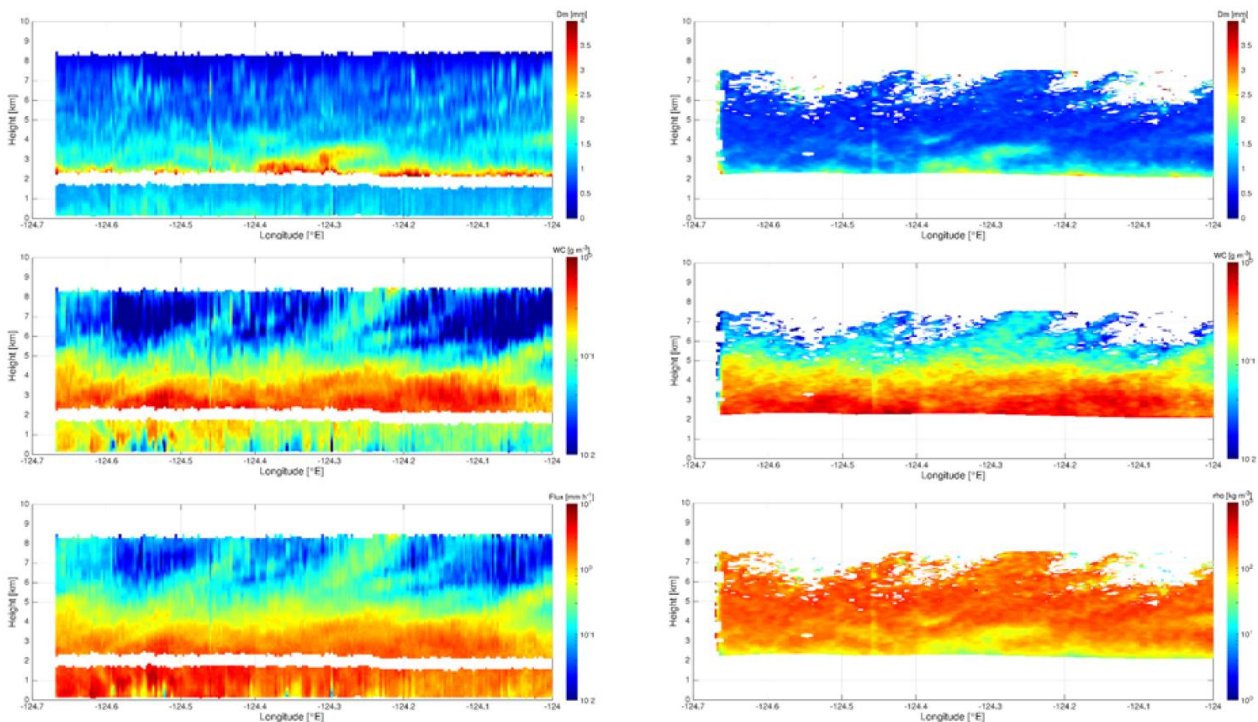
Figure 12: Retrieved parameters for the leg shown in Figure 4 of Battaglia et al. (2019): mean mass-weighted maximum size (top), IWC (centre) and flux (bottom). The right bottom panel shows the bulk ice density as defined in Leinonen et al. (2018). (Reproduced from Battaglia et al., 2019)

Conclusion: A lack of validation presently exists for triple-frequency observations, which would therefore be enhanced significantly through the presence of more such validating data. Bearing in mind that all models have assumptions and associated uncertainties, which lead to divergent conclusions and retrieval results, then validation is best conducted for particular microphysical regions where the information content is high, i.e. in regions where retrievals with different frequencies would give different results, e.g. varying particle size distribution, particle habit etc.

6. RADAR-RADIOMETER ALGORITHMS

During the TRMM era, several algorithms for estimating precipitation from a combination of radar and microwave radiometer observations were developed (Grecu et al., 2016). The TRMM observatory included a single-frequency (Ku band) crosstrack scanning radar and a multichannel (10–85 GHz), conically scanning passive microwave radiometer (see Kummerow et al. 1998). Radar and radiometer observations coincided over the 245-km radar swath. Haddad et al. (1997) used a Bayesian approach to adjust path-integrated attenuation in the near-vertical columns of the radar scans using independent estimates of path-integrated attenuation from radar observations of surface reflection (Meneghini et al. 2000) as well as observed microwave radiances. Grecu et al. (2004) later formulated a variational approach to radar–radiometer estimation of precipitation from TRMM. Similar to Haddad et al. (1997), a parameter of the precipitation particle size distribution was used to optimize the path-integrated attenuation in each radar profile, but microwave radiances were also simulated in the same forward model framework. Masunaga and Kummerow (2005) developed a combined algorithm methodology based on cloud-resolving model simulations and an iterative search procedure that determined the pre-calculated observations most consistent with the actual observations. An approach similar to that of Grecu et al. (2004) but based on a Gauss–Newton inversion methodology rather than adjoint modelling was developed by Munchak and Kummerow (2011).

At the heart of the GPM Mission are the radar and radiometer measurements provided by the Core Observatory. Along with the associated radar-radiometer algorithms, these data provide detailed and accurate information on the characteristics of precipitation. Although the existing TRMM combined algorithms could, in principle, have been extended to the GPM instruments, they were not able to readily process the additional information provided by the GPM Core Observatory. One obvious extension of the existing TRMM formulations is the inclusion of a Ka-band radar specific term in the maximum likelihood functional that lies at the core of these algorithm formulations (Grecu et al. 2004; Munchak and Kummerow 2011). Since this approach is also consistent with existing dual-frequency radar estimation methods (Grecu et al. 2011), it is deemed the most seamless extension of existing approaches able to make use of GPM observing capabilities. However, to circumvent the difficulties generally arising from the use of complex forward models in inverse problems, an alternative ensemble-based statistical minimization procedure that does not require adjoint modelling or expensive finite difference sensitivity calculations was utilized. A similar approach was previously demonstrated in Grecu and Olson (2008).

The combined GPM radar-radiometer algorithm has been described in detail by Grecu et al. (2016). While the DPR algorithms represent a major advancement over the TRMM PR by providing not only estimates of the 3D precipitation structure but also estimates of the PSD characteristics, ambiguities still exist as a result of a number of assumptions. These assumptions include the vertical profiles of water vapour and cloud liquid water as well as the 'shape' parameter, μ, of the size distribution and the mass densities of snow aggregates and graupel. The purpose of the combined DPR+GMI retrieval is to use the multi-channel GMI radiances as additional constraints on the DPR profiling algorithm over the radar swath. Specifically, some of the aforementioned assumptions can be constrained by using variational procedures that minimize departures between simulated and observed brightness temperatures, or by using filtering approaches which determine an ensemble of radar solutions that are consistent with the brightness temperatures and their uncertainties. Therefore, the resulting combined precipitation retrievals are consistent with both DPR reflectivity profiles and multi-channel GMI radiances within the framework of maximum-likelihood estimation. The combined retrieval methodology is based on approaches developed and tested within the

TRMM mission. Improvements include the incorporation of a more complex radar-only retrieval algorithm, the optimization over an extended set of assumptions, and the inclusion of uncertainty estimates in the final products. The combined DPR+GMI retrievals, which provide high-quality precipitation estimates, have been used to construct an a priori database that relates hydrometeor profiles to microwave radiances over the range of observed brightness temperatures. The advantage of databases constructed directly from combined observations over cloud-model derived databases has previously been demonstrated (e.g. Grecu and Olson, 2006). This database is applicable not only to the Core GMI retrieval but also to constellation radiometer retrievals.

Conclusion: As for the GPM DPR radar-only algorithms, the combined radar-radiometer technique can also quantify rain rates up to 110 mm h^{-1}, and has errors that are lower at 10 mm h^{-1} since this is where both the Ku and Ka channels on DPR are sensitive to the rain and provide additional constraints for both the DPR and CORRA algorithms.

7. COMPARISONS OF SATELLITE PRECIPITATION ALGORITHMS
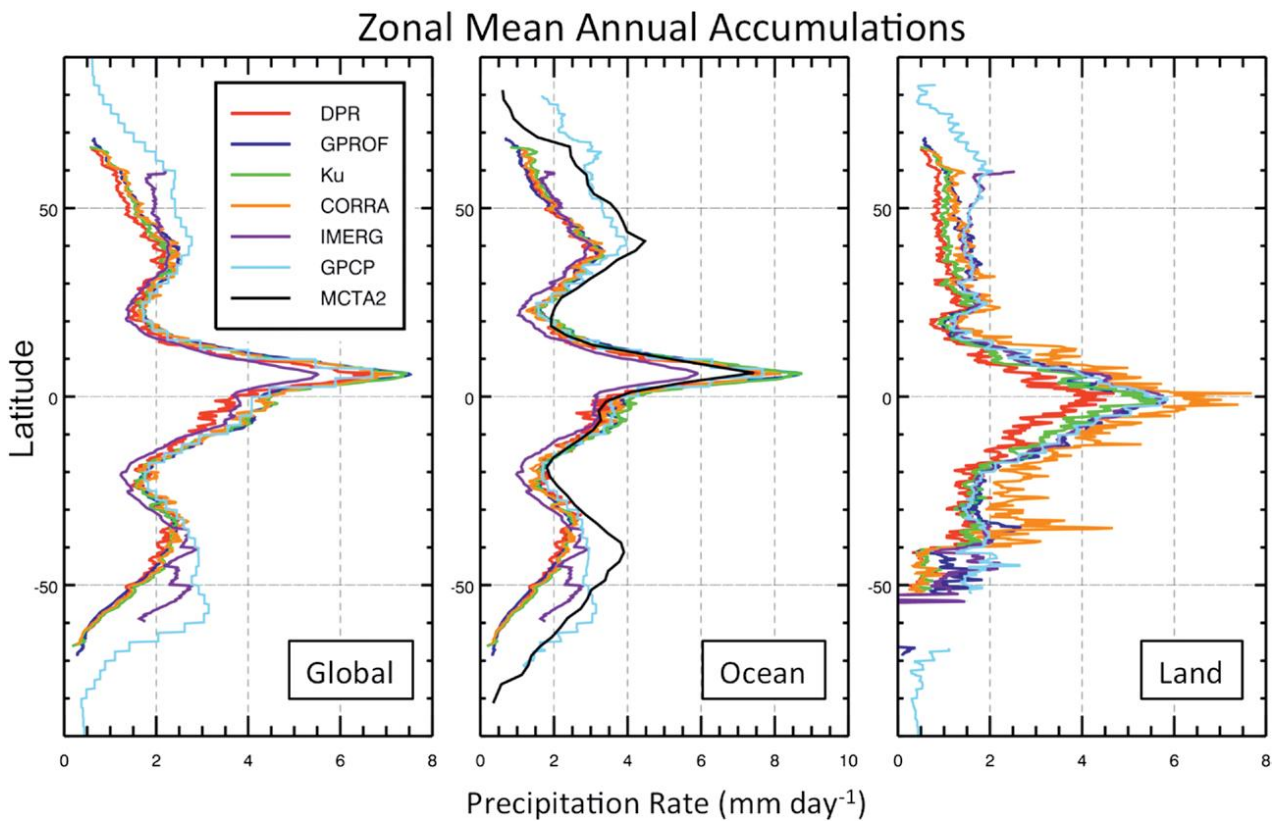
Figure 13: Zonal precipitation averages (mm day^{-1}) for the full annual cycle during 2015. The five estimates are GPM DPR (dual-frequency radar; red), GPM GPROF (GMI passive radiometer; blue), GPM Ku band (single-frequency radar; green), GPM CORRA (DPR + GMI; orange), IMERG (GPM merged with constellation estimates; purple), GPCP global estimates (light blue), and MCTA2 estimates over ocean (black, covering the years 2007–10). The GPCP is version 2.3, MCTA is version 2, IMERG is version 03, and the other GPM products are version 04. (Reproduced from Skofronick-Jackson et al., 2017).

A good example of validation efforts, in the context of GPM algorithms and data, has been provided by Skofronick-Jackson et al., (2017), who highlighted the importance of direct statistical validation

and verification of satellite estimates against high-quality ground measurements and physical validation for algorithm improvement and hydrological models. Validating data are garnered from both regular ongoing surface observations and focused field campaigns (Hou et al. 2014). Major GPM validation efforts include (1) comparisons among satellite precipitation products, (2) comparisons against ground datasets, and (3) analyses for meeting mission requirements.

One evaluation technique compares the zonal means among the various GPM instrument algorithms and established precipitation estimates such as the Global Precipitation Climatology Project (GPCP) datasets (Adler et al. 2003) and, over ocean, the Merged CloudSat, TRMM, and Aqua version 2 (MCTA2) dataset (Behrangi et al. 2014). Both GPCP and MCTA2 include a variety of input datasets selected for their utility in precipitation estimation at both low and high latitudes. Shown are the global zonal means for 2015 for land and ocean (Figure 13a), ocean only (Figure 13b), and land only (Figure 13c). Figure 13, corresponding to Figure 5 in Skofronick-Jackson et al. (2017), illustrates that DPR, Ku-band, CORRA, and GPROF algorithm retrievals are in good agreement. The GPM zonal accumulations underestimate with respect to the MCTA at higher latitudes. This is most attributable to the fact that the DPR minimum detectable reflectivities correspond to minimum rain rates of approximately 0.2 mm h^{-1}. Since much of the higher-latitude precipitation is light, and CORRA and GPROF are based on DPR estimates, GPM is low in the higher latitudes. A high-latitude, light-precipitation solution for GPROF was implemented in the version 05 algorithm release. Examining the mean daily precipitation (mm day^{-1}) for each of the algorithms shows that IMERG's annual precipitation is lower than the other algorithms while there are interesting differences among the diverse approaches over land. Land surfaces tend to complicate the retrieval process and the various algorithms use different approaches to mitigate surface (emissivity and clutter) issues.

Conclusion: GPM precipitation methods return a variety of precipitation-related accumulations dependent on the nature of the algorithm used to calculate them. It is evident that there is a notable discrepancy in the accumulations given by the IMERG method.

8. REFERENCES

Abel, S. J., and I. A. Boutle, 2012: An improved representation of the raindrop size distribution for single-moment microphysics schemes, *Q. J. R. Meteorol. Soc.*, 138, 2151 – 2162

Adler, R. F., G. J. Huffman, A. Chang, R. Ferraro, P. Xie, J. Janowiak, B. Rudolf, U. Schneider, S. Curtis, D. Bolvin, A. Gruber, J. Susskind, P. Arkin, and E. Nelkin, 2003: The version 2 Global Precipitation Climatology Project (GPCP) monthly precipitation analysis (1979-present). *J. Hydrometeor*, 4(6), 1147-1167, doi:10.1175/1525-7541(2003)004<1147:TVGPCP>2.0.CO;2.

Alishouse, J. C., R. R. Ferraro, and J. V. Fiore, 1990: Inference of Oceanic Rainfall Properties from the Nimbus 7 SMMR. *J. Appl. Meteor.*, 29, 551–560, https://doi.org/10.1175/1520-0450(1990)029<0551:IOORPF>2.0.CO;2

Aonashi, K., J. Awaka, M. Hirose, T. Kozu, T. Kubota, G. Liu, S. Shige, S. Kida, S. Seto, N. Takahashi, Y. Takayabu, 2009: "GSMaP passive microwave precipitation retrieval algorithm: Algorithm description and validation", *J. Meteorol. Soc. Jpn.*, vol. 87A, pp. 119-136, 2009.

Austin, R. T., and G. L. Stephens, 2001: Retrieval of stratus cloud microphysical parameters using millimeter-wave radar and visible optical depth in preparation for CloudSat: 1. Algorithm formulation. *J. Geophys. Res.*, 106, D22, 28233-28242.

Austin, R. T., A. J. Heymsfield, and G. L. Stephens, 2009: Retrieval of ice cloud microphysical parameters using the CloudSat millimeter-wave radar and temperature. *J. Geophys. Res.*, 114, D00A23, doi:10.1029/2008JD010049.

Battaglia, A., S. Tanelli, K. Mroz, and F. Tridon, 2015: Multiple scattering in observations of the GPM dual-frequency precipitation radar: evidence and impact on retrievals. *J. Geophys. Res.*, 10.1002/2014JD022866.

Battaglia, A., K. Mroz, T. Lang, F. Tridon, S. Tanelli, G. Heymsfield, and L. Tian, 2016a: Using a multi-wavelength suite of microwave instruments to investigate the microphysical structure of deep convective cores. *J. Geophys. Res. Atm.*, doi: 10.1002/2016JD025269.

Battaglia, A., K. Mroz, F. Tridon, S. Tanelli, and P.-I. Kirstetter, 2016b: Multiple-scattering-induced "ghost echoes" in GPM-DPR observations of a tornadic supercell. *J. Appl. Meteorol. Climatol.*, 55, 1653–1666, dOI: 10.1175/JAMC-D-15-0136.1.

Battaglia, A., Tanelli, S., Tridon, F, Kneifel, S., Leinonen J, Kollias, P., 2019, Triple-frequency radar retrievals, chapter in the book Satellite precipitation measurement, Editor in Chief: Vincenzo Levizzani, Springer

Behrangi, A., G. Stephens, R. F. Adler, G. J. Huffman, B. Lambrigtsen, and M. Lebsock, 2014: An update on the oceanic precipitation rate and its zonal distribution in light of advanced observations from space. *J. Climate*, 27, 3957–3965, doi:10.1175/JCLI-D-13-00679.1.

Benedetti, A., G. L. Stephens, and J. M. Haynes, 2003, Ice cloud microphysics retrievals from millimeter radar and visible optical depth using an estimation theory approach, 2003, *J. Geophys. Res.*, 108(D11), 4335, doi:10.1029/2002JD002693.

Bohren, C. F.; Huffmann, D. R. (2010). Absorption and scattering of light by small particles. *New York: Wiley-Interscience*. ISBN 3-527-40664-6.

Boukabara, S. A., Garrett, K., Chen, W. C., Iturbide-Sanchez, F., Grassotti, C., Kongoli, C., Chen, R. Y., Liu, Q. H., Yan, B. H., Weng, F. Z., Ferraro, R., Kleespies, T. J., & Meng, H. (2011). MiRS: An All-Weather 1DVAR Satellite Data Assimilation and Retrieval System. *IEEE Transactions on Geoscience and Remote Sensing*, 49(9), 3249-3272.

Casella, D., L. M. Amaral, S. Dietrich, A. C. Marra, P. Sanò, and G. Panegrossi,, 2017a: The Cloud Dynamics and Radiation Database algorithm for AMSR2: exploitation of the GPM observational dataset for operational applications, *IEEE J. of Sel. Topics in Appl. Earth Obs. and Rem. Sens. (J-STARS)*, 10(8), DOI : 10.1109/JSTARS.2017.2713485

Casella, D., G. Panegrossi, P. Sanò, A. C. Marra, S. Dietrich, B. T. Johnson, and Mark S. Kulie; 2017b: Evaluation of the GPM-DPR snowfall detection capability: Comparison with CloudSat-CPR, *Atmos. Res.*, 197, 64-75

Chandrasekar, V., R. Meneghini, and I. Zawadzki, 2003, Global and local precipitation measurements by radar, in *Meteorological Monographs Series*. Washington, DC: AMS, Aug. 2003, vol. 30, no. 52.

Chang, A. T. C., and A. S. Milman, 1982: Retrieval of ocean surface and atmospheric parameters from multichannel microwave radiometric measurements. *IEEE Trans. Geosci. Electron.*, GE-20, 217-224.

Comstock, K. K., R. Wood, S. E. Yuter, and C. Bretherton; 2004: Reflectivity and rain rate in and below drizzling stratocumulus, *Q. J. Roy. Meteorol. Soc.*, 130, 2891-2919. doi: 10.1256/qj.03.187.

Conner, M.D. and G.W. Petty, 1998: Validation and Intercomparison of SSM/I Rain-Rate Retrieval Methods over the Continental United States. *J. Appl. Meteor.*, 37, 679–700, https://doi.org/10.1175/1520-0450(1998)037<0679:VAIOSI>2.0.CO;2

Durán-Alarcón, C., B. Boudevillain, C. Genthon, J. Grazioli, N. Souverijns, N. P. M. van Lipzig, I. V. Gorodetskaya, and A. Berne: The vertical structure of precipitation at two stations in East Antarctica derived from micro rain radars, The Cryosphere, 13, 247–264, doi:10.5194/tc-13-247-2019, 2019.

Ebtehaj, A. M., and C. D. Kummerow, 2017: Microwave retrievals of terrestrial precipitation over snow-covered surfaces: A lesson from the GPM satellite. *Geophys. Res. Lett.*, 2017, 44, 6154–6162, doi:10.1002/2017GL073451.

Engelen, R. J., and G. L. Stephens, 1999: Characterization of water vapour retrievals from TOVS/HIRS and SSM/T-2 measurements. *Quart. J. Roy. Meteor. Soc.*, 125, 331–351.

Eriksson, P., M. Jamali, J. Mendrok and S. A. Buehler, 2015: On the microwave optical properties of randomly oriented ice hydrometeors, *Atmos. Meas. Tech.*, 8, 1913–1933, 2015, doi:10.5194/amt-8-1913-2015

Evans, K. F., J. Turk, T. Wong, and G. L. Stephens, 1995: A Bayesian Approach to Microwave Precipitation Profile Retrieval. *J. Appl. Meteor.*, 34, 260–279.

Ferraro, R. R., F. Weng, N. C. Grody, and A. Basist, 1996: An Eight-Year (1987–1994) Time Series of Rainfall, Clouds, Water Vapor, Snow Cover, and Sea Ice Derived from SSM/I Measurements. *Bull. Amer. Meteor. Soc.*, 77, 891–906, https://doi.org/10.1175/1520-0477(1996)077<0891:AEYTSO>2.0.CO;2

Ferraro, R. R., F. Weng, N. C. Grody, and L. Zhao, 2000: Precipitation characteristics over land from the NOAA-15 AMSU sensor. *Geophys. Res. Lett.*, 27, 2669 – 2672.

Gloerson, P., and L. Hardis, 1978: The sanning multichannel microwave radiometer (SMMR) experiment. *Nimbus-7 User's Guide*. NASA Goddard Space Flight Center, 213-245.

Gong, J., and D. L. Wu, 2017: Microphysical properties of frozen particles inferred from Global Precipitation Measurement (GPM) Microwave Imager (GMI) polarimetric measurements. *Atmos. Chem. Phys.* 2017, 17, 2741–2757.

Grecu, M., and W. S. Olson, 2006: Bayesian estimation of precipitation from satellite passive microwave observations using combined radar–radiometer retrievals. *J. Appl. Meteor. Climatol.*, 45, 416–433.

Grecu, M., L. Tian, W. S. Olson, and S. Tanelli, 2011: A Robust Dual-Frequency Radar Profiling Algorithm. *J. Appl. Meteorol. Climatol.*, 50, 1543–1557.

Grecu, M., W. S. Olson, S. J. Munchak, S. Ringerud, L. Liao, Z. Haddad, B. L. Kelley, and S. F. McLaughlin, 2016: The GPM Combined Algorithm, *J. Atmos. Ocean. Tech.*, 33, 2225-2245, doi: 10.1175/JTECH-D-16-0019.1.

Grecu, M., L. Tian, G. M. Heymsfield, A. Tokay, W. S. Olson, A. J. Heymsfield, and A. Bansemer, 2018, Nonparametric Methodology to Estimate Precipitating Ice from Multiple-Frequency Radar Reflectivity Observations, *J. App. Meteor.*, 57, 2605-2622, doi: 10.1175/JAMC-D-18-0036.1.

Green, D.R., J.D. Nilsen, R.E. Saffle, D.W. Holmes, M.D. Hudlow, and P.R. Ahnert, 1983: "RADAP-II, an interim radar data processor", *Preprints, 21st Conf. Radar Meteor., Amer. Meteor. Soc.*, 404-408.

Haddad, Z., E. A. Smith, C. D. Kummerow, T. Iguchi, M. R. Farrar, S. L. Durden, M. Alves, and W. S. Olson, 1997: The TRMM ''Day-1'' radar/radiometer combined rain-profiling algorithm. *J. Meteor. Soc. Japan*, 75, 799–809.

Haynes, J. M., R. T. Marchand, Z. Luo, A. Bodas-Salcedo, and G. L. Stephens, 2007: A Multipurpose Radar Simulation Package: QuickBeam. *Bull. Amer. Met. Soc.*, 88 (11), 1723–1727, dOI: 10.1175/BAMS-88-11-1723.

Haynes, J. M., T. S. L'Ecuyer, G. L. Stephens, S. D. Miller, C. Mitrescu, N. B. Wood, and S. Tanelli, 2009: Rainfall retrieval over the ocean with spaceborne W-band radar. *J. Geophys. Res.*, 114, D00A22, doi:10.1029/2008JD009973.

Heymsfield, A. J., et al., 2008, Testing IWC retrieval methods using radar and ancillary measurements with in situ data, *J. Appl. Meteorol. Climatol.*, 47, 135–163, doi:10.1175/2007JAMC1606.1.

Heymsfield, A. J., A. Bansemer, N. B. Wood, G Liu, S. Tanelli, O. O. Sy, M. Poellot, and C. Liu; 2018: Toward Improving Ice Water Content and Snow-Rate Retrievals from Radars. Part II: Results from Three Wavelength Radar–Collocated In Situ Measurements and CloudSat–GPM–TRMM Radar Data, *J. Appl. Meteor. Climat.*, 57, 365-389, doi: 10.1175/JAMC-D-17-0164.1

Hilburn, K. A., and F. J. Wentz, 2008: Intercalibrated passive microwave rain products from the unified microwave ocean retrieval algorithm (UMORA). *J. Appl. Meteor. Climatol.*, 47, 778-794, doi: 10.1175/2007JAMC1635.1.

Hiley, M. J., M. S. Kulie, and R. Bennartz, 2011. Uncertainty analysis for CloudSat snowfall retrievals. J. Appl. Meteorol. Climatol. 50, 399–418. doi:10.1175/2010JAMC2505.1.

Hitschfeld, W., and J. Bordan, 1954, Errors inherent in the radar measurement of rainfall at attenuating wavelengths. *J. Meteor.*, 11, 58-67.

Hogan, R. J. and A. Battaglia, 2008: Fast lidar and radar multiple scattering models: Part 2:Wide-angle scattering using the time-dependent two-stream approximation. *J. Atmos. Sci.*, 65, 3636–3651, doi: 10.1175/2008JAS2643.1.

Hollinger, J., R. Lo, and G. Poe, 1987: *Special Sensor Microwave/Imager User's Guide*, Naval Research Laboratory, Washington, D.C., Sep. 14, 1987.

Hong, G., Heygster, G., Miao, J., and Kunzl, K., 2005: Detection of tropical deep convective clouds from AMSU-B vater vapor channels measurements, *J. Geophys. Res.*, vol. 110, D05205, doi:10.1029/2004JD004949, 2005

Houze, R., et al., 2017: Olympic Mountains Experiment (OLYMPEX). *Bull. Amer. Met. Soc.*, https://doi.org/10.1175/BAMS-D-16-0182.1.

Hou, 2010, A. Y., Precipitation estimation using combined active/passive sensor information within the GPM framework, Proceedings of *ECMWF-JCSDA Workshop*, 2010.

Hou, A. Y., R. K. Kakar, S. Neeck, A. A. Azarbarzin, C. D. Kummerow, M. Kojima, R. Oki, K. Nakamura, and T. Iguchi, 2014: The Global Precipitation Measurement mission. *Bull. Amer. Meteor. Soc.*, 95, 701–722, doi:10.1175/BAMS-D-13-00164.1.

Iguchi, T., and R. Meneghini, 1994: Intercomparison of single-frequency methods for retrieving a vertical rain profile from airborne or spaceborne radar data. *J. Atmos. Oceanic Technol.*, 11, 1507–1516.

Iguchi, T. K., R. Meneghini, J. Awaka, and K. Okamoto, 2000: Rain-profiling algorithm for the TRMM Precipitation Radar. *J. Appl. Meteor.*, 39, 2038–2052.

Jaynes, E. T., cited 2001: Probability theory: The logic of science. [Available online at http://bayes.wustl.edu/etj/prob.html.]

Jazwinsky, A. H., 1970: *Stochastic Processes and Filtering Theory*. Academic Press, 376 pp.

Kidd, C: 1998: On rainfall retrieval using polarization-corrected temperatures International *Journal of Remote Sensing* 19 (5), 981-996

Kneifel, S., U. Loehnert, A. Battaglia, S. Crewell, D. Siebler, 2010: Snow scattering signals in ground-based passive microwave radiometer measurements. *J. Geophys. Res.-Atmos.* 2010, 115, D16214.

Kongoli, C.; Pellegrino, P.; Ferraro, R.R.; Grody, N.C.; Meng, H., 2003: A new snowfall detection algorithm over land using measurements from the Advanced Microwave Sounding Unit (AMSU). *Geophys. Res. Lett.* 2003, 30,doi:10.1029/2003GL017177

Kongoli C., H. Meng, J. Dong , and R. Ferraro, 2018: A Hybrid Snowfall Detection Method from Satellite Passive Microwave Measurements and Global Forecast Weather Models. *Q. J. Roy. Meteor. Soc.*, 2018, https://doi.org/10.1002/qj.3270

Kubota, T., Seto, S., Awaka. J., and Kida, S., 2014, Evaluation of Precipitation Estimates by at-Launch Codes of GPM/DPR Algorithms Using Synthetic Data from TRMM/PR Observations, *IEEE J. Appl. Earth Obs. Remote Sens.*, 7, 3931-3944, 2014

Kulie, M. S.; Bennartz, R.; Greenwald, T. J.; Chen, Y.; Weng, F., 2010: Uncertainties in Microwave Properties of Frozen Precipitation: Implications for Remote Sensing and Data Assimilation. *J. Atmospheric Sci.* 2010, 67, 3471–3487, doi:10.1175/2010JAS3520.1.

Kummerow, C., and L. Giglio, 1994: A passive microwave technique for estimating rainfall and vertical structure information from space, Part I: Algorithm description. *J. Appl. Meteor.*, 33, 3-18.

Kummerow, C., Y. Hong, W. S. Olson, S. Yang, R. F. Adler, J. McCollum, R. Ferraro, G. Petty, D. Shin, and T. T. Wilheit, 2001: The Evolution of the Goddard Profiling Algorithm (GPROF) for Rainfall Estimation from Passive Microwave Sensors. *J. Appl. Meteor.*, 40, 1801–1820, https://doi.org/10.1175/1520-0450(2001)040<1801:TEOTGP>2.0.CO;2

Kummerow, C. D., S. Ringerud, J. Crook, D. Randel and W. Berg, 2010. An observationally generated A-Priori database for microwave rainfall retrievals, *J. Atmos. and Oceanic Tech.*, 28(2), 113-130, doi: 10.1175/2010JTECHA1468.1.

Kummerow, C. D., D. L. Randel, M. Kulie, N.-Y. Wang, R. Ferraro, S. J. Munchak, and V. Petkovic, 2015: The evolution of the Goddard profiling algorithm to a fully parametric scheme. *J. Atmos. Oceanic Technol.*, 32, 2265–2280.

Kuo, K., W. S. Olson, B. T. Johnson, M. Grecu, L. Tian, T. L. Clune, B. H. van Aartsen, A. J. Heymsfield, L. Liao, and R. Meneghini, 2016: The Microwave Radiative Properties of Falling Snow Derived from Nonspherical Ice Particle Models. Part I: An Extensive Database of Simulated Pristine Crystals and Aggregate Particles, and Their Scattering Properties. *J. Appl. Meteor. Climatol.*, 55, 691–708, https://doi.org/10.1175/JAMC-D-15-0130.1

Laviola, S., and V. Levizzani, 2011: The 183-WSL fast rain rate retrieval algorithm. Part I: Retrieval design. *Atmospheric Research*, Volume 99, Number 3-4, p.443-461, (2011)

L'Ecuyer, T. S, and G. L. Stephens, 2002: An Estimation-Based Precipitation Retrieval Algorithm for Attenuating Radars. *J. Appl. Meteorol. Climatol.*, 41, 272-285.

Lebsock, M., and T. S. L'Ecuyer, 2011: The retrieval of warm rain from CloudSat, *J. Geophys. Res. Atmos.*, 116, D20209, doi:10.1029/2011JD016076

Lebsock, M., 2019: Level 2C RAIN-PROFILE Product Process Description and Interface Control Document, NASA JPL

Le, M., V. Chandrasekar, and S. Lim, 2009: Microphysical Retrieval from Dual-Frequency GPM Observations. Proceedings of *34th Conference on Radar Meteorology*, Williamsburg, VA.

Leinonen, J. and W. Szyrmer, 2015: Radar signatures of snowflake riming: A modeling study. *Earth and Space Science*, 2, 346–358, doi:10.1002/2015EA000102.

Leinonen, J., M. D. Lebsock, and G. L. Stephens, 2016: Improved Retrieval of Cloud Liquid Water from CloudSat and MODIS. *J. Appl. Meteorol. Climatol.*, 55, 1831-1844, doi: 10.1175/JAMC-D-16-0077.1.

Leinonen, J., et al., 2018: Retrieval of snowflake microphysical properties from multi-frequency radar observations. *Atm. Meas. Tech. Disc.*, https://doi.org/10.5194/amt-2018-73.

Lemonnier, F., J.-B. Madeleine, C. Claud, C. Genthon, C Durán-Alarcón, C. Palerme, A. Berne, N. Souverijns, N. van Lipzig, I. V. Gorodetskaya, T. L'Ecuyer, and N. Wood; 2019: Evaluation of CloudSat snowfall rate profiles by a comparison with in situ micro-rain radar observations in East Antarctica, The Cryosphere, 13, 943–954, doi: 10.5194/tc-13-943-2019

Levizzani, V., S. Laviola, and E. Cattani, C. Kidd, 2011: Detection and measurement of snowfall from space. *Remote Sens.*, 3, 145-166, doi:10.3390/rs3010145.

Lhermitte R., 1990, Attenuation and Scattering of Millimeter Wavelength Radiation by Clouds and Precipitation. *J. Atmos. Ocean. Tech.*, 7, 464-479

Liao, L., R. Meneghini, T. Iguchi, and A. Detwiler, 2003, Validation of snow parameters as derived from dual-wavelength airborne radar, presented at the *31st Int. Conf. Radar Meteorology*, Seattle, WA, Aug. 6–12, 2003.

Liao, L., and R. Meneghini, 2004: On study of air/space-borne dual-wavelength radar for estimates of rain profiles. *Third Int. Ocean–Atmosphere Conf.*, Beijing, China, Institute of Atmospheric Physics of Academia Sinica, CD-ROM.

Liu, G., 2004: Approximation of Single Scattering Properties of Ice and Snow Particles for High Microwave Frequencies. *J. Atmos. Sci.*, 61, 2441–2456, https://doi.org/10.1175/1520-0469(2004)061<2441:AOSSPO>2.0.CO;2

Liu, G.; Seo, E.-K., 2013: Detecting snowfall over land by satellite high-frequency microwave observations: The lack of scattering signature and a statistical approach. *J. Geophys. Res. Atmospheres* 2013, 118, 1376–1387, doi:10.1002/jgrd.50172.

Mardiana, R., T. Iguchi, N. Takahashi, and H. Hanado, 2003, Dual-frequency rain profiling method without the use of surface reference technique, in *Proc. IGARSS*, vol. 3, Jul. 21–25, 2003, pp. 1954–1956.

Mardiana, R., T. Iguchi, and N. Takahashi, 2004, A dual-frequency rain profiling method without the use of a surface reference technique, *IEEE Trans. Geosci. Remote Sens.*, vol. 42, no. 10, pp. 2214–2225, Oct. 2004.

Marks, C. J., and C. D. Rodgers, 1993: A retrieval method for atmospheric composition from limb emission measurements. *J. Geophys. Res.*, 98, 14 939–14 953.

Marzano F. S., A. Mugnai, G. Panegrossi, N. Perdicca, E. A. Smith, and J. Turk, 1999: Bayesian estimation of precipitating cloud parameters from combined measurements of space-borne microwave radiometer and radar, *IEEE Trans. Geosci. Remote Sens.*, vol. 37, no. 1, pp. 593-613.

Mason, S. L., J. C. Chiu, R. J. Hogan, and L. Tian, 2017: Improved rain rate and drop size retrievals from airborne Doppler radar. *Atmos. Chem. Phys.*, 17, 11 567–11 589, doi.org/10.5194/acp-17-11567-2017.

Mason, S. L., R. J. Hogan, C. D. Westbrook, S. Kneifel, and D. Moisseev, 2019, The importance of particle size distribution shape for triple-frequency radar retrievals of the morphology of snow, *Atmos. Meas. Tech.*, submitted 2019

Matrosov, S. Y., 2007: Potential for attenuation-based estimations of rainfall rate from CloudSat. *Geophys. Res. Lett.*, 34, L05817, doi:10.1029/2006GL029161.

Matrosov, S., 2008: Assessment of Radar Signal Attenuation Caused by the Melting Hydrometeor Layer. *IEEE Trans. Geosci. Remote Sens.*, 46 (4), 1039–1047, doi: http://dx.doi.org/10.1175/2007JAMC1768.1.

Matrosov, S. Y., A. J. Heymsfield, and Z. Wang, 2005, Dual-frequency radar ratio of nonspherical atmospheric hydrometeors, *Geophys. Res. Lett.*, 32, L13816, doi:10.1029/2005GL023210.

Matrosov, S. Y., 2015, The Use of CloudSat Data to Evaluate Retrievals of Total Ice Content in Precipitating Cloud Systems from Ground-Based Operational Radar Measurements. *J. Appl. Meteorol. Climatol.*, 54, 1663-1674, doi: 10.1175/JAMC-D-15-0032.1.

Matrosov, S. Y.; 2019: Comparative Evaluation of Snowfall Retrievals from the CloudSat W-band Radar Using Ground-Based Weather Radars, *J. Atmos. Ocean. Tech.*, doi:10.1175/JTECH-D-18-0069.1

Matsui, T., T. Iguchi, X. Li, M. Han, W. Tao, W. Petersen, T. L'Ecuyer, R. Meneghini, W. Olson, C.D. Kummerow, A.Y. Hou, M.R. Schwaller, E.F. Stocker, and J. Kwiatkowski, 2013: GPM Satellite Simulator over Ground Validation Sites. *Bull. Amer. Meteor.* Soc., 94, 1653–1660, https://doi.org/10.1175/BAMS-D-12-00160.1

Meissner, T., and F. J. Wentz, 2012: The emissivity of the ocean surface between 6 – 90 GHz over a large range of wind speeds and Earth incidence angles. *IEEE Trans. Geosci. Rem. Sens.*, 50(8), 3004-3026, doi: 10.1109/TGRS.2011.2179662.

Meneghini, R., H. Kumagai, J. R. Wang, T. Iguchi, and T. Kozu, 1997, Microphysical retrievals over stratiform rain using measurements from an airborne dual-wavelength radar-radiometer, *IEEE Trans. Geosci. Remote Sens.*, vol. 35, no. 3, pp. 487–506, May 1997.

Meneghini, R., L. Liao, and T. Iguchi, 2002, Integral equations for a dual-wavelength radar, in *Proc. IGARSS*, vol. 1, Jun. 24–28, 2002, pp. 272–274.

Mie, Gustav (1908). "Beiträge zur Optik trüber Medien, speziell kolloidaler Metallösungen". Annalen der Physik. 330 (3): 377–445.

Miller, S. D., G. L. Stephens, C. K. Drummond, A. K. Heidinger, and P. T. Partain, 2000: A multisensor diagnostic satellite cloud property retrieval scheme. *J. Geophys. Res.*, 105, 19 955–19 971.

Mitrescu, C., T. L'Ecuyer, J. Haynes, S. Miller, and J. Turk, 2010, CloudSat Precipitation Profiling Algorithm—Model Description. *J. Appl. Meteorol. Climatol.*, 49, 991-1003, doi: 10.1175/2009JAMC2181.1

Mugnai, A., H. J. Cooper, E. A. Smith, and G. J. Tripoli, 1990: Simulation of microwave brightness temperatures of an evolving hailstorm at SSM/I frequencies. *Bull. Am. Meteorol. Soc.*, vol. 71, no. 1, pp. 2–13, 1990.

Olson W. S., 1987: Estimation of Rainfall Rates in Tropical Cyclones by Passive Microwave Radiometry. Ph.D. Thesis. University of Wisconsin, 282pp.

Olson, W. S., C. D. Kummerow, G. M. Heymsfield, and L. Giglio, 1996: A method for combined passive–active microwave retrievals of cloud and precipitation profiles. *J. Appl. Meteor.*, 35, 1763–1789.

Palerme, C., J. E. Kay, C. Genthon, T. L'Ecuyer, N. B. Wood, and C. Claud; 2014: How much snow falls on the Antarctic ice sheet?, *The Cryosphere*, 8, 1577-1587

Panegrossi G., S. Dietrich, F. S. Marzano, A. Mugnai, E. A. Smith, X. Xiang, J. Tripoli, P. K. Wang and J. P. V. Poiares Baptista, 1998: Use of cloud model Microphysics for passive microwave-based precipitation retrieval: significance of consistency between model and measurement manifolds; *J. Atmos. Sci.*, 55, 1644-1673, doi: http://dx.doi.org/10.1175/1520-0469(1998)055<1644:UOCMMF>2.0.CO;2

Panegrossi G., J-F. Rysman, D. Casella, A. C. Marra, P. Sanò, and M. S. Kulie, 2017: CloudSat-based assessment of GPM Microwave Imager snowfall observation capabilities, *Rem. Sensing*, 9(12), 1263; doi:10.3390/rs9121263, 2017.

Prigent, C., F. Aires., W. B. Rossow, 2006: Land surface microwave emissivities over the globe for a decade. *Bull. Am. Meteorol. Soc.* 2006, 87, 1573–1584.

Protat, A., J. Delanoe, E. J. O'Connor, and T. S. L'Ecuyer, 2010: The evaluation of CloudSat and CALIPSO ice microphysical products using ground-based cloud radar and lidar observations. *J. Atmos. Oceanic Technol.*, 27, 793–810, doi:10.1175/2009JTECHA1397.1.

Rodgers, C. D., 1976: Retrieval of atmospheric temperature and composition from remote measurements of thermal radiation. *Rev. Geophys. Space Phys.*, 14, 609–624.

Rodgers, C. D., 1990: Characterization and error analysis of profiles retrieved from remote sounding measurements. *J. Geophys. Res.*, 95, 5587–5595.

Rodgers, C. D., 2000, *Inverse Methods for Atmospheric Sounding: Theory and Practice*, World Sci., River Edge, N.J.

Rodgers, E., and H. Siddalingaiah, 1983: The Utilization of Nimbus-7 SMMR Measurements to Delineate Rainfall over Land. *J. Climate Appl. Meteor.*, 22, 1753–1763, https://doi.org/10.1175/1520-0450(1983)022<1753:TUONSM>2.0.CO;2

Rose, C. R., and V. Chandrasekar, 2005, A Systems Approach to GPM Dual-Frequency Retrieval, *IEEE Trans. Geosci. Remote Sens.*, vol. 43, no. 8, pp. 1816–1826, Aug. 2005.

Rose, C. R., and V. Chandrasekar, 2006: A GPM Dual-Frequency Retrieval Algorithm: DSD Profile-Optimization Method. *J. Atmos. Ocean Technol.*, 23, 1372–1383.

Rysman, J.-F., G. Panegrossi G., P. Sanò, A. C. Marra, S. Dietrich, L. Milani, M. S., Kulie, SLALOM, 2018: An all-surface snow water path retrieval algorithm for the GPM Microwave Imager, *Rem. Sensing, Remote Sens.* 10(8), 1278; https://doi.org/10.3390/rs10081278, 2018.

Sadowy, G. A., A. C. Berkun, W. Chun, E. Im, and S. L. Durden., 2003: Development of an advanced airborne precipitation radar. *Microwave Journal*, 46 (1), 84–98.

Sanò, P., Panegrossi, G., Casella, D., Di Paola, F., Milani, L., Mugnai, A., Petracca, M., and Dietrich, S., 2015: The Passive microwave Neural network Precipitation Retrieval (PNPR) algorithm for AMSU/MHS observations: description and application to European case studies. *Atmos. Meas. Tech.*, 8, 837–857, doi:10.5194/amt-8-837-2015, 2015.

Sanò, P., Panegrossi, G., Casella, D., Marra, A. C., Di Paola, F., and Dietrich, S., 2016: The new Passive microwave Neural network Precipitation Retrieval (PNPR) algorithm for the cross-track scanning ATMS radiometer: description and verification study over Europe and Africa using GPM and TRMM spaceborne radars, *Atmos. Meas. Tech.*, 9, 5441-5460, https://doi.org/10.5194/amt-9-5441-2016, 2016.

Sanò P., G. Panegrossi, D. Casella, A. C. Marra, L. P. D'Adderio, J.-F. Rysman, S. Dietrich, 2018: The Passive Microwave Neural Network Precipitation Retrieval (PNPR) algorithm for the Conical Scanning GMI Radiometer, *Remote Sens.*, 10, 1122; doi:10.3390/rs10071122, 2018

Savage, R. C., and J. A. Weinman, 1975: Preliminary calculations of the upwelling radiance from rain clouds at 37.0 and 19.35 GHz. *Bull. Amer. Meteor. Soc.*, 56, 1272-1274.

Shukla, A. K., C. S. P. Ojha, R. P. Singh, L. Pal, and D. Fu; 2019: Evaluation of TRMM Precipitation Dataset over Himalayan Catchment: The Upper Ganga Basin, India, *Water*, 11, 613; doi:10.3390/w11030613

Skofronick-Jackson, G., B. T. Johnson, 2011: Surface and atmospheric contributions to passive microwave brightness temperatures for falling snow events. *J. Geophys. Res.* 2011, 116, doi:10.1029/2010JD01443

Skofronick-Jackson, G., W. A. Petersen, W. Berg, C. Kidd, E. F. Stocker, D. B. Kirschbaum, R. Kakar, S. A. Braun, G. J. Huffman, T. Iguchi, P. E. Kirstetter, C. D. Kummerow, R. Meneghini, R. Oki, W. S. Olson, Y. N. Takayabu, K. Furukawa, and T. Wilheit, 2017: The Global Precipitation Measurement (GPM) mission for science and society. *Bull. Amer. Meteor. Soc.*, 98, 1679-1695, doi:10.1175/BAMS-D-15-00306.1.

Skofronick-Jackson, G., D. Kirschbaum, W. Peterson, G. Huffman, C. Kidd, E. Stocker, and R. Kakar, 2018: The Global Precipitation Measurement (GPM) mission's scientific achievements and societal contributions: reviewing four years of advanced rain and snow observations. *Q. J. R. Meteorol. Soc.*, 144 (Suppl. 1), 27–48.

Smith E. A., H. J. Cooper, X. Xiang, A. Mugnai, and G. J. Tripoli, 1992: Foundations for Statistical-Physical Precipitation Retrieval from Passive Microwave Satellite Measurements. Part I: Brightness-Temperature Properties of a Time-dependent Cloud-Radiation Model, *J. Appl. Meteor.*, vol. 31, no. 6, pp. 506–531, 1992.

Spencer, R. W., 1986: A satellite passive 37-GHz scattering based method for measuring oceanic rain rates.

Spencer, R. W., H. M. Goodman, and R. E. Hood, 1989: Precipitation Retrieval over Land and Ocean with the SSM/I: Identification and Characteristics of the Scattering Signal. *J. Atmos. Oceanic Technol.*, 6, 254–273, https://doi.org/10.1175/1520-0426(1989)006<0254:PROLAO>2.0.CO;2

Spencer, R. W., 1993: Global Oceanic Precipitation from the MSU during 1979—91 and Comparisons to Other Climatologies. *J. Climate*, 6, 1301–1326, https://doi.org/10.1175/1520-0442(1993)006<1301:GOPFTM>2.0.CO;2

Surussavadee, C. and D. H. Staelin, 2008: Global millimeter-wave precipitation retrievals trained with a cloud-resolving numerical weather prediction model, Part I: Retrieval design, *IEEE T. Geosci. Remote*, vol. 46, n. 1, pp. 99-108, doi:10.1109/TGRS.2007.908302, 2008

Takbiri, Z., A. Ebtehaj, E. Foufoula-Georgiou, P. Kirstetter, and F. Turk, 2019: A Prognostic Nested K-Nearest Approach for Microwave Precipitation Phase Detection over Snow Cover. *J. Hydrometeor*. doi:10.1175/JHM-D-18-0021.1, in press.

Tridon, F., et al., 2018: The microphysics of stratiform precipitation during OLYMPEX: compatibility between 3-frequency radar and airborne in situ observations. *J. Geophys. Res.*, under submission

Ulaby, F. T., R. K. Moore, and A. K. Fung, (1986): Microwave Remote Sensing: Radar Remote Sensing and Surface Scattering and Emission Theory. Norwood, MA: Artech House, Inc. 1064pp. IBSN 0890061912

Wentz, F. J., and R. W. Spencer, 1998: SSM/I rain retrievals within a unified all-weather ocean algorithm. *J. Atmos. Sci.*, 55, 1613-1627.

Wentz, F. J., and T. Meissner, 2016: Atmospheric absorption model for dry air and water vapor at microwave frequencies below 100 GHz derived from spaceborne radiometer observations. *Radio Sci.*, 51, doi: 10.1002/2015RS005858.

Wilheit, T.: 1972, 'The Electrically Scanning Microwave Radiometer (ESMR) Experiment', Nimbus-5 User's Guide, NASA/Goddard Space Flight Center, Greenbelt, Maryland, 59–105.

Wilheit, T.: 1975, 'The Electrically Scanning Microwave Radiometer (ESMR) Experiment', Nimbus-6 User's Guide, NASA/Goddard Space Flight Center, Greenbelt, Maryland, 87–108.

Wilheit, T. T., A. T. Chang, and L. S. Chiu, 1991: Retrieval of Monthly Rainfall Indices from Microwave Radiometric Measurements Using Probability Distribution Functions. *J. Atmos. Oceanic Technol.*, 8, 118–136, https://doi.org/10.1175/1520-0426(1991)008<0118:ROMRIF>2.0.CO;2

Wilheit, T., R. Adler, S. Avery, E. Barret, P. Bauer, W. Berg, A. Chang, J. Ferriday, N. Grody, S. Goodman, C. Kidd, D. Kniveton, C. Kummerow, A. Mugnai, W. Olson, G. Petty, A. Shibata, and E. Smith, 1994: Algorithms for the retrieval of rainfall from passive microwave measurements, *Remote Sensing Rev.*, vol. 11, n. 1-4, pp. 163-194, 1994

Wood, N. B., T. S. L'Ecuyer, D. Vane, G. L. Stephens, and P. Partain, 2013: Level 2C Snow Profile Process Description and Interface Control Document, NASA JPL

Wood, N. B., T. S. L'Ecuyer, A. J. Heymsfield, G. L. Stephens, D. R. Hudak, and P. Rodriguez, 2014: Estimating snow microphysical properties using collocated multisensor observations, *J. Geophys. Res. Atmos.*, doi: 10.1002/2013JD021303

You, Y., N.-Y. Wang, R. Ferraro, and S. Rudlosky, 2017: Quantifying the Snowfall Detection Performance of the GPM Microwave Imager Channels over Land. *J. Hydrometeorol.* 2017, 18, 729–751, doi:10.1175/JHM-D-16-0190.1.